Impact of Grey Matter Conductivity Anisotropy on EEG and MEG Source Estimation

Master's Thesis

Presented by:

Timon Gronotte

Matriculation Number: 459 872

Major: Mathematics

Advisors:

Prof. Dr. Carsten Wolters

Prof. Dr. Christian Engwer

Münster, October 27, 2025

Declaration of Academic Integrity

I hereby confirm that this thesis, entitled "Impact of Grey Matter Conductivity Anisotropy on EEG and MEG Source Estimation", is solely my own work and that I have used no sources or aids other than the ones stated. All passages in my thesis for which other sources, including electronic media and AI tools, have been used, be it direct quotes or content references, have been acknowledged as such and the sources cited. I am aware that plagiarism is considered an act of deception which can result in sanction in accordance with the examination regulations.

I confirm that I am aware that my work may be cross-checked with other texts to identify possible similarities and that it may be stored in a database for this purpose.

I confirm that I have not submitted the following thesis in part or whole as an examination paper before.

Münster, October 27, 2025

Acknowledgements

I would like to thank everyone who contributed to and supported me throughout this thesis, especially

- Prof. Dr. Carsten Wolters for the opportunity to work in his group, for his academic guidance and supervision of the thesis.
- Prof. Dr. Christian Engwer for his helpful insights, for his patience and guidance towards this final thesis.
- Prof. Dr. Sampsa Pursiainen for the kind welcome and discussions at the Tampere University and the enlightening workshops there and in Münster.
- Doctoral student Malte Höltershinken for all his help with scientific and software-related questions.
- My family and friends for all of their support throughout my studies.

This work was supported by the Deutsche Forschungsgemeinschaft (DFG), projects WO1425/11-1 and WO1425/10-2, by DAAD project 57663920 and by ERA PerMed project ERAPERMED2020-227, PerEpi (Bundesministerium für Gesundheit (BMG), project ZMI1-2521FSB006).

Contents

Symbols

Ω Volume conductor domain
u Electric potential
σ Conductivity tensor
σ_r Radial conductivity
σ_t Tangential conductivity
q Anisotropy ratio
M Dipole moment
x_0 Dipole position
μ Magnetic permeability
ϵ Electric Permittivity
ρ Charge density
E Electric field
B Magnetic flux
B^P Primary magnetic flux
B^S Secondary magnetic flux
A Magnetic potential
j Current density
j^p Primary current density
n Unit outer normal
Ω^∞ Patch region
$\tilde{\Omega}$ Transition region
χ Continues indicator function
u^∞ Infinity potential
u^c Correction potential
σ^∞ Infintiy conductivity
σ^c Correction conductivity
∇ Gradient operator
$\nabla\cdot$ Divergence operator
Δ Laplace operator
$\nabla\times$ Curl operator
δ_{x_0} Dirac distribution
$||\cdot||$ Assicaited L^2 norm
H^1 First order Sobolev space
S_h^1 Used FEM space
$\mathbb{P}^1$ Space of affine linear functions

1. Introduction

Electroencephalography (EEG) and Magnetoencephalography (MEG) source estimation is an ill-posed inverse problem in biomedical brain research. It is concerned with reconstructing current distributions inside the brain from measurements of electric potential and magnetic fluxes. These methods provide a powerful tool in studying brain connectivity [56] as well as neurological disorders such as epilepsy [69, 51], depression [20] and many more, as they allow noninvasive measurements with high temporal resolution.

Solving the inverse problem requires accurate simulations of potentials and fields produced by current distributions [28, 43]. As such, all numerical simulation errors need to be as low as possible. Simplifying assumptions, such as disregarding volume conductor geometry or tissue conductivity structure, introduce model errors. Such model errors are unavoidable, however, it is most important to be aware of the assumptions made and how much influence they have.

A finite element method (FEM) provides a flexible and accurate solution to model geometrically complicated, inhomogeneous and anisotropic head volume conductors [12]. Still, discretizing a model for numerical solving introduces further issues. For instance, the EEG and MEG forward problems contain a singularity for the most common current distribution used to simulate local brain activity [18, 28]. While in the FEM context there is a mathematically rigorous solution to this problem in the form of subtraction approaches, they so far suffered from high computational complexity [71, 8]. Another option is St. Venant type approaches [67, 12], which approximate the singularity with low computational complexity and with only a very small error. Further all options are vulnerable to insufficient approximations due to, for example, insufficient mesh resolution, deformed elements or an inappropriate choice of the basis functions.

Studies have not only shown that the gray matter has an anisotropic structure, even in adults [68, 62, 3], but also that modeling these anisotropic conductivities has significant effects in realistic head models [72, 74, 30, 26, 27], especially in the gray matter compartment. Yet, gray matter anisotropy is not usually modeled, and to the best of our knowledge, there is only a single study validating FEM approaches in its presence [21]. While the standard remains to model gray matter source space conductivity as isotropic, the study by Drechsler et al. investigated only sphere models. Furthermore, the discretizations used in that study have since been significantly improved to the Local Subtraction approach [33] and the Multipolar St. Venant approach [67].

This thesis investigates gray matter modeling errors and associated numerical errors

while validating the Local Subtraction approach. The model errors caused by ignoring gray matter anisotropy for EEG will be quantified and compared to the numerical errors produced by the most modern numerical approximations on spherical models as well as realistic head models. This should provide the data needed to decide if isotropic source space modeling is still appropriate for all source reconstructions. Additionally, the new Local Subtraction approach will be closely investigated, especially the influence of varying the sparsity of the right-hand side vector through its parametrization. This should further support it as a practical choice in source reconstruction or reveal its limitations. Lastly, the compatibility of the Local Subtraction approach with the MEG forward problem in the case of gray matter conductivity is explored along with preliminary testing of numerical MEG errors. This should show the significant difficulty of generalizing the Local Subtraction approach towards this use case while providing first insights for future MEG research.

First, to investigate the parameter dependence of the Local Subtraction approach, parameter sweeps of the extension distance are performed on differently resolved spherical head models and current dipoles at varying eccentricities. The findings are then used to recommend a parametrization depending on the mesh, which is then used for all other investigations.

Second, the model error caused by assuming isotropic gray matter conductivities is then assessed by finding pairings of isotropic and anisotropic conductivities that show minimal differences in a four-layer sphere model. This is possible due to the existence of analytical solutions [16] and will be used to study the effects of anisotropy, used difference measure, source orientation and depth through parameter variation. The resulting error bounds will then be used to compare against the numerical errors produced by the Local Subtraction and Multipolar St. Venant approaches. While executing the same parameters as for the model error investigations, the dependence on the mesh resolution will additionally be tested.

Third, to investigate numerical errors on a realistic head model of an adult, simulations with both mentioned approaches are executed for an isotropic conductivity parametrization as well as multiple anisotropic ones. The results are then checked against each other as well as against the results from a refined head model. Furthermore, the effects on different dipole locations will be visualized.

Finally, the precursory MEG investigation will explore the mathematics of anisotropic conductivities in the source space for the Local Subtraction approach before presenting some numerical results, to inspire further work.

2. Preliminaries

2.1. The Forward Model

In this section we briefly introduce the models that are used to calculate the potentials at the EEG sensors and fluxes at the MEG magnetometers given a source current density j^p.

2.1.1. The EEG Forward Model

The EEG sensors measure the electric potential, i.e. a voltage at the head surface, which we derive from the Maxwell equations. To obtain a solution for these equations, we impose the Heaviside-Gibbs gauge and further restrict to a quasi-static formulation of the equations. This is the current standard in the field [55, 33, 73, 17, 66] and the reasoning for the approximation can be found, for example, in appendix B of [44] or [28].

In this simplified model the source current needs to lie in a conductor Ω, which has the potentially anisotropic conductivity tensor field $\sigma : \Omega \to \mathbb{R}^{3\times 3}$, electric permittivity ϵ and constant magnetic permeability μ. The electric field E and magnetic field B caused by j^p are now the solution to:

$$\nabla \cdot E = \frac{\rho}{\epsilon} \tag{2.1}$$

$$\nabla \times E = 0 \tag{2.2}$$

$$\nabla \times B = \mu j \tag{2.3}$$

$$\nabla \cdot B = 0 \tag{2.4}$$

Where ρ is the electric charge density and the current density j is given by:

$$j = j^p + \sigma E \tag{2.5}$$

Due to the imposed gauge, we have for the electric potential u:

$$E = -\nabla u \tag{2.6}$$

Taking the divergence of (2.3) yields due to the vector identity $\nabla \cdot (\nabla \times B) = 0$:

$$0 = \nabla \cdot (j^p - \nabla u) \tag{2.7}$$

Additionally, we assume that no current can flow out of the volume conductor, giving us a Neumann boundary condition. To ensure a unique solution, we additionally set the electric potential to 0 at an arbitrary point $x_{ref} \in \partial\Omega$, yielding:

Definition 1 (EEG forward problem)**.** *Let $\Omega \subset \mathbb{R}^3$ be a volume conductor with boundary $\partial\Omega$ and outer normal n with conductivity $\sigma : \Omega \to \mathbb{R}^{3\times 3}$. Then the electric potential $u : \Omega \to \mathbb{R}$ due to the primary current j^p and hence the EEG forward problem, is the solution to:*

$$\begin{cases} \nabla \cdot (\sigma \nabla u) = \nabla \cdot j^p & \text{on } \Omega \\ \langle \sigma \nabla u, n \rangle = 0 & \text{on } \partial\Omega \\ u(x_{ref}) = 0 \end{cases} \tag{2.8}$$

Note that one could impose more complex boundary conditions, such as the complete electrode model, to more accurately model the conductive EEG electrodes [40, 52]. Further, in practice, one usually simulates the EEG electrodes by sampling the electric potential at their respective positions.

2.1.2. The MEG Forward Model

To simulate the magnetic field B generated by neural activity, we derive an approach utilizing our EEG forward model. We closely follow [34] §2.1 for this motivation.

First, recall that for a differentiable scalar field φ and a differentiable vector field F on $\mathbb{R}^3$, we have the following identities, which can be confirmed by direct computation:

$$\nabla \times (\varphi \cdot F) = \varphi \cdot (\nabla \times F) + \nabla\varphi \times F \tag{2.9}$$

$$\nabla \times (\nabla \times F) = \nabla (\nabla \cdot F) - \Delta F \tag{2.10}$$

These allow us to derive a Laplace equation:

$$\Delta B \overset{2.10}{=} \nabla (\nabla \cdot B) - \nabla \times (\nabla \times B) \overset{2.4}{=} -\nabla \times (\nabla \times B) \overset{2.3}{=} -\mu \nabla \times j \tag{2.11}$$

Defining the Newton potential for $\mathbb{R}^3$:

$$N(x) := -\frac{1}{4\pi} \cdot \frac{1}{||x||} \tag{2.12}$$

We have for sufficiently regular j

$$\Delta \left(\int_{\mathbb{R}^3} N(x-y) j(y) dV(y) \right) = j(x) \tag{2.13}$$

As shown in [22] §16 Satz 1, we assume that j is compactly supported. Taking $B \xrightarrow{x\to\infty} 0$ from physical intuition, B is uniquely determined by [22] §16 Corollary 2. Hence using Stokes' theorem:

$$\begin{aligned} B(x) &= \int_{\mathbb{R}^3} N(x-y)(-\mu\nabla \times j)\, dV(y) \\ &= \frac{\mu}{4\pi}\int_{\mathbb{R}^3} \frac{1}{||x-y||}\left(\nabla \times j\right)(y)\, dV(y) \\ &\overset{2.9}{=} \frac{\mu}{4\pi}\int_{\mathbb{R}^3} -\left(\nabla_y \frac{1}{||x-y||}\right) \times j\, dV(y) \\ &= \frac{\mu}{4\pi}\int_{\mathbb{R}^3} j \times \frac{x-y}{||x-y||^3}\, dV(y) \end{aligned} \tag{2.14}$$

This last equation is the usual starting point [55, 33, 28] for solving the MEG forward problem and is formally known as:

Definition 2 (Biot-Savart law)**.** *Given an electric current density j in the volume conductor Ω, the magnetic flux density B at some point x outside Ω is given by the Biot-Savart law:*

$$B(x) = \frac{\mu_0}{4\pi}\int_\Omega j(y) \times \frac{x-y}{||x-y||^3} dV(y) \tag{2.15}$$

where μ is the magnetic permeability of the vacuum.

Noting that it is linear in j, the MEG forward problem is directly obtained by inserting equations 2.5 and 2.6:

Definition 3 (MEG forward problem)**.** *Let j^p be an electric primary current density in the volume conductor Ω, with conductivity σ and electric potential u in Ω generated by j^p. Then we call for all $x \notin \Omega$*

$$B^P(x) = \frac{\mu_0}{4\pi}\int_\Omega j^p(y) \times \frac{x-y}{||x-y||^3} dV(y) \tag{2.16}$$

the primary magnetic field and

$$B^S(x) = -\frac{\mu_0}{4\pi}\int_\Omega \sigma(y)\nabla u(y) \times \frac{x-y}{||x-y||^3} dV(y) \tag{2.17}$$

the secondary magnetic field. The magnetic flux density B and hence the MEG forward problem can be computed as $B = B^P + B^S$.

The two parts of the magnetic field are named after their respective sources. The primary current density j^p caused by neural activity produces the primary magnetic field. The passive volume currents $\sigma\nabla u$, which are induced by j^p, produce the secondary magnetic field. Hence, to solve the MEG forward problem this way requires first solving the EEG forward problem.

Note that in practice, it is not possible to sample the magnetic field at a single point. Instead, one measures the fluxes through a set of magnetometers.

$$\int_F \langle B, n\rangle\, dS \tag{2.18}$$

Where F is some surface enclosed by the pickup coil of an MEG sensor, along with a unit normal n.

2.2. Dipole Models

In this section, we want to discuss the relevant current densities j^p. From equation (2.8), it is immediately clear that j^p fully determines the obtained solution and hence j^p must be chosen carefully.

As aforementioned, we ultimately want to reconstruct some neural activity from the measured signals. The first step towards this goal is to model a single neural event. Theoretically, that is any instance where a current is produced in the brain. Practically, we need a large set of cells simultaneously producing aligned currents to obtain a measurable signal. Hence, we want to solve the forward problems for small regions in the brain where j^p is non-zero and of some sufficiently nice form.

However, the extent of these regions is unclear, especially if we want to reconstruct unknown activity. Further we would need to determine a complete vector field for j^p in this region. The standard way to work with these issues is to assume the neural activity is local to a single point and can be mathematically described as a point dipole:

$$j^p(x) := M\delta_{x_0}(x) \tag{2.19}$$

where $M \in \mathbb{R}^3$ is the dipole moment vector, representing direction and strength, δ_{x_0} is the Dirac distribution at x_0 defined by

$$\delta_{x_0}(x) := \begin{cases} 1 & x = x_0 \\ 0 & x \neq x_0 \end{cases} \tag{2.20}$$

where x_0 is interpreted as the dipole position.

The advantage of this model is the reduction to only six parameters that need to be reconstructed. While it is not obvious that this is a valid simplification, its adequacy has been investigated multiple times [18, 61] and the effects have been declared negligible.

Additionally, j^p is not differentiable at x_0 and cannot be directly integrated into standard numerical models, necessitating special treatment. We will investigate two general classes of methods to address this singularity in the context of finite element methods (FEM), though we note that other approaches exist, including further FEM techniques [47, 63], boundary element methods [42, 48] and in some limited cases, analytical solutions [16], each with their own respective preconditions, strengths and weaknesses.

These two investigated classes are:

1. Approximation of the singular point through an arrangement of non-singular sources. As a concrete example of this approach, we will introduce the Multipolar St. Venant method [67]. It was chosen as the de facto standard approach in the field due to its low computational complexity and very good results.

2. Analytical regularization to reformulate the problem into an expression that is directly solvable using standard numerical models. The Local Subtraction approach [33] will be introduced as an example of this method. It was chosen as a contender to the Multipolar St. Venant approach due to promising initial results and a clean mathematical derivation.

2.2.1. The Finite Element Formulation

As our stated interest lies in two FEM approaches, this section is dedicated to deriving a fairly standard continuous Galerkin formulation of the EEG forward problem from definition 1.

Given a bounded volume conductor $\Omega \subset \mathbb{R}^3$ with a Lipschitz continuous boundary $\partial\Omega$, we first want to obtain a weak solution to (2.8) in $H^1(\Omega)$, that is, the first-order Sobolev space with respect to the Euclidean L^2 norm.

Initially, we assume we have a continuously differentiable current density $j^p \in C^1(\Omega, \mathbb{R}^3)$, a smooth coercive symmetric positive definite tensor field $\sigma \in C^\infty(\Omega, \mathbb{R}^{3\times3})$ and a corresponding twice continuously differentiable solution $u \in C^2(\mathbb{R}^3, \mathbb{R})$ to (2.8) on Ω for an arbitrary $x_{ref} \in \Omega$. Then we have for any smooth, compactly supported test function $\varphi \in C^\infty(\mathbb{R}^3, \mathbb{R})$:

$$\int_\Omega [\nabla \cdot (\sigma \nabla u)] \cdot \varphi \, dV = \int_\Omega [\nabla \cdot j^p] \cdot \varphi \, dV \tag{2.21}$$

Applying integration by parts on the left hand side yields:

$$-\int_\Omega (\sigma \nabla u) \cdot \nabla \varphi \, dV = \int_\Omega [\nabla \cdot j^p] \cdot \varphi \, dV \tag{2.22}$$

Where the boundary term drops due to our Neumann boundary condition. We thus directly obtain a coercive continuous bilinear form on $H^1(\Omega)$:

$$a(v, w) := \int_\Omega (\sigma \nabla v) \cdot \nabla w \, dV \tag{2.23}$$

Alongside a continuous linear operator on $H^1(\Omega)$:

$$l(v) := \int_\Omega [\nabla \cdot j^p] \cdot v \, dV \tag{2.24}$$

Which defines our abstract elliptic problem $a(u, w) = l(w) \; \forall w \in H^1(\Omega)$. For this work, we restricted ourselves to considering admissible triangulations $\mathcal{T}_h$ based on tetrahedrons along first-order Lagrangian shape functions, resulting in the linear finite-element space:

$$S_h^1(\Omega) := \left\{ v_h \in C^0(\Omega) | v_h|_T \in \mathbb{P}^1 \; \forall T \in \mathcal{T}_h \right\} \subset H^1(\Omega) \tag{2.25}$$

Where $\mathbb{P}^1(T)$ denotes the space of affine linear functions over T, thus we define:

Definition 4 (EEG Finite Element Forward Problem)**.** *Let the volume conductor Ω, admissible triangulation $\mathcal{T}_h$, conductivity σ, current density j^p, bilinear form a, linear operator l and finite-element space $S_h^1(\Omega)$ be defined as above. Then the potential u_h is a solution to the finite element EEG forward problem if:*

$$a(u_h, w) = l(w) \ \forall w \in S_h^1(\Omega) \tag{2.26}$$

Deriving the FEM formulation required us to assume a continuously differentiable current density j^p, which, as mentioned above, is not the case for a point dipole. While the requirements could potentially be lowered, to the author's knowledge, no FEM approach is known that allows direct inclusion of the point dipole, necessitating some adjustment to the right-hand side. Next, we will introduce the Local Subtraction and Multipolar St. Venant approaches with their respective adjustments.

2.2.2. The Local Subtraction Approach

Here we seek to introduce the Local Subtraction approach as presented by Höltershinken et al. [33]. The original work presents a comprehensive derivation along with proving existence and uniqueness and is highly recommended. As such, we will focus on declaring the algorithm and highlighting its dependencies.

First, we reiterate the underlying assumptions on head models that were made to derive a weak formulation of the EEG forward problem. Namely, our head model is confined to a bounded Lipschitz domain $\Omega \subset \mathbb{R}^3$ with boundary $\partial\Omega$. This domain is adorned with a smooth, symmetric positive definite tensor field $\sigma : \Omega \mapsto \mathbb{R}^{3\times3}$ describing the potentially anisotropic conductivity throughout the model.

Given a dipole at position $x_0 \in \Omega$ with moment $M \in \mathbb{R}^3$, the only additional assumption required for this approach is that there is an open neighborhood $U \subset \Omega$ containing the dipole position on which σ is constant. Going forward, we will call the conductivity in this set $\sigma^\infty := \sigma(x_0)$.

The idea of subtraction approaches is to first find an applicable solution u^∞ to the EEG forward problem, assuming $\sigma(x) = \sigma^\infty \ \forall x \in \Omega$. In a second step, we then want to find a correction function u^c such that the actual potential in Ω is given by $u := u^\infty + u^c$. The crucial point is that, done properly, we do not need to correct u^∞ near the singularity. Instead, we only need to solve a well-posed numeric problem to find u^c and thereby u.

We first want to construct u^∞ and consider equation 2.8 on an unbound homogeneous conductor, i.e., $\mathbb{R}^3$. The problem then reads:

$$\nabla \cdot (\sigma^\infty \nabla u^\infty) = \nabla \cdot (M \cdot \delta_{x_0}) \tag{2.27}$$

In the sense of distributions, this can be solved analytically by:

Definition 5. *(Anisotropic Fundamental Solution) Let $\sigma^\infty \in \mathbb{R}^{3\times 3}$ be symmetric positive definite, let $M, x_0 \in \mathbb{R}^3$ be the dipole moment and position respectively. The solution to equation (2.8) with j^p as in (2.19) is then given by:*

$$u^\infty_{x_0,M,\sigma^\infty}(x) := \frac{1}{4\pi\sqrt{\det \sigma^\infty}} \frac{\left\langle M, (\sigma^\infty)^{-1}(x-x_0)\right\rangle}{\left\langle (\sigma^\infty)^{-1}(x-x_0), x-x_0\right\rangle^{\frac{3}{2}}} \tag{2.28}$$

A comprehensive proof for this established solution [55, 71, 33] can be found in [34].

Previous subtraction approaches [71, 8] directly used the above as the aforementioned base function that needs to be corrected by u^c. Here, the Local Subtraction approach splits off by assuming u^∞ is the solution at the dipole but multiplying it with a continuous cut-off function to get a base function which is zero outside a small, local region around the dipole.

Making this rigorous, we need to define two additional sets. First, we define the patch, a set Ω^∞, such that $U \subset \Omega^\infty \subset \Omega$. Additionally, we define the transition region $\tilde{\Omega} \subset \Omega$ such that $\Omega^\infty \cap \tilde{\Omega} = \emptyset$ and such that we can define a continuous function:

$$\chi : \Omega \to [0,1] \text{ fulfilling } \chi(x) = \begin{cases} 1 & \text{if } x \in \Omega^\infty \\ 0 & \text{if } x \in \Omega \setminus (\Omega^\infty \cup \tilde{\Omega}) \end{cases} \tag{2.29}$$

With this, we define the correction potential $u^c := u - \chi \cdot u^\infty$ and similarly the correction conductivity $\sigma^c := \sigma - \sigma^\infty$. Using the linearity of the differential operators and that by definition $\nabla \cdot (\sigma^\infty \nabla u^\infty) = \nabla \cdot (M \cdot \delta_{x_0})$, we have:

$$\nabla\cdot(\sigma\nabla u) = \nabla\cdot(\sigma\nabla u^c) + \nabla\cdot(\sigma^c\nabla[\chi u^\infty]) + \nabla\cdot(\sigma^\infty\nabla[(\chi-1)u^\infty]) + \nabla\cdot(M\cdot\delta_{x_0}) \tag{2.30}$$

By definition of the EEG forward problem, the left-hand side is equal to $\nabla \cdot (M \cdot \delta_{x_0})$ on the right-hand side. Hence, the other three terms need to fulfill:

$$\nabla\cdot(\sigma\nabla u^c) = -\nabla\cdot(\sigma^c\nabla[\chi u^\infty]) - \nabla\cdot(\sigma^\infty\nabla[(\chi-1)u^\infty]) \quad \text{on } \Omega \tag{2.31}$$

$$\langle \sigma\nabla u^c, n\rangle = -\langle \sigma\nabla[\chi u^\infty], n\rangle \quad \text{on } \partial\Omega \tag{2.32}$$

Where the boundary term follows immediately when substituting $u = u^c + u^\infty$ into it.

Now we can directly see that since by definition $\sigma^c = 0$ on the neighborhood U of x_0 as well as having $\chi(x) - 1 = 0\ \forall x \in \Omega^\infty$, the singularity at x_0 was eliminated from the equations. At this point, we can use the FEM formulation from definition 4 to solve for u^c. If we apply partial integration after moving into the FEM spaces, as detailed in [33], this allows us to compute this final formulation:

Definition 6 (Weak formulation of EEG Local Subtraction approach)**.** *Given the bilinear form $a : H^1(\Omega) \times H^1(\Omega) \to \mathbb{R}$ from definition 4 and defining a linear form $l : H^1(\Omega) \to \mathbb{R}$*

by

$$l(v) = -\int_{\tilde{\Omega}} \langle \sigma \nabla (\chi \cdot u^{\infty}), \nabla v \rangle \, dV - \int_{\partial\Omega^{\infty}} \langle \sigma^{\infty} \nabla u^{\infty}, n \rangle \, v dS - \int_{\Omega^{\infty}} \langle \sigma^{c} \nabla u^{\infty}, \nabla v \rangle \, dV \tag{2.33}$$

Where n is the unit outer normal on Ω^{∞}. Then the continuous Galerkin Local Subtraction approach is given by the problem of finding $u^c \in H^1(\Omega)$ such that $\forall v \in H^1(\Omega)$ we have

$$a(u^c, v) = l(v) \tag{2.34}$$

There are a few important points to note:

Remark 7. *The right-hand side of (2.34) only has support on the closure of Ω^{∞} and Ω^c. Hence, if those sets are chosen to be small in a FEM approach, we arrive at a sparse right-hand side, leading to a significant speed-up.*

Remark 8. *The work from the analytic subtraction approach [8] has been extended such that the functional on the right-hand side can be evaluated completely analytically.*

Remark 9. *Choosing $\Omega^{\infty} = \Omega$, we obtain the classical subtraction approach [71].*

Remark 10. *Existence and uniqueness up to a constant function were shown in [33]. It was also shown that the final u is, in the smooth setting, independent of the choices of $\Omega^{\infty}, \tilde{\Omega}$ and χ. Since these choices, along with the size of U, need to be made in a discrete setting, the dependence on these choices will be investigated.*

Configuration

To implement this dipole model, one must explicitly construct the sets Ω^{∞} and $\tilde{\Omega}$, as well as solve the relevant integrals. Here, we describe the approach implemented in DUNEuro and the configuration options it exposes to the user.

We begin with the construction of the patch set Ω^{∞}. It is built iteratively by adding elements around the dipole position. The root of this iteration can be influenced by the `initialization` parameter. It provides the options `single_element` and `closest_vertex`. The former initializes the patch with the element in which the dipole lies. The latter, on the other hand, finds the closest vertex to the dipole source and adds all elements containing that vertex.

Additionally, there is a boolean `restrict` parameter. If set to `true`, it only allows an element E_{new} with conductivity tensor σ_{new} to be added to the patch set if $||\sigma_{\text{new}} - \sigma^{\infty}||^2 < 10^{-8}$, where $||\cdot||$ denotes the Frobenius norm and σ^{∞} is the conductivity tensor at the dipole position. The existence of this parameter is due to the shared implementation with St. Venant type dipole models and is not part of the Local Subtraction formulation. Therefore, we will always set it to `false`.

Once a root has been established, additional elements are added iteratively. To that end, the `extensions` parameter takes a list of `vertex` and `interface` keywords. DUNEuro processes this list sequentially. If `vertex` is specified, it tries to add all elements that share a node with an element already in the patch. If, on the other hand, `interface` is specified, it only adds elements that share a face with a patch element. The union of the elements added in this way defines Ω^∞. Since the conductivity is constant within the element containing the dipole, this ensures that Ω^∞ always contains the small required neighborhood where the conductivity is constant around the dipole.

The transition region $\tilde{\Omega}$ is lastly implicitly defined as all elements that share a vertex with a patch element but are not themselves part of the patch. This allows the cut-off function to be defined in the piecewise linear function space very easily by setting all degrees of freedom in the patch region to 1 and all remaining ones to 0.

The remaining parameters are Gaussian quadrature orders used to integrate the analytic solution over the patch and transition regions. For the MEG, we will adopt the values used in the original paper [33], namely `intorder_meg_patch = 0`, `intorder_meg_boundary = 6` and `intorder_meg_transition = 5`. Note that the integration order inside the patch is 0, this is because integration over the patch has been transformed into a boundary integral, see also Chapter 6.

While the original implementation [33] also required similar parameters to assemble the linear system for the anisotropic EEG problem, Malte Höltershinken later extended the analytic integration to this case, eliminating the need for these parameters entirely.

2.2.3. The Multipolar St. Venant Approach

Here we describe the Multipolar St. Venant approach, which will be used in later numerical studies and was introduced in [67] by Vorwerk et al. for isotropic volume conductors.

The idea of this approach is to directly model the singular dipole potential through a number of monopole sources on grid nodes. This approach is inherently grid-dependent and as such, we assume we have a discretization $\mathcal{T}_h$ of our head domain.

Given a dipole at a location p^0, we identify the closest grid node p^1 and refer to all nodes which share an element with p^1 as $p^2, \ldots, p^n$. The elements of the set $\{p^1, \ldots, p^n\}$ will be the locations of our monopole sources.

The potential produced by a charge distribution in a vacuum is given by:

$$u(x) := \frac{1}{4\pi\epsilon_0} \int_R \frac{\rho(y)}{||x-y||_2} dy \tag{2.35}$$

where ϵ_0 is the electric vacuum permittivity, $\rho(y)$ is the charge density at point y and $R \subset \mathbb{R}^3$ is an open set containing all points where ρ does not equal 0.

Assuming a discrete charge distribution of N point charges q_i at respective position y^i, this reduces to:

$$u(x) := \frac{1}{4\pi\epsilon_0} \sum_i^N \frac{q_i}{||x - y^i||_2} \tag{2.36}$$

Which can be expressed through a Cartesian multipole expansion around the origin for points sufficiently far from the sources. The terms up to second order are given by:

$$4\pi\epsilon_0 u(x) = \frac{1}{||x||_2} \sum_i^N q_i + \sum_{k=1}^3 \frac{x_k}{||x||_2^3} \sum_i^N y_k^i q_i + \sum_{k,l=1}^3 \frac{x_k x_l}{||x||_2^5} \sum_i^N \left(3y_k^i y_l^i - \left|\left|y^i\right|\right|_2^2 \delta_{k,l}\right) q_i + ... \tag{2.37}$$

The Multipolar St. Venant approach assumes that the potential from its monopole distribution is given by these three first terms, developed around the dipole location. They contain the monopole moment, dipole moment and quadrupole moment, respectively given by:

$$M := \sum_i^N q_i \quad p := \sum_i^N \Delta p^i q_i \quad Q_{k,l} := \sum_i^N \left(3\Delta p_k^i \Delta p_l^i - \left|\left|\Delta p^i\right|\right|_2^2 \delta_{k,l}\right) q_i \tag{2.38}$$

Where $\Delta p^i = p^i - p^0$ is the position of the monopoles relative to the dipole position. Similarly, one can express the potential of a true point dipole in a Cartesian multipole expansion and match these moments to determine the monopole strength. The approach as implemented in DUNEuro, however, requires a rescaling with a_{ref}, which needs to be at least twice the element edge length and such that $\forall 1 \leq i \leq n$ and $\forall 1 \leq j \leq 3$, we have $\Delta p_j^i \cdot a_{ref}^{-1} < 1 \; \forall 1 \leq i \leq n$ and $\forall 1 \leq j \leq 3$. With that, we define:

$$\bar{M} := M \cdot a_{ref} \quad \bar{p} := p \cdot a_{ref} \quad \bar{Q}_{k,l} := Q_{k,l} \cdot a_{ref} \quad \bar{\Delta p^i} := \Delta p^i \cdot a_{ref} \; \forall 1 \leq i \leq n \tag{2.39}$$

Then the monopole strengths q^i need to fulfill:

$$\begin{bmatrix} \bar{M} \\ \bar{p}_1 \\ \bar{p}_2 \\ \bar{p}_3 \\ \bar{Q}_{1,1} \\ \bar{Q}_{2,2} \\ \bar{Q}_{3,3} \\ \bar{Q}_{1,2} \\ \vdots \end{bmatrix} = \begin{bmatrix} 1 & \cdots & 1 \\ \bar{\Delta p_1^1} & \cdots & \bar{\Delta p_1^n} \\ \bar{\Delta p_2^1} & \cdots & \bar{\Delta p_2^n} \\ \bar{\Delta p_3^1} & \cdots & \bar{\Delta p_3^n} \\ 3(\bar{\Delta p_1^1})^2 - \left|\left|\bar{\Delta p^1}\right|\right|_2^2 & \cdots & 3(\bar{\Delta p_1^n})^2 - \left|\left|\bar{\Delta p^n}\right|\right|_2^2 \\ 3(\bar{\Delta p_2^1})^2 - \left|\left|\bar{\Delta p^1}\right|\right|_2^2 & \cdots & 3(\bar{\Delta p_2^n})^2 - \left|\left|\bar{\Delta p^n}\right|\right|_2^2 \\ 3(\bar{\Delta p_3^1})^2 - \left|\left|\bar{\Delta p^1}\right|\right|_2^2 & \cdots & 3(\bar{\Delta p_3^n})^2 - \left|\left|\bar{\Delta p^n}\right|\right|_2^2 \\ 3\bar{\Delta p_1^1}\bar{\Delta p_2^1} & \cdots & 3\bar{\Delta p_1^n}\bar{\Delta p_2^n} \\ \vdots & \ddots & \vdots \end{bmatrix} \cdot \begin{bmatrix} q^1 \\ q^2 \\ q^3 \\ \vdots \\ q^n \end{bmatrix} \tag{2.40}$$

We call the vector on the left-hand side $\bar{t}$, the used matrix $\bar{X}$ and the remaining vector q. Where we require, to match the original dipole, with moment m, that:

$$M := 0 \quad p := m/a_{ref} \quad Q_{k,l} := 0 \tag{2.41}$$

The amount of monopoles is mesh-dependent but usually underdetermined, hence to reach a unique solution, we need an additional regularization term. A physiologically plausible approach is to minimize the energy. To do so, we define:

$$\bar{W} = \mathrm{diag}(\left|\left|\bar{\Delta p}^1\right|\right|_2, \cdots, \left|\left|\bar{\Delta p}^n\right|\right|_2)^{\frac{r}{2}} \text{ for } r \in \{1, 2\} \tag{2.42}$$

Then q is now the unique minimizer of:

$$F_\lambda(q) = \left|\left|\bar{t} - \bar{X}q\right|\right|_2^2 + \lambda \left|\left|\bar{W}q\right|\right|_2^2 \tag{2.43}$$

Remark 11. *Regarding the choice of the parameters, we will follow [2], using $r = 2$, $a_{ref} = 20mm$ and $\lambda = 10^{-6}$.*

Having obtained the monopole strengths and locations, one may now construct a sparse right-hand side vector for the FEM forward problem from definition 4. To do so, simply set the right-hand side entry associated with node p^i to q^i and the remaining entries to 0.

Remark 12. *For highly eccentric sources, chosen monopole sources may lie on the boundary or in a different compartment than the considered source space. To avoid this invalidation of assumptions, it is customary to reject monopole locations which lie on the boundary or in another compartment relative to the true dipole.*

Remark 13. *This approach does not consider the source space anisotropy for its dipole representation.*

Remark 14. *This formulation suffers from frequent outliers when simulating dipoles, which will be evident in the following. It should be acknowledged, however, that recent considerations from Malte Höltershinken could reduce the number of outliers significantly. The issue with this formulation is that the constructed right-hand side does not necessarily fulfill the required discrete Neumann compatibility condition to get a unique solution. Leaving out higher moments when not enough valid mesh nodes are available can help maintain this compatibility and thus ensure that a unique solution is found.*

Due to time constraints, it was not possible to include the evaluation of this promising idea in this work, although it might improve the performance of the St. Venant type approaches.

2.3. Anisotropic Brain Conductivities

It is well-established that the human brain is not an isotropic medium due to the fibrous nature of its neurons. Consequently, the brain exhibits anisotropic conductivities.

These conductivities are, however, hard to obtain due to the highly individual structures and the difficulty of obtaining invasive measurements in human subjects. However, studies have shown that electrical conductivity tensors correlate with the diffusion tensors obtained from Diffusion Tensor Imaging (DTI) using Magnetic Resonance Imaging (MRI) machines. They also provide methods to estimate the electrical conductivity from the diffusion tensors.

The method on which our assumptions are based is the effective medium approach, developed and validated in [68, 62, 3]. It relates the two tensors through the statistics of the mediums microstructure, which are estimated from the DTI data, formally utilizing a statistical correlation expansion. Note that this provides an estimate of the conductivity tensor that is still based on a single isotropic parameter that also needs to be estimated.

However, studies have found non-negligible results when anisotropic conductivities were modeled [72, 74, 30, 26, 27], with anisotropies close to the source being particularly significant. This research, however, focused mostly on white matter and skull anisotropies, for which good DTI data was available.

In [21], Drechsler et al. presented a preliminary validation of FEM-based forward approaches for modeling anisotropy in the source space. We aim to expand upon this work and will, therefore, use the same parameters that they presented.

To align with the requirements for the analytic solutions of the sphere model [16, 17], we model anisotropy using specific tensors, acknowledging that the actual conductivity is more complex. We first define the required canonical directions as follows:

Definition 15 (Radial and tangential directions)**.** *For a point y on the boundary between the CSF and gray matter compartments, we denote the unit normal pointing from the gray matter to the CSF as n_y. For a point x in the gray matter, we define the* ***radial direction*** *to be n_y where y is the point on the boundary that is closest to x.*
Any vector orthogonal to the radial direction is said to point in a ***tangential direction****.*

These definitions allow us to define the tensors used in the following to model conductivity:

Definition 16 (Conductivity tensor)**.** *A* ***conductivity tensor*** *at a point x in the gray matter is a symmetric positive definite matrix $\sigma \in \mathbb{R}^{3\times 3}$, such that its eigenvector with the largest eigenvalue points in the radial direction and its other eigenvectors point in tangential directions with identical eigenvalues. We refer to the largest eigenvalue as* ***radial conductivity*** *σ_r and to the remaining one as* ***tangential conductivity*** *σ_t. Further, we call the quotient $\frac{\sigma_r}{\sigma_t}$ the* ***anisotropy ratio****.*

Table 2.1.: Anisotropy ratios of studied models.

Model	Anisotropy ratio $\frac{\sigma_r}{\sigma_t}$
Adult	1.41
Child	2.7
Premature baby	5

Remark 17. *This means our conductivity tensor for a point x in the gray matter is fully determined by the size of one of its eigenvalues and the anisotropy ratio.*

The work of Drechsler et al. was based on research with 7T MRI machines showing evidence that the gray matter compartment in adults exhibits anisotropy [31, 13, 39, 58]. This is especially important for EEG source localization since we assume the dipolar source lies in the gray matter. Hence, inaccuracies in its conductivity can directly bias the reconstruction of cortical current sources. For adults, the highest measured anisotropy ratio was 1.41:1 from [58]. Consequently, we will use this ratio for our adult models.

While these findings are significant for adult models, it is important to consider how the brain develops in the first years of life, as it undergoes massive changes affecting gray matter anisotropy as well. For premature infants of 26 weeks, studies [50, 49] showed a much-increased gray matter anisotropy, the correct modeling of which could prove important for studying such young humans with source localization. We assume upper limits of the anisotropy ratio for the premature infant model here as 5:1 and for our child model as 2.7:1, to match the previous publication [21]. A summary of the used ratios can be found in Table 2.1.

3. Methods

This work focuses primarily on evaluating the Multipolar St. Venant approach and Local Subtraction approach in a multitude of simulation studies. The following sections detail the shared underlying computational setup and tools common to all studies. While individual studies will reference these foundational tools, each also contains a dedicated Methods section to discuss the exact study specific parameters and configurations.

3.1. Error Measures

In EEG and MEG source analysis the forward models produce high-dimensional vectors containing the predicted sensor results as outputs. To understand the nature of the differences between two outputs, the following error measures have been established [46].

Definition 18 (Source analysis error measures)**.** *Let V be a vector space with norm $||\cdot||$ and let $v, w \in V$, then we define the relative error (RE) as:*

$$RE(v,w) := \frac{||v-w||}{||w||} \tag{3.1}$$

The magnitude error (MAG):

$$MAG(v,w) := \frac{||v||}{||w||} \tag{3.2}$$

The logarithmic magnitude error (lnMAG):

$$lnMAG(v,w) := \log\left(MAG(v,w)\right) = \log\left(\frac{||v||}{||w||}\right) \tag{3.3}$$

And the relative difference measure (RDM):

$$RDM(v,w) := \left|\left|\frac{v}{||v||} - \frac{w}{||w||}\right|\right| \tag{3.4}$$

Typically, the vectors v and w represent the measured potentials at EEG or MEG sensors in $\mathbb{R}^n$ and the standard Euclidean norm is used.

The RE measures the overall difference between two measurements. By making the error relative to one measurement, it allows for a comparison across different experimental

Table 3.1.: Four-layer sphere reference model.

Compartment	Radius	Isotropic conductivity
Skin	88 - 92 mm	0.43 $\frac{S}{m}$
Skull	80 - 88 mm	0.01 $\frac{S}{m}$
CSF	76 - 80 mm	1.79 $\frac{S}{m}$
Brain (adult)	0 - 76 mm	0.33 $\frac{S}{m}$
Brain (child)	0 - 76 mm	0.51 $\frac{S}{m}$
Brain (premature baby)	0 - 76 mm	0.59 $\frac{S}{m}$

setups, such as those with varying sensor counts. This made the RE a common benchmark for comparing different forward modeling approaches and serves as an all-encompassing measure, though it does not provide insight into the nature of the difference.

The RDM removes scaling issues by comparing only the normalized vectors. It is specifically intended to capture topography errors in the results, such as wrong peak location or incorrect slopes in the change of the electric potential or magnetic field. Such errors are often correlated to subsequent positional errors in the reconstructed sources [14].

The lnMAG is blind to component-wise differences between measurements, as it only compares the total signal magnitude. It is a tool to diagnose scaling errors in simulations or to interpret results concerning the depth precision and strength of a reconstructed source.

Mathematically one should be aware that only the RDM is symmetric in its arguments, ranging from 0 to 2, while lnMAG fulfills $\mathrm{lnMAG}(v, w) = -\mathrm{lnMAG}(w, v)$ with values in $\mathbb{R}$. The relative errors $\mathrm{RE}(v, w)$ and $\mathrm{RE}(w, v)$ are independent in general, with values in $\mathbb{R}$ as well.

3.2. Meshing

For the later study of finite element methods, we need to construct meshes of the respective domains and assign them conductivity tensors.

It has been shown that the local mesh density introduces a bias in favor of certain potential approaches [41, 19]. In [41] it was found that a balanced mesh benefits direct approaches such as the St. Venant approaches, while a finer mesh around conductivity jumps benefited the full subtraction approach. Recently, [33] has shown that the Local Subtraction approach is less sensitive to the global mesh structure compared to the full subtraction approach. Instead, it performed best on the grid that was designed to favor the St. Venant approaches. This is probably linked to its now sparse and therefore local right-hand side, similar to St. Venant approaches.

For the validation of the numeric approaches in a four-layer sphere model, we enforced a homogeneous mesh size due to this development and to reduce the overall number of variables. We generated meshes of the four-layer sphere model using GMSH[1][23], parametrized as in Table 3.1 to conform with our reference [21]. It used a Delaunay-type algorithm to generate meshes with target element side lengths of 4, 2 and 1 millimeters. In the following, they will be referenced as *rough_mesh*, *mid_mesh* and *fine_mesh* respectively. In GMSH, this means locally constraining the average side length of the tetrahedral elements to the given value. Note that this was not a refinement and when moving to a finer grid, additional benefits of a more precise approximation may influence the results.

In the later sections, a realistic calibrated head model has been investigated, which was provided to the author. It is the same mesh used in [33][2] with more precise data and measured sensor positions.

Due to the difficulties in creating adequate meshing, GMSH did not quite achieve our desired meshing resolution. Hence, the actually obtained values are presented in Table 3.2.

Table 3.2.: Average element side length in the used meshes. Gray M. and White M. are short for gray matter and white matter respectively.

	rough_mesh	**mid_mesh**	**fine_mesh**	**realistic mesh**
Skin	4.28	2.35	1.29	2.6592
Skull	4.69	2.56	1.32	-
Compacta	-	-	-	1.6301
Spongiosa	-	-	-	1.5117
CSF	4.3	2.37	1.29	1.3491
Brain	5.38	2.7	1.36	-
Gray M.	-	-	-	1.6367
White M.	-	-	-	1.9878

3.3. Electrodes

We used two distinct methods to obtain the electrode positions for our volume conductor models.

[1]The used meshing scripts can be found at `https://gitlab.dune-project.org/timon.gronotte/thesis-experiments/-/tree/main/src/mesh_tools/mesh_scripts?ref_type=heads`

[2]Their mesh can be found at `https://doi.org/10.5281/zenodo.12575552`. The mesh used here is not currently publicly available.

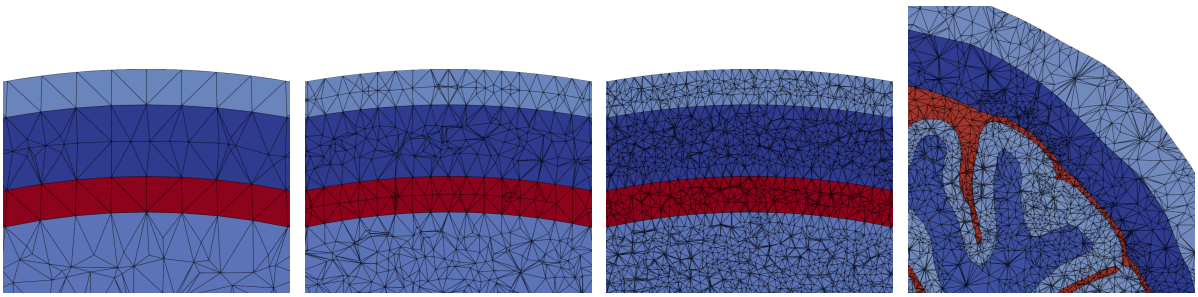

(a) (b) (c) (d)

Figure 3.1.: Subfigure (a) shows `rough_mesh`, (b) shows `mid_mesh`, (c) shows `fine_mesh` and (d) shows our realistic head model, with differently colored compartments.

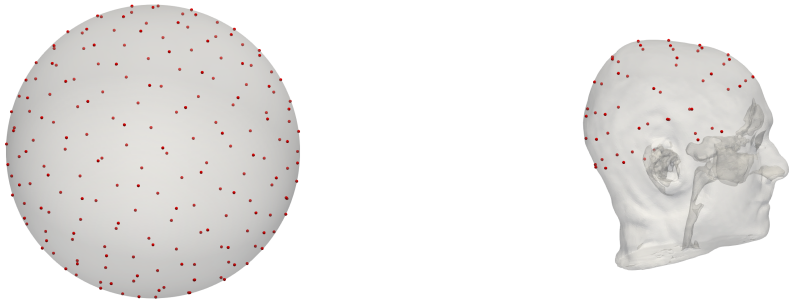

(a) (b)

Figure 3.2.: (a) shows the electrode positions on `mesh_mid` and (b) on the realistic head model.

For our sphere models, we generated points on the outermost sphere using a Fibonacci lattice [25]. This method produces a set of N points that are approximately evenly distributed on the spherical surface. In practice, our results were obtained using a lattice of 500 points. These positions were then adjusted by shifting them to the nearest surface node on the mesh using DUNEuro tools[3].

In contrast, the realistic head model we used was provided with a pre-existing set of 57 digitized electrode positions.

The electrode configurations for both models are shown in Figure 3.2.

[3]The electrode placement implementation can be found at: `https://gitlab.dune-project.org/timon.gronotte/thesis-experiments/-/blob/main/src/aniso_tests/electrode_creator.py`

3.4. Conductivity Tensors

All simulations that we will carry out require us to specify conductivities throughout the model.

Our analytical investigations into four-layer sphere models, based on the results from DeMunck et al. [16, 17], simply require us to specify the eigenvalues of the conductivity tensors, from definition 16, per compartment.

Transitioning to numerical solving using finite element methods, we need to represent the conductivity on the mesh of our domain. The DUNEuro toolbox, which implements the investigated approaches, chose to attach one conductivity tensor to each element in the mesh that we need to construct.

In the sections involving spherical volume conductor models, elements in isotropic compartments were assigned an appropriately scaled identity matrix. To construct the anisotropic tensors with given radial and tangential conductivity for an element, we first calculated the element barycenter and get its position relative to the sphere center in radial coordinates. Then we constructed a diagonal matrix with the conductivities on the diagonal for which we explicitly calculated the rotation matrices to receive the desired symmetric positive definite tensor from the aforementioned radial coordinates[4].

In the sections involving realistic head models, the approach to isotropic compartments remains unchanged. But in the case of an anisotropic gray matter compartment, it is not clear how we correctly obtain the tensors. As mentioned before, modern FEM approaches that consider white matter anisotropy inform the tensor construction with Diffusion Tensor Imaging [73]. While the inclusion of measured patient data would ultimately be a goal, we did not have access to such data for this work and hence needed to artificially create reasonable tensors. For these early tests, we chose the following ad hoc methodology to adhere to our definition of conductivity tensor.

To construct the tensors in a given labeled mesh, we first isolate the surface between the gray matter and surrounding compartments and computed per-element outward normals. With those, we were able to use the same algorithm for elements at the gray matter border as for elements in the sphere models to construct their anisotropic tensors. For elements that lie deeper in the compartment, we assigned them the tensor that was constructed for the nearest border element.

There is a known issue with this procedure. If a border element has more than one side that lies on the border, the computed element normal could point in any direction. This issue did not affect the used meshes and due to its late discovery, the issue still persists in the script[5].

[4]The implementation for placing tensors in spheres can be found at: `https://gitlab.dune-project.org/timon.gronotte/thesis-experiments/-/blob/main/src/aniso_tests/anisotropy_creator.py`

[5]The implementation for placing tensors in arbitrary but labeled head models can be found

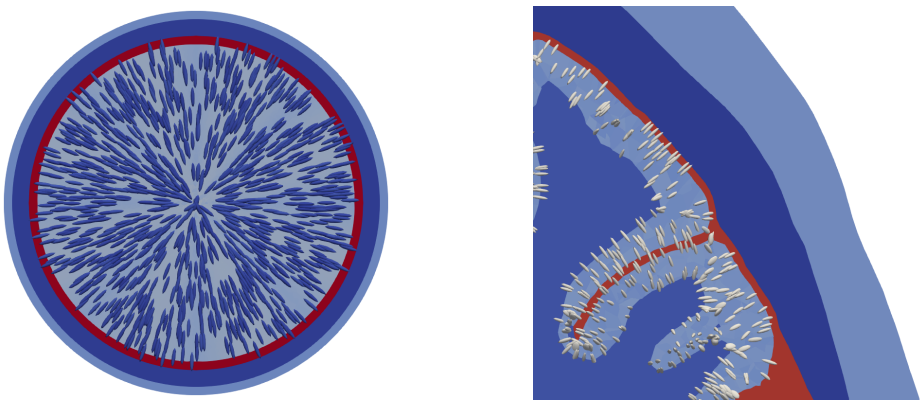

(a) (b)

Figure 3.3.: Subfigure (a) shows a visualization of the generated anisotropic tensors of a premature infant. (b) shows the tensors generated in our realistic head model.

In any case, this approach is quite simplistic and warrants its own investigation into how to best construct these tensors, especially for deeper elements.

3.5. Dipoles

In the sections involving spherical volume conductor models, dipoles were created[6] by pseudo-randomly generating points on the unit sphere using a zero-seeded `numpy.random`. These points were then scaled to the given eccentricities and assigned a moment. Note that this process does not consider the St. Venant condition. In this context, the St. Venant condition means that a dipole can only be placed at positions where the nearest mesh node belongs solely to elements within the gray matter.

Radial dipoles were assigned the unit length vector used to generate their position, while tangential moments were constructed by finding an orthogonal vector to the generating vector. Additionally, a set of dipoles with arbitrary orientation, referred to as mixed dipoles, was generated by sampling another set of random unit vectors.

Note that unless otherwise specified, each test configuration for sphere models consisted of 1000 dipoles with unit strength. The typically used eccentricities can be found in Table 3.3.

For realistic head models, we relied on an internal tool to generate dipole positions in

at: `https://gitlab.dune-project.org/timon.gronotte/thesis-experiments/-/blob/main/src/realistic_tests/tensor_sculptor.py`

[6] The script for dipole placement in spherical head models can be found at: `https://gitlab.dune-project.org/timon.gronotte/thesis-experiments/-/blob/main/src/aniso_tests/dipole_creator.py`

Table 3.3.: Usually used eccentricities in % of brain radius and in mm. For brain radius see Table 3.1.

ecc in %	0.85	0.9	0.936	0.9639	0.9778	0.9848	0.9883	0.99
ecc in mm	64.6	68.4	71.136	73.2564	74.3128	74.8448	75.1108	75.24

the gray matter. It constructs a bounding box around a head model and inserts a regular grid, in our case with a spacing of $1.4mm$. The points of this grid represent potential dipole positions and as such, all points that do not lie in the gray matter compartment were removed. We further chose to reject points that lie within $0.5mm$ of a compartment boundary and then enforce the St. Venant condition.

These dipole positions were then assigned a unit moment on the radial axis pointing to the nearest compartment boundary, reusing the computations from the tensor creation[7].

3.6. Software

The numeric simulations were run with DUNEuro [57, 7, 70], a finite element solver toolbox for EEG and MEG source reconstruction. It is based on the DUNE C++ library [6, 9, 10, 5, 4]. For an introduction, the book [54] is highly recommended. Otherwise, see the official website `https://www.dune-project.org/`. For the generation of additional tetrahedral meshes, GMSH [24] was used.

The analytic forward simulations were carried out with an adapted version of SimBio[8] [59], which implemented the results from De Munck and Peters [17].

The above software was interfaced using Python interfaces, along with NumPy [29], Pandas [60, 45] and SciPy [64]. For the data visualization, Matplotlib [37] and ParaView [1] were used. The precisely used versions can be found in the testing repository[9] or individually linked tests. Note that all links will reference the latest version of the code. However, all repositories will contain a version tag for reproducibility.

[7] The script for moment assignment given dipole positions can be found at: `https://gitlab.dune-project.org/timon.gronotte/thesis-experiments/-/blob/main/src/realistic_tests/source_space_sculptor.py`

[8] See implementation: `https://gitlab.dune-project.org/timon.gronotte/simbiosphere/-/tree/AnisotropicInterface`

[9] `https://gitlab.dune-project.org/timon.gronotte/thesis-experiments`

4. Numerical Considerations in FEM Source Modeling

4.1. The Effect of Dipole Positioning Strategies

Numerical simulations naturally involve representing the dipoles on the mesh. The Local Subtraction approach has the theoretical guarantee to provide the best approximation of its correction potential in the first-order Sobolev norm. However, the approach implicitly depends on the mesh, as in actual use, we need to construct the patch and transition sets from the mesh, which discretely contains the conductivity and stores our data. The Multipolar St. Venant approach, in contrast, explicitly depends on the mesh to create an approximation of the dipole. As such, the mesh structure around the dipole is of vital importance for both approaches to achieve a good approximation.

For the older full subtraction [71] and Buchner St. Venant [12] approaches, Johannes Vorwerk investigated the dipole placement relative to the mesh in his Diploma thesis [65]. Finding that the Buchner St. Venant approach tends to perform best when dipole locations are placed on mesh nodes, while the full subtraction approach performed best with sources in the element barycenter.

His findings informed the dipole choices of our reference publication [21]. Prompting us to reevaluate if these findings remain accurate for the Local Subtraction and St. Venant approaches and to understand any potential bias our chosen positions might introduce. Specifically, dipoles in the barycenter or on the nodes of elements were tested against arbitrary placements.

Methods

To study the mesh dependence, `mid_mesh` from Section 3.2 was selected and adorned with isotropic premature conductivities from Table 5.1. For anisotropic testing, these conductivities were assumed in the radial direction and the tangential conductivity was scaled according to Table 2.1. The tensors were then placed as described in Section 3.4.

On this mesh, 1000 dipoles per eccentricity from Table 3.3 were generated using one of the following strategies. The first option, referred to as `unconstrained`, uses the dipoles directly as they are created by the process from Section 3.5. Besides that, we called `nodes` the strategy where we move each dipole to the closest node in the mesh that lies

fully in the brain compartment before calculating various moments[1]. Further, we have a process that moves each dipole location to the closest barycenter of a mesh element fully in the brain compartment. We refer to this simply as `barycenter`. All strategies are based on and implemented in the dipole creation script presented in Section 3.5. Furthermore, while the closest barycenter or node to a given generated location was taken for the restrictions, this means that the eccentricities shown in the plots are not completely accurate for constrained sources.

Numeric solutions are calculated using the St. Venant approach and the Local Subtraction approach[2]. The relative errors against the analytic solution at the new position are calculated as the measurement of the resulting effects.

Results

In Figure 4.1(a), we see results from the Local Subtraction approach with isotropic conductivity and radial dipoles, showing overall very good relative errors regardless of source location. If we were to compare the numeric solution of a dipole after applying a restriction strategy to the analytic solution at its original position, we saw relative errors around a median of 0.023. One may also see that for all eccentricities larger than 0.94, the `node` errors appear to be exactly identical. This is in fact the case, since due to the mesh side length of approximately $2mm$ and the exclusion of nodes in the compartment boundary, the closest available node in this $3mm$ range is nearly always the same. To a lower degree, a similar effect is true for the `barycenter` approach.

Figure 4.1(b) shows a nearly identical test scenario, where the only difference is the usage of the Multipolar St. Venant approach. This approach shows a more pronounced effect of the dipole location, showing the best results if they are placed on `nodes` and the worst if the source lies in a `barycenter`. For readability of the plot, the y-axis of the plot is limited at 0.01, which hides some of the simulation results. It is of note, however, that in the case of placement only on `nodes`, no data needed to be cut.

Figures 4.1(c) and (d) show again respectively the two approaches but with an anisotropic gray matter compartment. Additionally, the plots show the relative error of the numerically computed potentials against the analytically computed potentials from the original position before a restriction has been applied. Those are indicated by the suffix "against original". First to note is the different error scale compared to the isotropic case. The Local Subtraction approach shows for the deeper eccentrics below 0.97 the best results for dipoles at the `barycenters` while producing distinctly bigger errors for dipoles at the `nodes`. This effect seems to disappear for higher eccentricities,

[1] At the time of writing, the Local Subtraction approach implementation in DUNEuro is not able to deal with dipoles exactly at the node locations. To mitigate this, we moved the dipoles that should lie on nodes in a random direction by at most $0.02mm$.

[2] The implementation can be found under: `https://gitlab.dune-project.org/timon.gronotte/thesis-experiments/-/tree/main/07_dipole_poition`

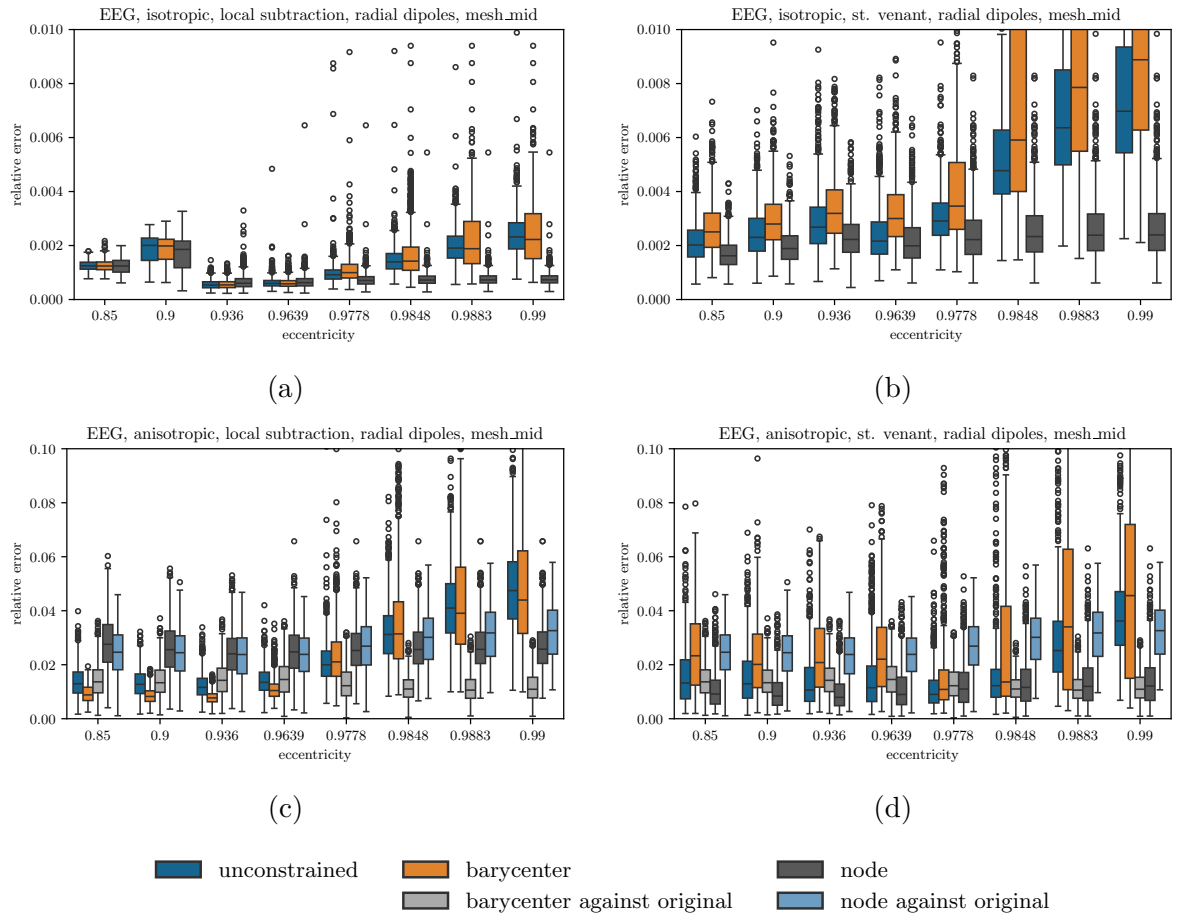

Figure 4.1.: Relative error for different dipole positioning schemes in the EEG case for 1000 radial dipoles at different eccentricities. (a) shows the results in an isotropic volume conductor using a Local Subtraction approach. (b) shows the same for a St. Venant approach. (c) shows the results in an anisotropic volume conductor with a 5:1 ratio using a Local Subtraction approach. (d) shows the same for a St. Venant approach. The anisotropic plots also show the relative error against the analytic solution at the original dipole location. This is missing from the isotropic plots since the errors are nearly identical in magnitude to the anisotropic ones. Note here the otherwise different orders of magnitude between isotropic and anisotropic results.

while the lack of available nodes fully in the brain compartment keeps the error of the `nodes` strategy small. For the St. Venant type approach, we consistently see significantly lower errors for the dipoles at `nodes`, again also due to the lack of nodes fully in the gray matter at high eccentricity. Regardless, no outliers from the St. Venant approach needed to be cut when the dipole lies at a `node`, which was not true when moving dipoles to `barycenters`, which produces consistently the highest errors at all eccentricities. Notably, for all eccentricities below 0.99, the median error of `unconstrained` dipoles is lower than the errors against the original position.

Note that the same plots are available for tangential sources in Figure A.1, but not discussed due to the similarity to radial results.

Discussion

The dipole placement test showed a connection between dipole position, mesh and observed errors, in line with previous work [65]. It has to be noted, however, that only a single realistically resolved grid has been considered, with the comparatively high conductivity values and anisotropy ratios from a premature baby. Hence, deeper conclusions are left to a dedicated work, taking the important mesh resolution into account.

In the isotropic case, an effect of dipole placement relative to the mesh was only observed for the Multipolar St. Venant approach. However, the resulting errors are generally so small that they bear little practical significance. That we see basically no differences for the Local Subtraction approach, might correlate with the absence of conductivity jumps close to the dipoles. Nevertheless, the pronounced outlier reduction of the Multipolar St. Venant approach when dipoles were placed on mesh nodes prompts a question for future research. What advantages could be achieved in realistic head models by linking mesh creation and source-space generation to intentionally position dipoles only on nodes?

In the anisotropic case, the effect was more pronounced, possibly due to the conductivity jumps in between elements, which may also be the cause of the generally much bigger errors. While at low eccentricities not moving the dipoles has a significant advantage over moved dipoles if compared to the original position, for higher eccentricities within $1mm$ of the brain compartment border, the relative error of a moved and unmoved dipole are nearly identical. This makes the sub-millimeter distinction of eccentricity futile in the anisotropic case on this mesh.

From this, we took away that in isotropic meshes, it is best to leave dipoles at their original position and it can be useful to consider dipoles that are closer than the element side length, not warranting very high mesh resolutions. This is grounded in the overall very small errors, which are of no practical concern. In the anisotropic case, restricting to specific dipole locations can provide advantages for either approach. To keep the dipole

positioning bias as low as possible and keep consistent with testing methods from other publications, we choose to use dipole positions that are generated independently of the mesh, as errors remain reasonable.

4.2. Assessment of Local Subtraction Patch Sizes

The original Local Subtraction paper [33] included some recommendations on how to construct the underlying sets in section 5.1. As the original investigation considered one spherical mesh and two local refinements with dipoles at a fixed eccentricity of 99% of the brain radius, we wanted to expand on these results.

Methods

To do so, we took the previously described meshes `rough_mesh`, `mid_mesh` and `fine_mesh` of the sphere model described in 3.1 and imbued them with the isotropic conductivity values of an infant. Together with a set of 1000 dipoles for each eccentricity from Table 3.3, we computed the potentials at the EEG sensors with the Local Subtraction approach using 0 to 10 vertex extensions with `initialization` set to `single_element` and then computed the errors against the analytical solution[3].

Results

First, we presented a qualitative look at the data in Figure 4.2 (a), (b) and (c). They showed the mean relative errors that were achieved by our tests on different grids, without error bars for readability. Note that these plots are also provided for a tangential source in Figure A.2 but are not deeply examined due to the similarities to the results for radial sources.

Figure 4.2 (a) showed the results for `rough_mesh`. Across all eccentricities, the error initially decreased before a peak at 3 to 4 vertex extensions before settling at a relatively consistent mean error. The peak was between two and three times as high as the respective consistent levels, where higher eccentricities produced a comparatively higher mean error. Notably, the dipoles at 85% of the brain radius showed a smaller peak that was shifted to 5 vertex extensions.

Figure 4.2 (b) displayed the results from `mid_mesh`. Again, all mean errors showed a slight decrease until they peaked around 6 to 9 vertex extensions, after which we saw a decrease in errors again. Here we saw that the dipoles between eccentricities of 85% and 90% of the brain radius showed a much smaller peak at 4 vertex extensions, as well as a potential peak or increase at the end of the plotted range. The peaks or increases of

[3]The implementation can be found under: `https://gitlab.dune-project.org/timon.gronotte/thesis-experiments/-/tree/main/08_vertex_extenstions`

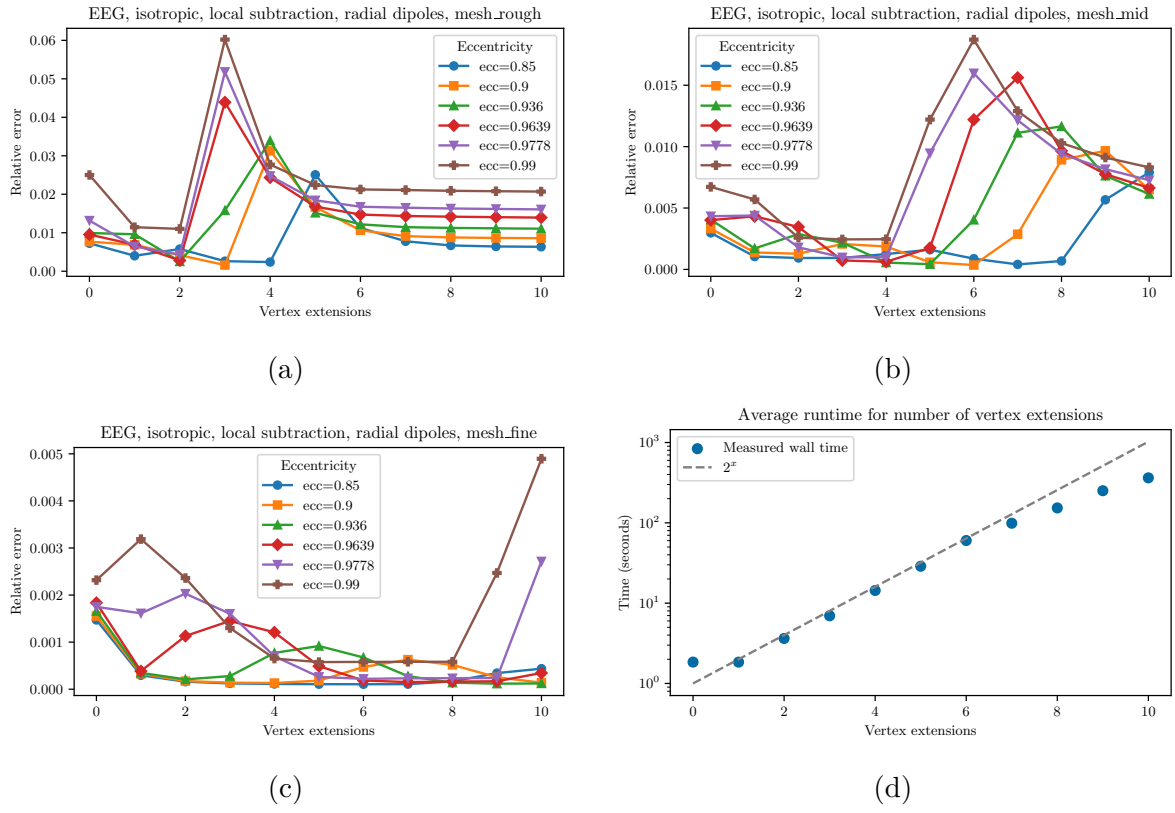

Figure 4.2.: Figures a,b,c show the EEG mean relative error for 1000 radial dipoles at different eccentricities and vertex extensions, without error ranges. (a) shows the results on `rough_mesh`, (b) on `mid_mesh` and (c) on `fine_mesh`. In (d) the average runtime in seconds for simulating 1000 dipoles is displayed in relation to the used number of vertex extensions.

relative error at the end of the plotted range were around two to three times higher than the mean errors before the increase, where again, higher eccentricities produced bigger errors.

Lastly, Figure 4.2 (c) showed more complicated behavior in the results from `fine_mesh`. The deepest eccentricity showed a nearly constant mean error. However, as sources got closer to the surface, errors increased as before and showed up to two peaks in the plotted range.

Figure 4.2 (d) showed the average wall time that was needed to compute a set of 1000 dipoles at different values of vertex extensions on `mesh_fine` with a logarithmic y-axis. We also plotted 2^x for reference.

Due to suspecting an interaction when the patch region of a dipole first intersects other compartments, we produced the plots from Figure 4.2 for dipoles lying on the line $\textit{sphere center} + c \cdot (-0.872,\ 0.419,\ -0.25)^T\ \forall c > 0$ at the previously considered eccentricities. The resulting plots are shown in Figure A.6 in the appendix and showed the same pattern as previously described. For the dipoles on said line, it was also explicitly checked that the respective large peaks occurred when there was a two-dimensional intersection between the patch region and the skin compartment.

Additionally, the potentials produced by the dipole on the above-mentioned line at an eccentricity of 99% on `mesh_mid` were visualized on a plane through the head model. Figure A.7 shows said potentials at four vertex extensions right before the peak that we found in Figure A.6 and at five extensions, right at the peak. Notice the smooth full potential at four extensions in the skin compartment and the jumping full potential at the skull-to-skin boundary, as well as the vastly different correction potentials at this interface.

Lastly, we showed the full test results in Figures A.3, A.4 and A.5. These plots additionally displayed the deviation from the mean in our sample, showcasing that the deviation in the samples was initially large for no vertex extensions but decreased until hitting the peaks from Figure 4.2. At those peaks were increases in deviation, after which the spread contracted again but in these samples stayed at a higher level than was achieved before the peak.

Discussion

The pattern that we observed for Figure 4.2 (a) fitted perfectly with the results and analysis from the original Local Subtraction paper [33]. We saw an initial decrease in errors as we could better describe the behavior near the singularity before we saw a sharp increase when the patch grew into the skin compartment. This was followed by a drop in mean error as we approached a full subtraction approach [71]. This equally applied to 4.2 (b), where a peak was in the plotted range.

Figure 4.2 (c), which showed the results for `fine_mesh`, seemed to show the emergence

of further effects. We saw the highest peaks at 10 vertex extensions. This seemed to correlate with the patches of the most eccentric sources intersecting the skin compartment, while the plotted range forbade solid conclusions. Most skin compartment intersections were, however, far outside the plotted range. Further, the plot showed for highly eccentric sources a drop from the initial mean error that was qualitatively more pronounced than in the rougher meshes, as well as an additional small peak for the less eccentric sources. This coincided for the aforementioned test dipole with at most two-dimensional intersections between patch region and CSF compartment. Notably, the transition when the patch grew from CSF to skull compartment did not seem to produce a visible perturbation in the data, although it had the biggest jump in conductivity. Potentially, this could be connected to the fact that, in contrast to the other two transitions, the conductivity dropped from the CSF to the skull.

Overall, the results supported the recommended two vertex extensions for superficial to deep sources on meshes with an average side length of roughly $2mm$ and $4mm$. The test on our finest mesh with an average element side length of $1mm$ showed, however, that for sources close to the conductivity jump from gray matter to CSF, bigger patches were required to achieve optimal results.

Considering the results from all three resolutions, one might not recommend a fixed amount of vertex extensions but rather a radius around the dipole. Assume that the method of creating the patch region via vertex extensions leads to a roughly spherical patch region around the dipole and further assume the number of vertex extensions times the average element side length gives an estimate of the radius of said sphere. In that case, we would see that the initial error decrease flattened out at roughly $10mm$ on all meshes. The following increases after flattening out seemed to be individually bound to the distance between the dipole location and conductivity jumps. In the presented results, the jump between the skull and skin compartment produced the most significant artifacts, which should in practice be more than $10mm$ away from the dipole. This motivated recommending a patch that has a radius as close as possible to but not over $10mm$. Such a recommendation would be easy to implement as an alternative to the vertex extensions and seems natural as spatially smaller regions with zero correction conductivity need to approximate the potential closer to the singular source.

However, the time plot in Figure 4.2 (d) showed a great impact on computation time if more vertex extensions were used. Considering the size of the errors even at the peaks, time concerns might impact practical applications far greater and incentivize choosing a few fixed vertex extensions.

Very interesting were also the vastly changing correction potentials found in Figure A.7. This might be caused by the need for the correction potential to correct the infinity potential with large negative values followed by large positive values when the entire potential needs to be approximated outside the patch. Additionally, this occurred at a large conductivity jump, where on both sides this caused increasingly steep gradients on

finer meshes in the elements where the conductivity is constant. Such a setting where the continuous potential clashed with the jumping conductivity would be very interesting to investigate using a discontinuous FEM approach.

Concluding, these results highlighted the local mesh dependence of the Local Subtraction approach[4]. Further, they showed that one can improve upon the recommendation of 2 vertex extensions from the original paper [33] depending on the used mesh. However, they also showed that 2 vertex extensions is still a valid recommendation due to the practical concerns with computation time and overall low relative errors.

[4]Lemma 2.4 in [33] shows that the weak solution obtained from the Local Subtraction approach is independent of all choices, assuming, however, continuous conductivity and an unrestricted Sobolev space.

5. Anisotropic EEG

This chapter focuses on investigating the effects of anisotropic conductivities at the dipolar source location for the EEG forward problem. Both the Local Subtraction and the Multipolar St. Venant approach are formulated generally enough for this investigation already[1]. Hence, the investigation focuses on quantifying the effect of anisotropy and its practical usability. First, the effects on sphere models are studied, extending and updating the work of Drechsler et al. [21], before investigating realistic head models.

5.1. Anisotropy Effect in a Four-Layer Sphere Model

In the case of spherical head models, we still have quasi-analytical solutions [16, 17] and therefore can meaningfully quantify the changes induced by anisotropy. To ensure the measured effects are actually due to anisotropy, we first restrict ourselves to the type of anisotropy that is of practical interest, namely the conductivity tensors described in Section 2.3. This means the main direction of conductivity and the relative restrictiveness of other directions are in fact assumed to be known from physiology. This allows pairing an isotropic conductivity with an anisotropic one that minimizes some difference measure, allowing us to attribute that difference to the anisotropy.

For later comparison against our reference work, we parametrize the model as in [21]. This means we use a four-compartment model consisting of brain, cerebrospinal fluid (CSF), skull and skin, see Table 3.1 for radii and isotropic conductivity. We will evaluate three different brain conductivity ratios typical for adults, children and premature babies, see Table 2.1. All parameters besides the brain conductivity will remain fixed throughout the evaluation[2].

Methods

To find the pairing of isotropic and anisotropic conductivities that minimizes their difference, the following procedure was devised. We distributed 500 electrodes E as described in Section 3.3. Next, we fixed a set of eccentricities, namely $80, 85, 90, 95$ and 99

[1] For the Local Subtraction approach, Malte Höltershinken recently extended and implemented analytic assembling of the right-hand side for this case [34].

[2] The implementation can be found under: `https://gitlab.dune-project.org/timon.gronotte/thesis-experiments/-/tree/main/01_tensor_tuner`

percent of the brain compartment radius. For each eccentricity in this set, we generated three sets of dipoles as described in Section 3.5, one radially oriented, one tangentially oriented and one with arbitrary orientation. Each dipole set consisted of 1000 individual dipoles, which were always of unit strength.

Using SimBio's implementation of De Munck's and Peters analytic formulas [17], we set up a function that gives the potentials at the electrodes for a dipole d in a sphere model S as in Table 3.1. The radial and tangential conductivity in the brain compartment can be specified as σ_r and σ_t respectively, yielding potential values: $u^{S,E}_{\sigma_r,\sigma_t}(d) \in \mathbb{R}^{|E|}$.

This means the potentials at the sensors for an isotropic conductivity $\sigma \in \mathbb{R}$ can be obtained by evaluating $u^{S,E}_{\sigma,\sigma}(d)$, to which we wanted to match the potentials $u^{S,E}_{c,c\cdot q}(d)$, where $q \in \mathbb{R}$ is an anisotropy ratio and $c \in \mathbb{R}$ a free parameter.

For each set of dipoles D, we then considered for each of the distance functions RE, RDM and lnMAG of the form $\text{dist} : \mathbb{R}^{|E|} \times \mathbb{R}^{|E|} \to \mathbb{R}$ the minimization problem:

$$\sigma_r = \underset{c\in\mathbb{R}_+}{\text{argmin}} \frac{1}{|D|} \sum_{d\in D} \left|\text{dist}\left(u^{S,E}_{\sigma,\sigma}(d), u^{S,E}_{c,c\cdot q^{-1}}(d)\right)\right| \tag{5.1}$$

Here, σ and q were the isotropic conductivity from Table 3.1 and the anisotropy ratio from Table 2.1 of an adult, child or premature infant. The optimal radial conductivity σ_r in a given setting was approximated using the Python interface of SimBio and SciPy's implementation of Brent's [11] algorithms[3]. Before calculating the optimal σ_r for all combinations of the above, we checked the convexity of the objective functions by plotting.

Results

An inspection of the plots of the objective functions for a range of possible σ_r revealed the following. First, RE and RDM, as functions of σ_r, exhibit a single minimum inside the considered intervals. The only exception to this was seen for radial sources in the infant model, where no minimum was found at the considered eccentricities of 0.8 and 0.85 for the RDM. This is possibly an effect of insufficient sampling. Similarly, the lnMAG appears to have a single root as a function of σ_r in the considered interval. This was taken as confirmation that the objective functions may be optimized using suitable Brent methods, except for deep radial sources against RDM. Further minimization results were confirmed by visual estimates from the produced plots. See the exemplary plots in Figure 5.1.

These plots allow further observations about the distribution of the difference measures over the set of simulated dipoles. In Figure 5.1, we can see that there is nearly no variation in the difference measures for only radial or only tangential sources. For arbitrarily oriented sources, we see that there still is a minimum, but the RDM has a variation

[3] In practice, SciPy's brentq was used to find the optimal value for lnMAG due to its superior performance.

of ±0.2. The reason for this probably lies in the different optimal σ_r for radial and tangential sources, therefore suggesting a strong dependence on source orientation.

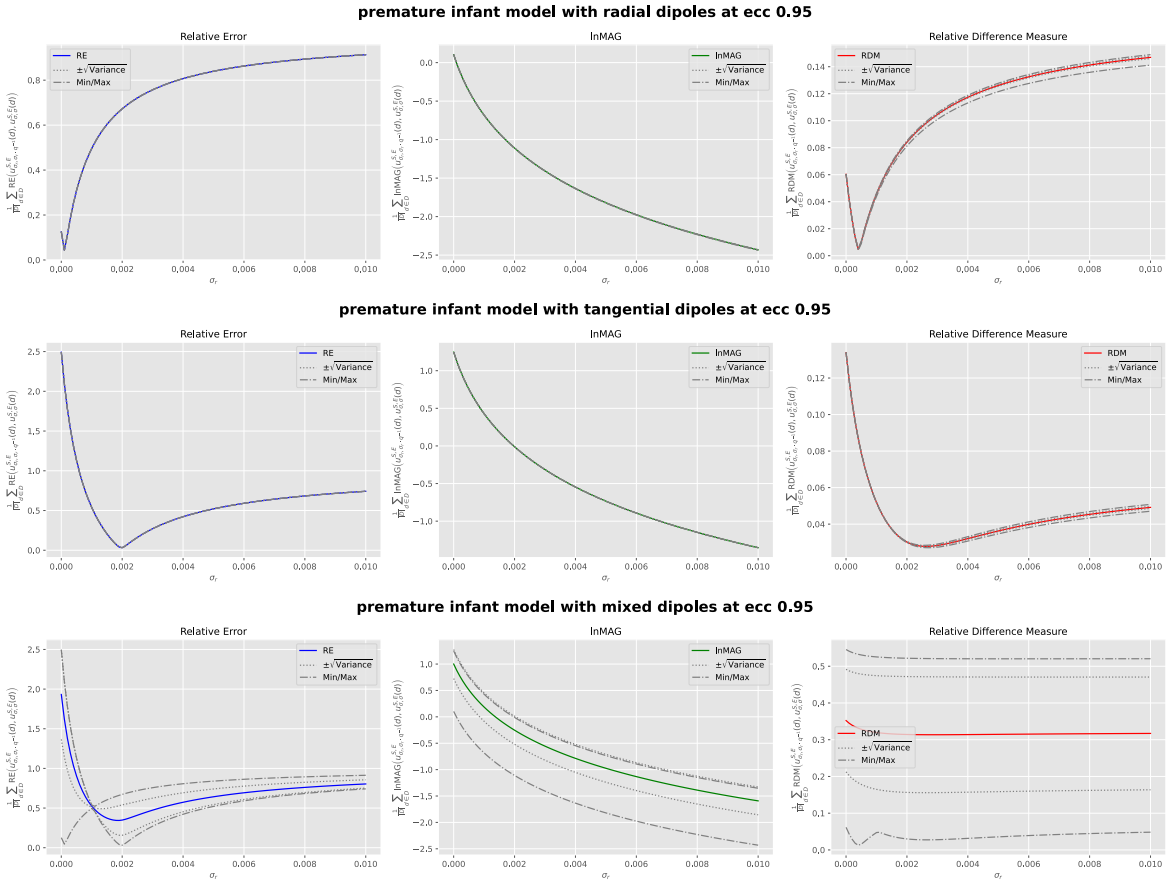

Figure 5.1.: Exemplary objective functions plot with σ the isotropic premature infant brain conductivity from Table 3.1 and q the corresponding anisotropy ratio from Table 2.1. D are the radial, tangential or mixed orientation dipole sets at an eccentricity of 0.95 and S and E represent the standard sphere model and electrode configuration.

Having by optimization obtained, where possible, optimal or otherwise good conductivity pairings, the optimal radial conductivity depending on source depth and difference measure is shown in Figure 5.2. The corresponding achieved RE and RDM between anisotropic and isotropic modeling are shown in Figure 5.3. The lnMAG is notably not shown here since it would always be effectively 0[4].

[4]Figures A.8 and A.9 in the appendix show similar results with more granular orientation dependence. These were not analyzed further due to practical irrelevance.

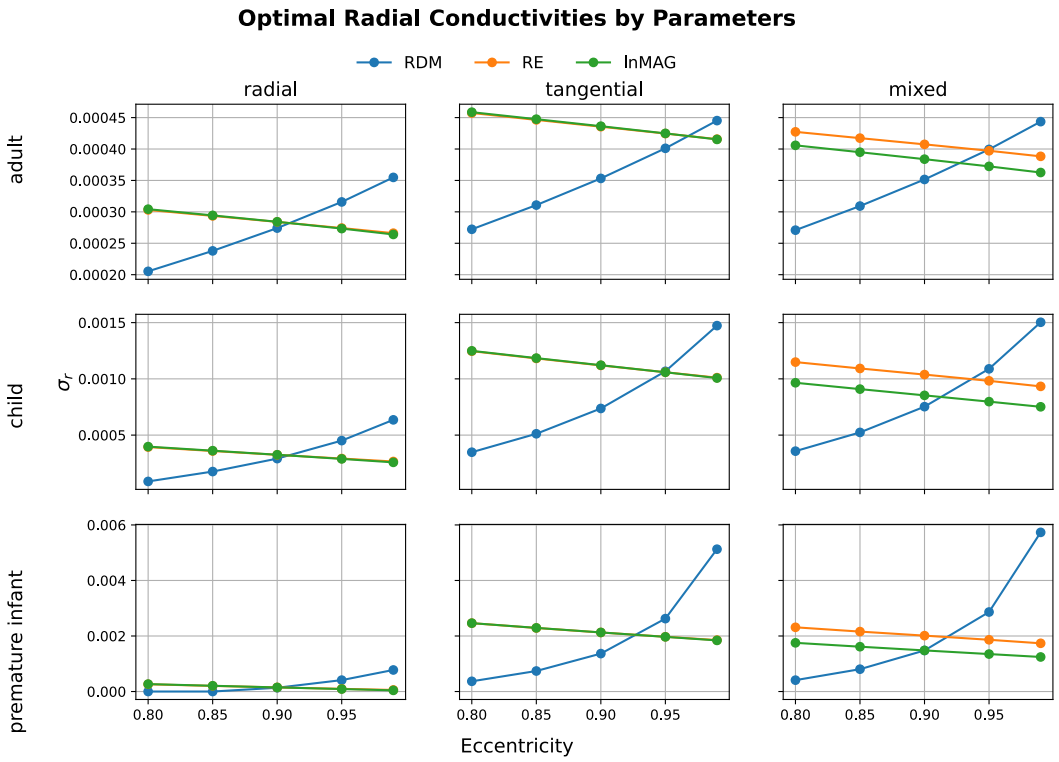

Figure 5.2.: Optimal radial conductivities, depending on source depth and difference measure, are shown for adult, child and premature infant conductivity sets and radial, tangential and mixed oriented dipoles. Where RE is not visible, it is exactly hidden behind the values associated with lnMAG.

Discussion

For most dipole sets, we were able to find optimal pairs of isotropic and fixed-ratio anisotropic conductivities. We saw that the optimal value depends on eccentricity, orientation and the observed difference measure.

Regarding the measures, the optimal conductivities of lnMAG and RE are closely linked, suggesting that the RE is mainly controlled by lnMAG. The RDM, however, appears independent and shows in optimization a trend towards higher conductivities for more eccentric sources, the opposite of the other measures. This forces a choice if one wants to optimize for magnitude or topographic errors. While minimizing the lnMAG and therefore RE would be very interesting, we choose to generally focus on the RDM due to the extreme conductivities resulting from lnMAG minimization. Regardless of the difference measure, we acknowledge that the found values escape physiological reason. This could possibly be due to our limitation to a four-layer sphere model not allowing us to distinguish gray and white matter.

Regarding source orientation, we were able to achieve quite low differences between

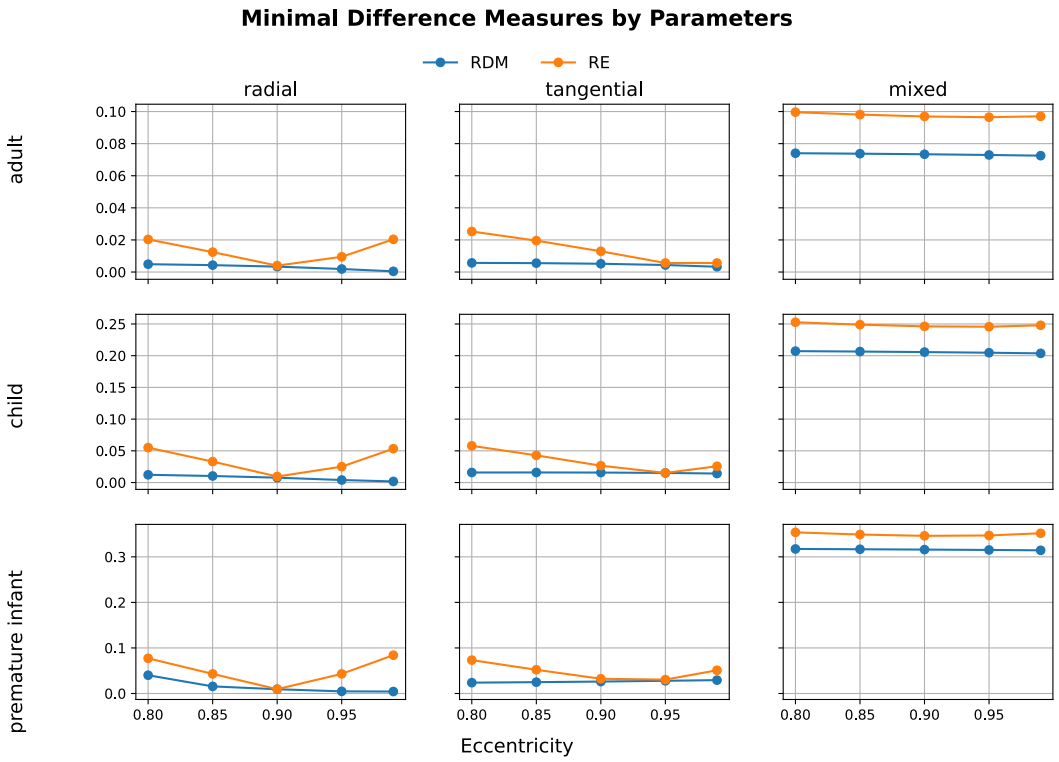

Figure 5.3.: RE and RDM between matched isotropic and anisotropic conductivities are shown, dependent on source depth and difference measure. Results cover adult, child, and premature infant conductivity sets and radial, tangential, and mixed-oriented dipoles. The lnMAG is omitted because its values are effectively 0 in this analysis.

isotropic and anisotropic pairing if the source orientation was fixed. Here, tangentially oriented sources lead to an anisotropic RE optimum that is nearly double the conductivity required for radial sources across all investigated ratios. This provides a possible reason for the failure to properly minimize difference measures for sources of mixed orientation. Regardless, we were able to reproduce the optimization findings from [21] with the mixed orientation dipoles, showing that we can significantly better approximate anisotropic results isotropically if the source orientation is known. Due to this, we will enact the normal constraint in all further investigations. This means only considering sources pointing in the radial direction (see definition 15), which is physiologically motivated and is practically assumed in our tensor placement.

Lastly we found the source depth to be of relatively minor significance compared to the difference measure and orientation. It is notable, however, that the lowest achieved relative error for radial and tangential dipoles occurs at an eccentricity of around 0.95, where the optimal conductivities of lnMAG and RDM lie very close together.

Overall this means that one can achieve small differences with a pure isotropic model if the source depth, orientation and a difference measure are known. If one needs to fix a single pairing of isotropic and anisotropic conductivities without knowing these for certain, as in source reconstruction, the differences will be significantly greater.

To achieve the best approximations of anisotropy for at least some sources, we fixed the ideal conductivity at a realistic eccentricity of 0.95 for radial sources and focused, as aforementioned, on the RDM. The exact values can be found in Table 5.1. It should be stressed again that the values are not realistic, questioning the validity of the four-layer sphere model in investigating gray matter anisotropy. They will only be used to validate the numerical approaches in an anisotropic setting.

Table 5.1.: Anisotropic conductivities, best matching isotropic conductivities for radially oriented dipoles from Table 3.1. Max RE gives the maximal relative error seen across 8000 radial dipoles with an eccentricity between 0.8 and 0.99. Max RDM gives the maximal relative difference measure across the same setup.

Model	Rad con.	Tan. con.	Max RE	Max RDM
Adult	0.27416 $\frac{S}{m}$	0.19444 $\frac{S}{m}$	0.0425	0.01822
Child	0.29106 $\frac{S}{m}$	0.1078 $\frac{S}{m}$	0.10463	0.04827
Premature baby	0.13561 $\frac{S}{m}$	0.02712 $\frac{S}{m}$	0.13145	0.06999

5.2. Numeric Errors in a Four-Layer Sphere Model

As we have established, in a four-layer sphere model, one can approximate the anisotropic conductivity when the source orientation and depth are known to a reasonable degree. In the following, we want to contrast this with numeric simulations. As a consequence of the previous Section 5.1, we only consider radially oriented sources.

Methods

To numerically evaluate the effect of an anisotropic brain compartment, the same tests were set up for all three spherical head model meshes, `rough_mesh`, `mid_mesh` and `fine_mesh` from Section 3.2, with 500 electrodes distributed as outlined in Section 3.3. The test consisted of setting up 1000 radially oriented dipoles per eccentricity from Table 3.3, placed as described in Section 3.5 and computing[5] the differences against the analytic potentials at the electrodes in RE, RDM and lnMAG.

[5]The implementation can be found at: `https://gitlab.dune-project.org/timon.gronotte/thesis-experiments/-/tree/main/03_loc_sub_VS_st_venan`

To do so, these meshes were imbued with the isotropic conductivity from Table 3.1. As reference tests, the calculations were first run with the isotropic brain conductivities from said table. Thereafter, the computations were run with the anisotropic brain compartment conductivities as computed in the previous Section 5.1, see Table 5.1. Those calculations were carried out to see if better results than isotropic approximations could be reached. Due to the physiologically unrealistic conductivity values of the optimization, tests were further conducted with the radial conductivities set to the isotropic values from Table 3.1. The tangential values for those were obtained by applying the anisotropy ratios from Table 2.1. This last parameterization was thought to provide further insight into the performance of the different source models with realistic conductivities. All the conductivities were set as tensors using the process described in Section 3.4.

Results

The relative error results can be found in Figure 5.4 for the isotropic test, along with the results for the optimized conductivities, while Figure 5.5 has the results for the physiologically realistic conductivity assumptions. RDM and lnMAG figures can be found in the appendix. The results from the isotropic case are in Figure A.10, from the optimized anisotropic conductivities in Figure A.11 and from the physiologically realistic anisotropic conductivities in Figure A.12.

The RE results from the fully isotropic calculations show the expected behavior and error ranges for this fairly standard test [33, 41, 67]. The error starts low with very few outliers for deep sources before the error and error range grow with eccentricity. Furthermore, we observe at all eccentricities a roughly second-order error reduction when halving the average element side length, as expected.

We see in all targets and meshes, besides the adult target on `rough_mesh`, that the Local Subtraction approach produces lower errors than the St. Venant approach. It is to note here that this result is due to us using 6 vertex extensions on `fine_mesh` because of the results from Section 4.2. If the recommended two vertex extensions are used, we saw no more error reduction for sources at higher eccentricities than 0.97 when moving from `mesh_mid` to `mesh_fine`.

In this isotropic case, these findings carry over to the RDM and lnMAG plots in Figure A.10, with both measures being consistently small.

Next, we consider the anisotropic test with the optimized conductivity values. In Figure 5.4, the results of the analytic isotropic approximation are shown along with the numeric results. Concerning the RE for realistically eccentric sources, these lie consistently between the medians of the numeric approaches on `rough_mesh` for sources outside of 98% of the brain radius. For the deepest sources, the isotropic analytic solutions produce notably bigger errors. Note here that the drop in approximation goodness is in part due to us fixing a single pairing of isotropic and anisotropic conductivities across all

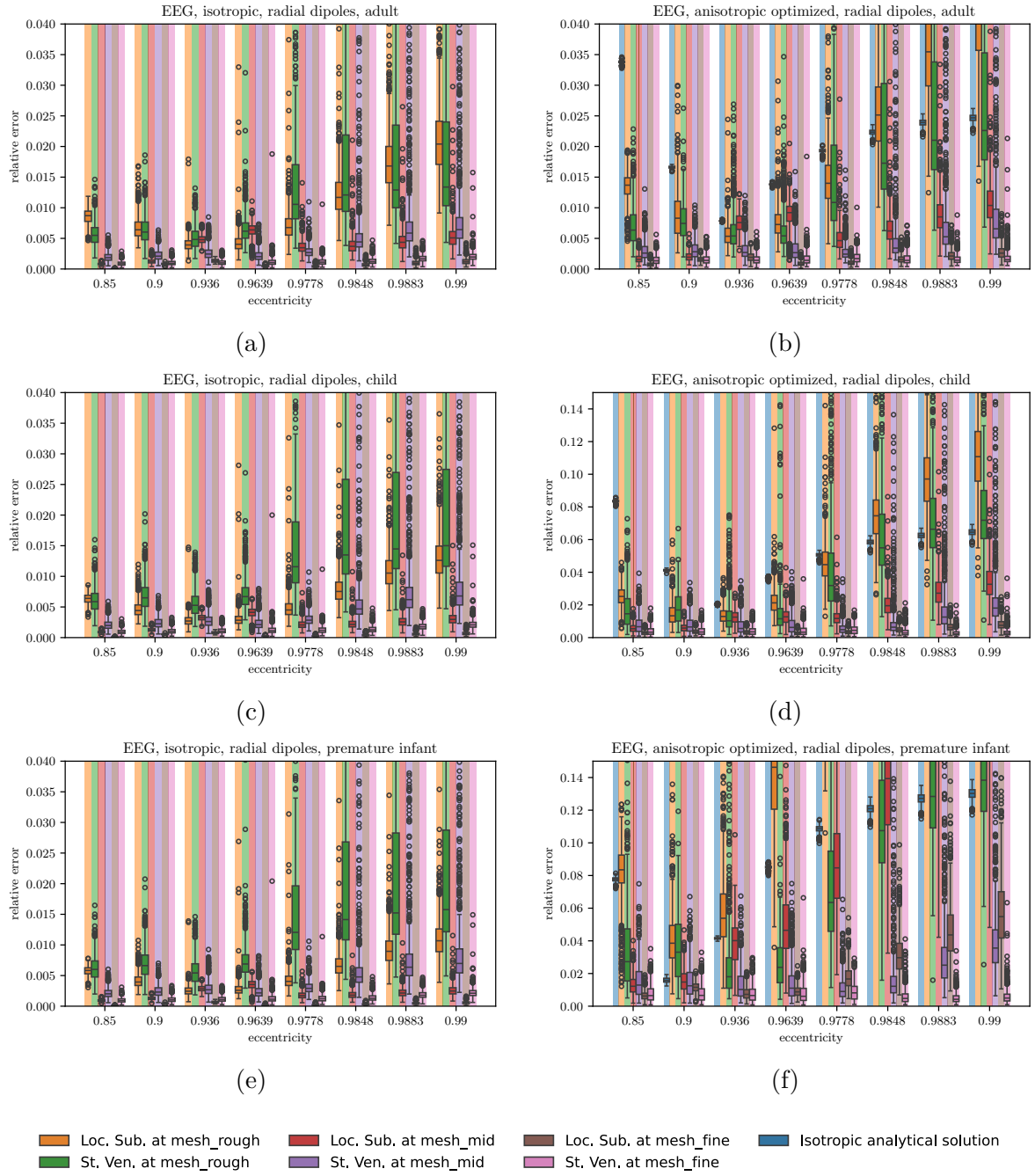

Figure 5.4.: Relative error comparison of Local Subtraction and Multipolar St. Venant approaches on multiple grids for radial dipoles plotted against eccentricity. Subfigures (a),(c),(e) show results for isotropic conductivities from Table 3.1, of adult, child and premature infant respectively. Subfigures (b),(d),(f) show the results for the error optimized conductivities from Section 5.1, of adult, child and premature infant respectively. The later also include a comparison against isotropic analytic approximation.

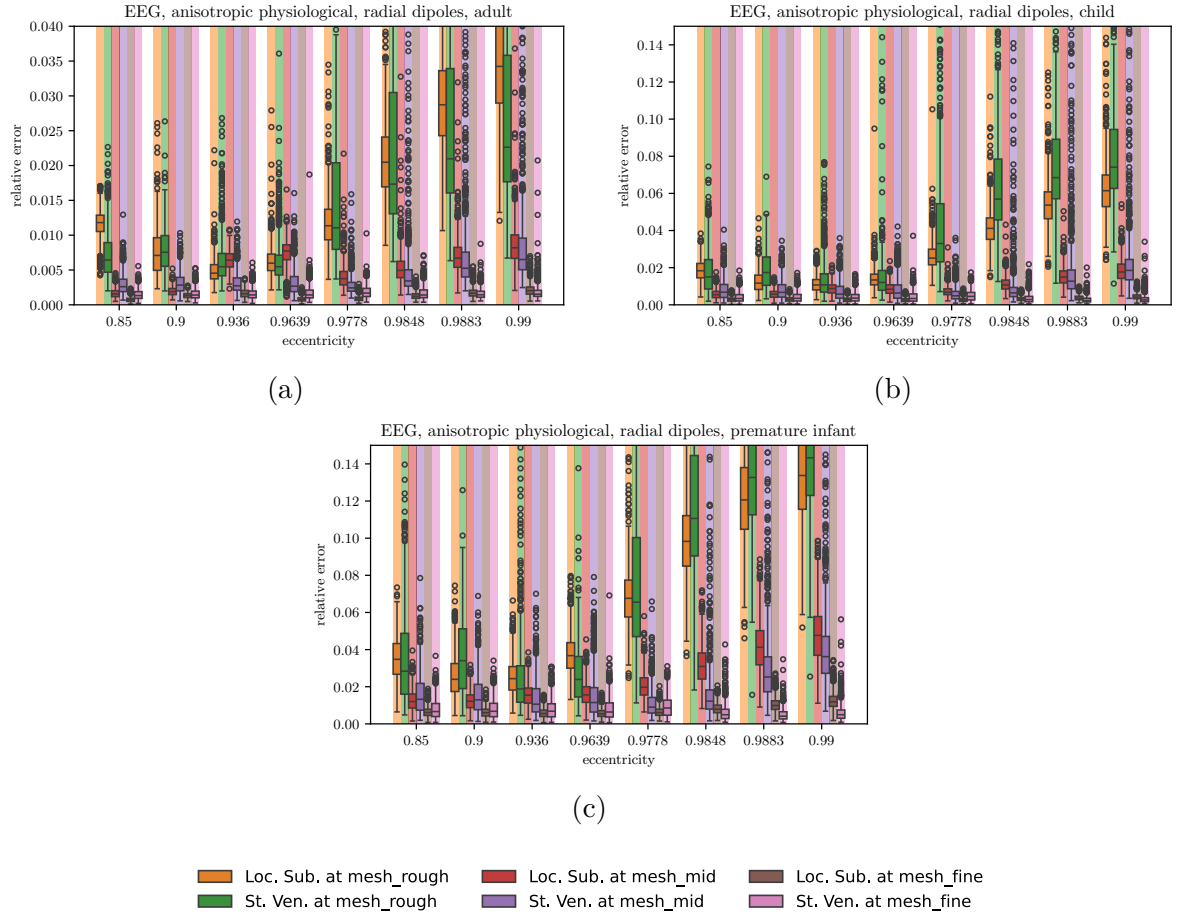

Figure 5.5.: Relative error comparison of Local Subtraction and Multipolar St. Venant approaches on multiple grids for radial dipoles plotted against eccentricity. Subfigures (a),(b),(c) show results for physiologically motivated anisotropic conductivities, of adult, child and premature infant respectively. Due to the very high errors, the isotropic analytic approximation has been omitted from these plots.

eccentricities.

Focusing on the numeric solutions, those still show a similar convergence order, but the average error and error spread are much bigger as compared to the isotropic case. Different is also that the Local Subtraction approach produces consistently bigger errors than the St. Venant type approach on the same grid.

For the adult target, the errors show nearly no visible difference to the isotropic case. The child target sees errors about 4 times as high as on an isotropic mesh and the premature infant target sees an around 8 times increase.

Looking at the RDM and lnMAG in Figure A.11, we see that the RDM is nearly indistinguishable from the RE, while the lnMAG remains fairly small for `mesh_mid` and `mesh_fine`.

The findings from the physiologically motivated conductivities in Figure 5.5 demonstrate a substantial decrease in error for the Local Subtraction approach in comparison to the optimized conductivity values. At the same time, the Multipolar St. Venant results look nearly identical for both anisotropic conductivities. The same can be seen for RDM and lnMAG in Figure A.12. Nevertheless, these errors remain far greater than those observed for the isotropic reference.

Discussion

In the reference test with isotropic conductivities, both approaches demonstrated excellent performance and convergence speeds that were in line with expectations. Here, the Local Subtraction approach is nearly always slightly ahead. However, the Local Subtraction approach showed a correlation between relative error and brain compartment conductivity. That correlation would suggest that the relative error can be decreased by increasing the brain compartment conductivity. If that were true, the assumed adult conductivity is near the boundary to when the Multipolar St. Venant approach becomes a better choice. We also found that the remaining relative error in the isotropic case appears to be closely bound to the RDM.

A key initial finding from the tests with anisotropic conductivities is that the relative errors achieved for premature infants and children were a magnitude higher for both approaches than in the isotropic case. The overall higher errors might be explained by the conductivity being different in each source element, breaking the continuity of the conductivity near the source quite severely. This would limit the area in which the Local Subtraction approach can rely on the analytic solution to solely the initialization element, requiring numeric correction in areas where u^{∞} still changes rapidly. Similarly, the Multipolar St. Venant approach assumes a homogeneous source space, which could explain the bigger errors. This would also be in line with the smaller errors for the adult tests, where the necessary corrections would be comparatively small.

The Local Subtraction approach performed in general not quite as well as the Multi-

polar St. Venant approach when tested with these conductivities. Clearly, the extreme conductivity values resulting from the minimization in the previous Section 5.1 overwhelm the Local Subtraction approach far more than the St. Venant type approach. Nevertheless, these results still indicate that it should be possible to approximate anisotropic conductivities with an isotropic one for radial dipoles in a four-layer sphere model. This approximation is, at best, equivalent to a proper anisotropic numeric model with a poor average element side length of 4mm. This means practical applications would yield better results from proper numerical simulations compared to an isotropic approximation. This confirms the finding of our reference publication [21], even with more prior knowledge included in the approximation.

Considering physiologically motivated conductivities, we further evaluated the performance of the approaches. Here, the two approaches become somewhat competitive, a clear improvement for the subtraction approaches from their previous showing in the reference publication [21]. Especially on `mesh_rough`, the Local Subtraction approach manages to outperform St. Venant for relatively shallow sources across all tested anisotropy ratios. While the Local Subtraction approach is competitive with the Multipolar St. Venant method for child-level anisotropy on the more practical `mesh_mid` and `mesh_fine` for relatively shallow sources, the St. Venant approach slightly pulls ahead for premature infant anisotropies. Interestingly, this somewhat reverses for sources deeper than $3mm$ in the brain compartment on the finest mesh. Looking at the RDM and lnMAG reveals that the Local Subtraction approach often produces the larger RDM, which it compensates for with a nearly always better lnMAG.

Hence, modeling an anisotropic source compartment does not perform as well as modeling an isotropic one. If, however, the anisotropic conductivity is known with certainty, properly modeling the anisotropy is superior to any isotropic approximation. Furthermore, no single approach substantially pulled ahead when modeling realistic conductivity values. Therefore, one might recommend using both approaches and cross-referencing the results. Lastly, it should be reiterated from the previous Section 5.1 that the four-layer sphere model seems unfit for investigating gray matter anisotropy and these results should be primarily taken as a performance evaluation.

5.2.1. Local Mesh-Dependent Performance of Multipolar St. Venant and Local Subtraction Approach

The results from the previous Section 5.2 show the Multipolar St. Venant approach beating the Local Subtraction approach in some anisotropic settings. If we were to use `mesh_init` from the original Local Subtraction paper [33], however, we would see the best performance from a Local Subtraction approach. In the meshing Section 3.2, the varying performance depending on the chosen mesh was mentioned and in this test, we seek to investigate the effects of differently resolved brain and CSF compartments in an

anisotropic gray matter setting.

Methods

To investigate the local mesh dependence of the Local Subtraction and Multipolar St. Venant approach, we chose the standard anisotropic sphere model for premature infants. The exact values can be found in Tables 3.1 and 2.1, while we assumed the radial conductivity in the gray matter to be equal to the isotropic value. We created multiple meshes of this model based on `mesh_mid` from Section 3.2, meaning the skull and skin compartments were set to be meshed with a $2mm$ average element side length. The average element side lengths of the brain and CSF compartments were independently varied between 4 and $2mm$ and 4 and $1mm$, respectively, with $0.222mm$ steps. For all meshes, we then created electrodes and dipoles as described in Sections 3.3 and 3.5, respectively. We then calculated the potential at the electrodes with Local Subtraction and Multipolar St. Venant, as well as analytically, to compute RDM, RE and lnMAG. We then computed[6] the median error per approach and eccentricity to compare which approach performed best on which mesh at a given eccentricity.

Results

Figure 5.6 shows the difference in median RE of Local Subtraction and Multipolar St. Venant at differently resolved sphere model meshes for radial dipoles at an eccentricity of 0.99.

First, we note that the average element side lengths do not actually lie on an equally spaced grid, nor did we achieve a sampling fully in the desired region. The first issue is mostly due to geometric constraints. The CSF compartment is only $4mm$ wide and depending on the meshing of the enclosing surfaces, making the desired edge lengths unfeasible. Furthermore, GMSH has internal stopping conditions that may result in early stopping, which is in part the reason for the second issue.

At the achieved average element side length, we see the median RE of the Local Subtraction approach minus the median RE of the Multipolar St. Venant approach, indicated by the marker color. Additionally, the data point is marked by a cross if the Local Subtraction achieved smaller errors and by a circle otherwise.

We see two clusters. The St. Venant approach produced the smaller median mostly in the region where CSF and gray matter had near-equal element side lengths. The Local Subtraction produced the better medians when the CSF resolution was high and the gray matter compartment was not highly resolved.

[6] The implementation can be found at: `https://gitlab.dune-project.org/timon.gronotte/thesis-experiments/-/tree/main/10_init_performance_check?ref_type=heads`

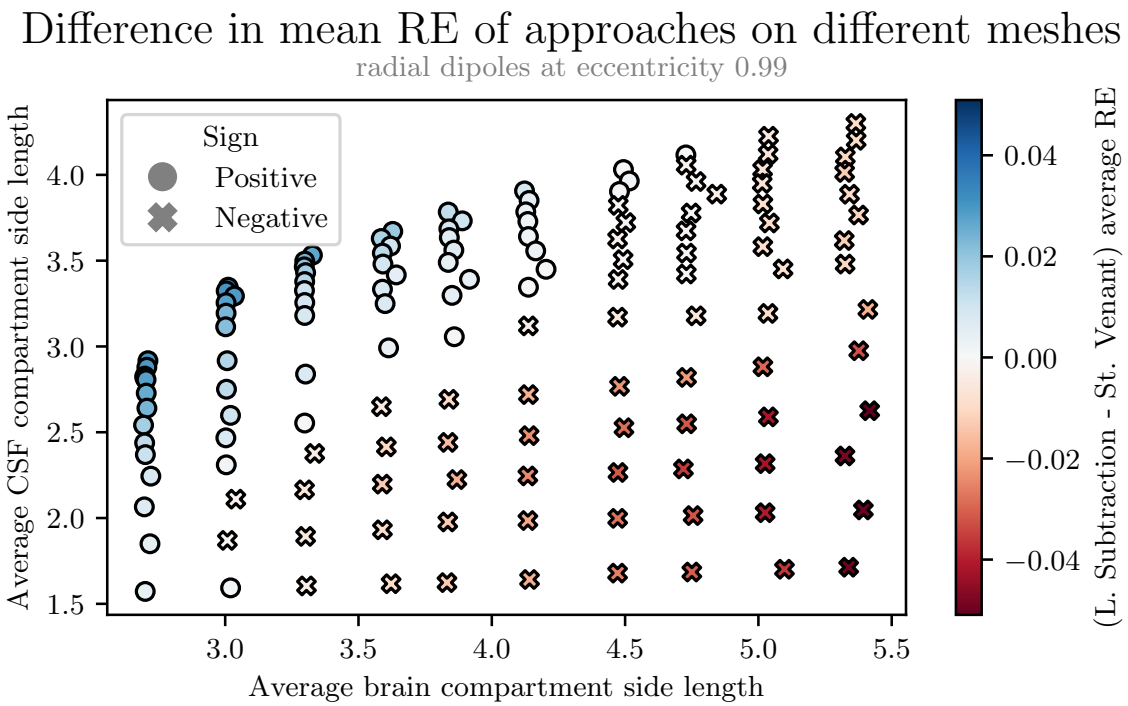

Figure 5.6.: Plot showing the difference in median RDM of Local Subtraction and Multipolar St. Venant at differently resolved sphere model meshes. The simulated dipoles were radial at an eccentricity of 0.99 in an anisotropic brain compartment. Data marked with a cross indicate a better median for the Local Subtraction approach.

Figure 5.7 additionally shows the achieved relative errors for the highest and lowest tested CSF and brain compartment average element side lengths.

Both approaches achieve the lowest errors at the finest mesh and we see an increase in the errors, especially for the highly eccentric sources, when we reduce either compartment resolution. Consequently, the largest errors were produced on the roughest mesh.

Discussion

These results demonstrate that selecting the optimal approach for anisotropic cases is highly mesh-dependent, precluding a universal recommendation.

For the presented highly eccentric configuration, clear trends are observed when changing the mesh resolution. Increasing the resolution in the brain compartment appears to lead to better results for the St. Venant approach relative to the Local Subtraction approach. Conversely, increasing the resolution in the CSF compartment appears to lead to better results for the Local Subtraction approach relative to the St. Venant approach. This befits the comments made in Section 3.2 quite well. The local

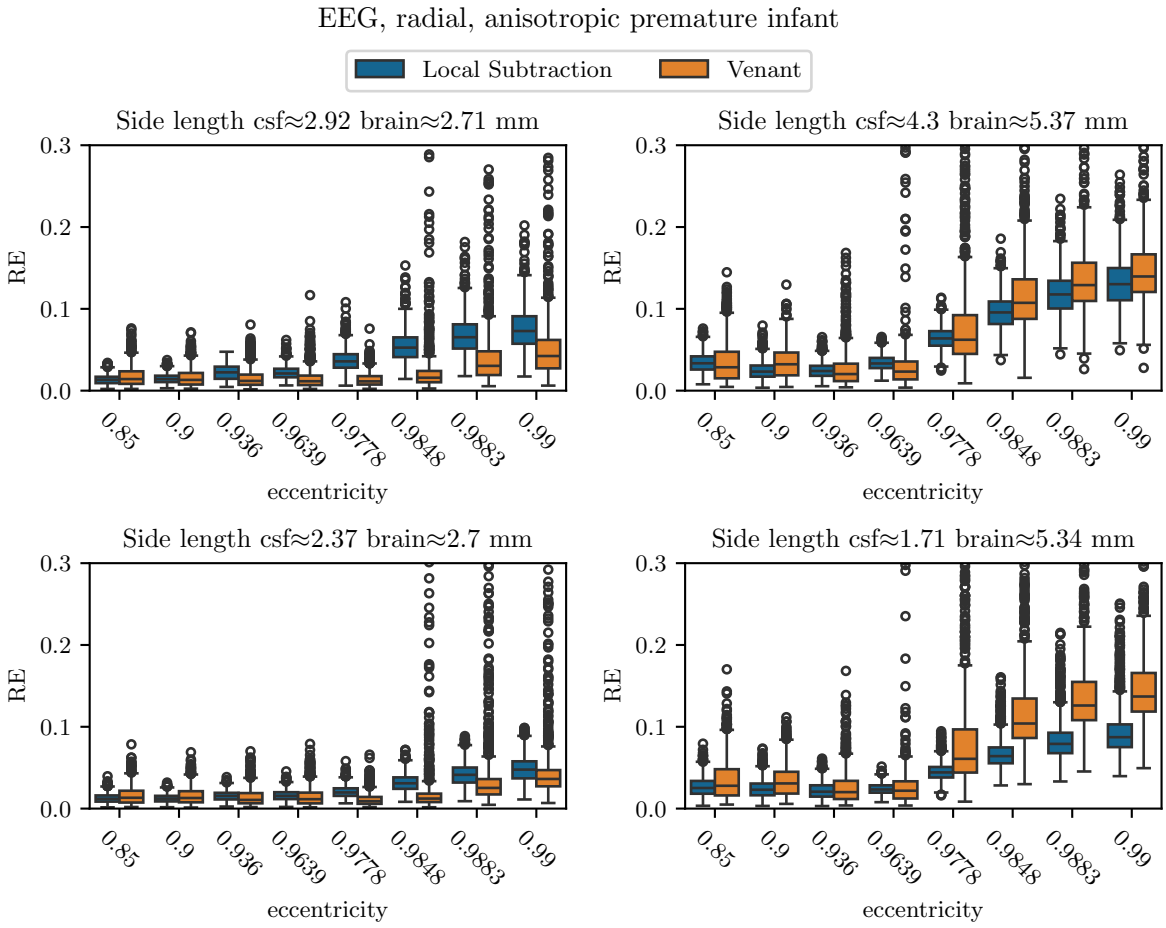

Figure 5.7.: Plots showing the relative error for the Local Subtraction and Multipolar St. Venant approach achieved in a four-layer sphere model of an anisotropic premature infant at differently resolved brain and CSF compartments.

subtraction approach still profits from high resolution at conductivity jumps, but only more then direct approaches, if they are in patch or transition region.

It is important to note, however, that the choice of the best approach is generally much more nuanced and the required extensive parameter sweeps across multiple variables exceed the scope of this investigation. Factors such as dipole orientation and source depth, which are not presented above, have shown a profound impact on the results in preliminary testing. Additional approach parameters, compartment sizes and geometry have not been investigated but should be considered in a more in-depth investigation.

From a practical standpoint, this suggests that both approaches are reasonable choices for anisotropy in the source space. Furthermore, one should aim to have similar brain and CSF compartment resolutions to ensure both approaches yield the best possible result. Since it is not currently possible to definitively state which approach is best for a

given mesh, running the forward computation with both provides a way to validate the simulation results and can give a hint towards insufficient mesh resolution.

5.3. Numeric Anisotropy Effect in a Realistic Head Model

To investigate the effect of conductivity anisotropy in the source space without conductivity measurement errors, we want to find for a given isotropic conductivity, anisotropy ratio, eigenvector directions and error measure the conductivity tensor that minimizes the error between isotropic and anisotropic simulations. In the previous Section 5.1, we investigated this in a four-layer sphere model, where we had quasi-analytic solutions available. There, we found that we could isotropically approximate the solution to a degree such that the error was about four times as high as anisotropic numeric models on a realistic grid. Nevertheless, we were obliged to determine that the conductivity pairings eluded physiological reasoning. It was assumed this result was in part due to a missing distinction between white and gray matter. Additionally, a spherical head model exhibits more symmetries than an actual brain. Hence, we want to repeat this investigation here using the previously investigated numerical models, knowing we will introduce a numerical error.

Methods

The devised procedure was based on the realistic head model introduced in the meshing Section 3.2, along with the electrodes E introduced in Section 3.3. Furthermore, we chose to use the dipoles D as described in Section 3.5 and assigned anisotropic conductivity tensors of a given anisotropy ratio q to the gray matter compartment, as described in Section 3.4, as well as isotropic tensors of a given conductivity σ to compare against, yielding a realistic head model S.

We constructed an objective function to measure the difference between the isotropic and anisotropic models, analogous to the optimization problem (5.1) from Section 5.1. The function takes as input the radial conductivity of the anisotropic tensors σ_r. After scaling the anisotropic tensors in the model, we calculated forward simulations for all dipoles using the Local Subtraction approach for both the isotropic $\tilde{u}^{S,E}_{\sigma_r,\sigma_r\cdot q^{-1}} \in \mathbb{R}^{|E|}$ and anisotropic $\tilde{u}^{S,E}_{\sigma,\sigma} \in \mathbb{R}^{|E|}$ models. This yielded potential values at our defined electrodes. From these potentials, we calculated the RDM between the isotropically and anisotropically computed potentials using the Local Subtraction approach. The objective functions final output is the mean RDM across all simulated dipoles.

$$\sigma_r = \underset{c\in\mathbb{R}_+}{\operatorname{argmin}} \frac{1}{|D|} \sum_{d\in D} \operatorname{RDM}\left(\tilde{u}^{S,E}_{\sigma,\sigma}(d), \tilde{u}^{S,E}_{c,c\cdot q^{-1}}(d)\right) \tag{5.2}$$

Note that the use of only radial dipoles and the use of the RDM were consequences of our sphere model testing. In Section 5.1, it was argued that only radial sources are physiologically reasonable and found that RE and lnMAG optimization favored conductivities where the numeric approaches get unstable.

As previously, the minimization was parameterized with the isotropic conductivities from Table 3.1 and the anisotropy ratio from Table 2.1 for premature infants, children and adults. SciPy's implementation of Brent's algorithm [11] was used to find the optimal radial conductivity for each age group[7]. Furthermore, all calculated RDMs were stored for later inspection and plotting.

Results

The output from the optimization can be found in Table 5.2, while a plot of the objective function can be found in Figure 5.8.

Table 5.2.: Radial conductivity σ_r minimizing RDM to isotropic conductivities at given ratios in our simulations. Values were obtained in realistic head model besides Anisotropic Sphere Validation, which was obtained from a four-layer sphere model.

Model	σ_{Iso}	$\sigma_r : \sigma_t$	Optimal σ_r	RDM
Adult	0.33	1.41:1	0.339	0.059
Child	0.51	2.7:1	0.476	0.18
Premature baby	0.59	5:1	0.408	0.287
Anisotropic Sphere Validation	0.51	2.7:1	0.54	0.024

All of the plots exhibit the same qualitative curve that was also observed in the previous sphere model study in Section 5.1. They show a single clear minimum with a quickly rising flank for smaller conductivities and a slowly rising flank for larger values.

The validation experiment, a four-layer sphere model passed through the same pipeline as the realistic head models, showed good results. The standard deviation of the means is small, especially in the minimum, with at most moderate outliers.

The adult model, with the lowest anisotropy ratio, showed the next best results. The standard deviation in the minimum is 0.05, which is over three times larger than in the validation experiment. But it does contain, in all tested radial conductivities, outliers that go far beyond the plotted range. For the child and premature infant models, we see similar overall trends but with a further increasing standard deviation of the computed RDMs.

[7]The implementation can be found at: https://gitlab.dune-project.org/timon.gronotte/thesis-experiments/-/tree/main/06_optimizing_conductivity_realistic_head

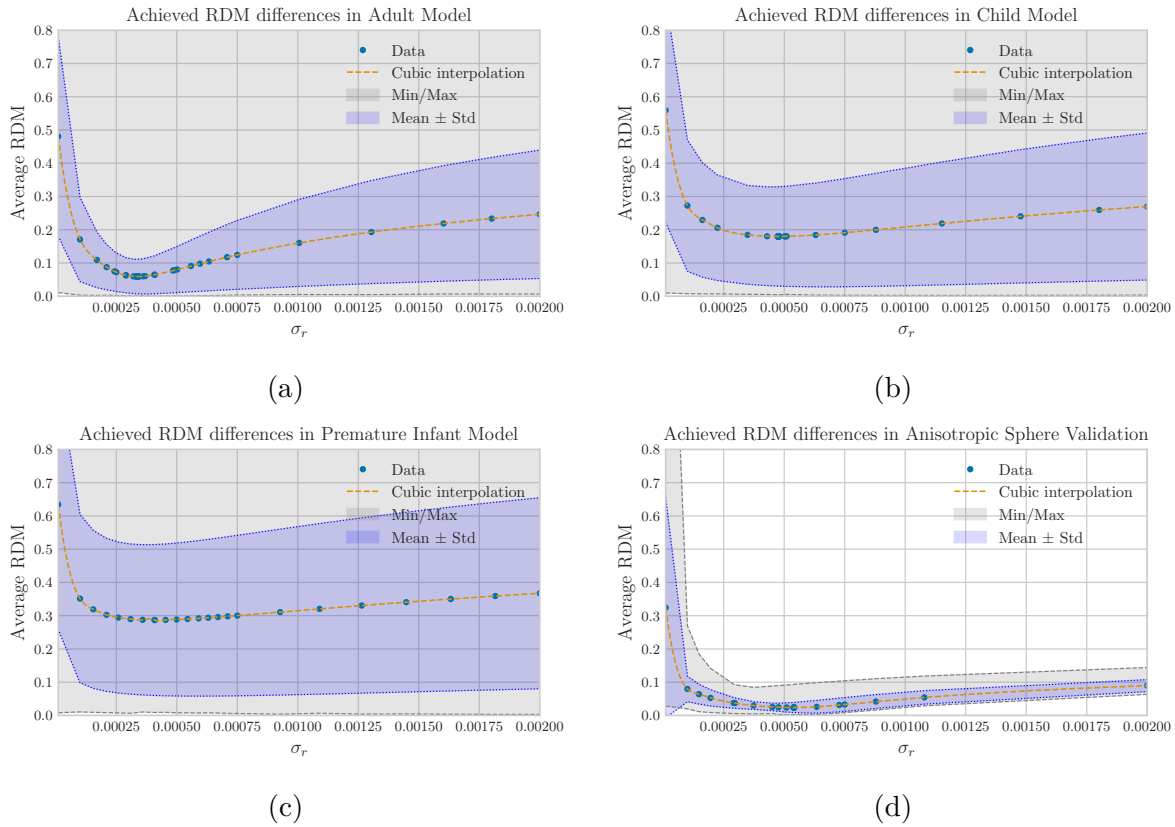

Figure 5.8.: Plots showing the average RDM between isotropic and anisotropic realistic head models, at different isotropic conductivities and anisotropy ratios. Subfigure (a) uses the values for a adults, (b) for a child and (c) for premature infant. Subfigure (d) shows the validation results for a four-layer sphere model with child values, that has undergone the same pipeline as the realistic head model.

Comparing the models quantitatively, the final RDM values in Table 5.2 increase with the anisotropy ratio, indicating that the effect of the anisotropy increases with the ratio. Note here that by construction, all models used the same volume conductor with conductivity tensors that shared their eigenvectors, differing only in their eigenvalues.

Discussion

The observed trends align with the necessary preconditions for our algorithmic optimizer, indicating that the model's assumptions are valid and lending support to the reliability of the optimization results.

The comparison between the child model Figure 5.8(b) and the four-layer sphere validation Figure 5.8(d), which share isotropic conductivity and anisotropy ratio, suggests a significant effect of a more complex geometry. These effects could, however, be

exaggerated by, first, the exact orientation of tensors and the bigger conductivity jumps between elements inherent to the more complex geometry. Our method of tensor creation passed a visual test but is not otherwise validated, leaving potential room for errors and improvement. Regarding the conductivity jumps, we previously saw in Figure 5.5 that numerical errors increased with an increase in anisotropy. Considering this effect was observed in a sphere model with gracefully changing anisotropy tensors, a bigger effect is to be expected in more complex realistic models.

All models use the same volume conductor with conductivity tensors that share their eigenvectors and only differ in their eigenvalues, meaning that the observed effect cannot be due to tensor placement or geometry.

Although the optimization yielded specific values for further testing, see Table 5.2, the wide spread of the data must be acknowledged. This spread is a predictable consequence of the globally more complex volume conductor geometry as well as the vastly different local geometries at the source locations. The results are therefore biased by the set of chosen source locations. This finding underscores a key limitation of the optimization approach. While statistics will always produce a best-fit value, the washed-out peak suggests that no single, truly optimal solution exists. Ultimately, the data distribution is a crucial finding in itself, demonstrating that the effect of anisotropy on the solution is highly dependent on the source location and resists a simple uniform approximation.

Our test so far aligns with the assumption that the effect of anisotropy should increase with more complex geometry and did provide conductivity pairings minimizing RDMs between isotropic and anisotropic simulations. However, a lot of uncertainties were discussed, including large variations of RDMs, such that the results need to be interpreted and used carefully. Note that the following section will further question the validity of the results.

5.4. Comparative Assessment of Numerical Solutions in a Realistic Head Model

Moving from sphere models to realistic head models sharply increases the model complexity and removes sphere model symmetries. In the previous Section 5.3, it was observed that this made isotropic approximation near impossible, but the spread of errors also questions if the numeric approaches are still valid on realistic head models. This will be investigated by comparing the simulation results of the Local Subtraction and Multipolar St. Venant approaches on a realistic head model and its regular refinement.

Methods

To carry out the simulations, the realistic head model as described in Section 3.2 and a regular refinement of this tetrahedral mesh were used. A source space that was used on both meshes was created on the standard realistic head model as described in Section 3.5. The mesh was then assigned isotropic and anisotropic conductivities corresponding to the adult, child and premature infant models by the process outlined in Section 3.4. Using the electrode set described in Section 3.3, forward simulations for all described variants were then carried out with the Multipolar St. Venant and Local Subtraction approaches.

The method for creating anisotropic tensors in realistic head models is in need of validation in its own right. To mitigate potential errors, the analysis was restricted to dipoles lying within a small cuboid region, shown in Figure 5.9. This cuboid lies in the left parietal lobe and was chosen visually to have only well-oriented dipoles in a relatively thin gray matter compartment[8].

For each dipole in this cuboid, empirical cumulative distribution functions (ECDFs) were computed[9] showing the RE, RDM and lnMAG between:

1. The results of the two approaches on the same meshes. For the lnMAG, the magnitude of the Local Subtraction approach will be divided by the magnitude of the Multipolar St. Venant approach.

2. The results of an approach on the original mesh and its refinement. For the lnMAG, the magnitude of the standard mesh will be divided by the magnitude on the refined mesh.

3. The isotropic and anisotropic forward simulations, using the same mesh and numerical approach. For the lnMAG and RE, the isotropic results will be relative to the anisotropic ones.

Cumulative distribution functions were used here as they nicely show what fraction of the results lies above or below a threshold. They hide outliers to some extent, which was willingly accepted to better focus on larger trends.

Results

To establish a baseline for subsequent comparisons, we first examine the results derived from the isotropically parameterized head model.

[8] It was confirmed that this indeed improved the obtained results.

[9] The implementation can be found at: `https://gitlab.dune-project.org/timon.gronotte/thesis-experiments/-/tree/main/09_realistic_head_comparisons`

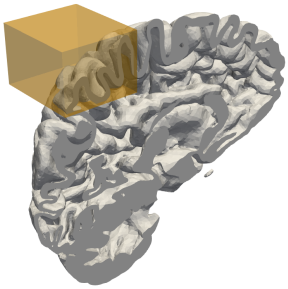

Figure 5.9.: Brain region used to restrict the analysis in Section 5.4. Only source locations within this highlighted region are included in the error comparisons.

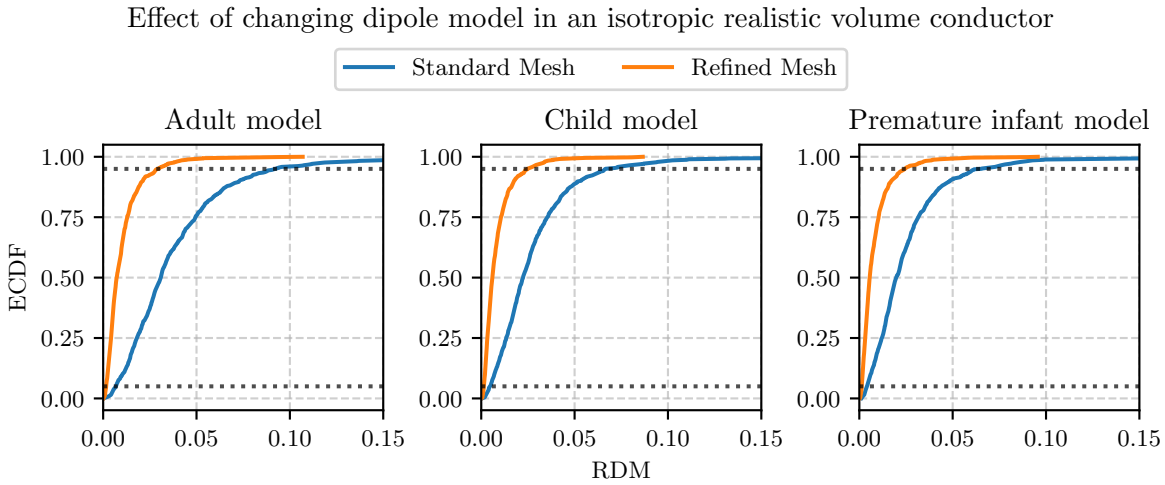

Figure 5.10.: ECDFs of RDM for isotropic forward calculations across different numerical approaches in the realistic head model. Curves compare Local Subtraction and St. Venant approaches on standard and refined meshes for adult, child and premature infant models.

Considering the differences between the numeric approaches on the same original mesh in Figure 5.10 shows that 95% of the produced differences result in an RDM smaller than 0.1 across all conductivities. On the finer mesh, 95% of the produced differences result in an RDM smaller than 0.025 across all conductivities. Regarding the lnMAG, all results show a tendency of the Local Subtraction approach to produce the greater magnitude. On the realistic mesh, 95% of the values showed a lnMAG magnitude below 0.15, while on the finer grid, this was below 0.025. It is noteworthy that the adult model values are slightly worse for lnMAG as well as RDM using the realistic mesh resolution, while the other curves show not much variance.

To assess the impact of grid resolution, ECDF plots for the RDM and lnMAG differences for a given numeric approach are shown in Figures A.13 and A.14. The RDM values

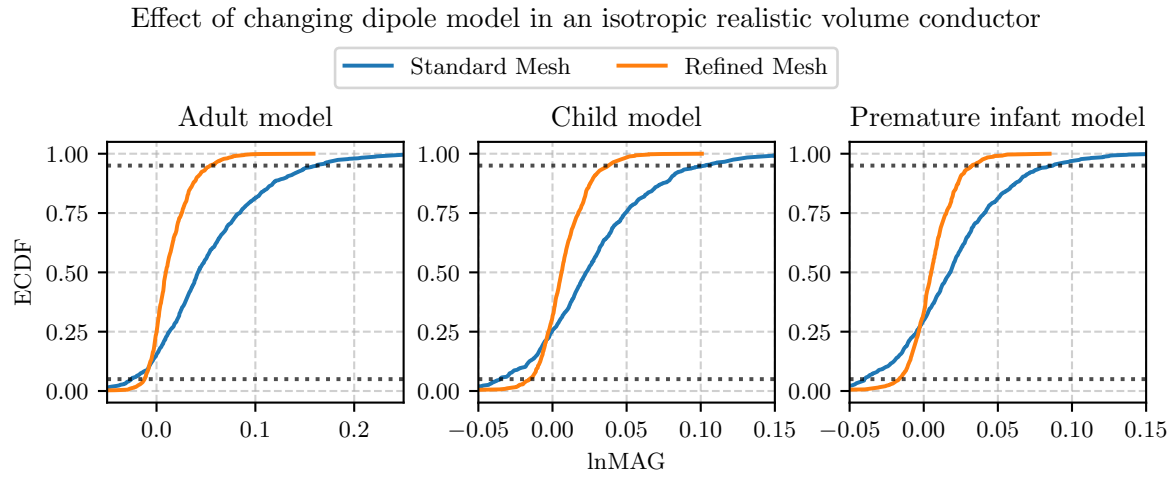

Figure 5.11.: ECDFs of lnMAG for isotropic forward calculations across different numerical approaches in the realistic head model. Curves compare Local Subtraction and St. Venant approaches on standard and refined meshes for adult, child and premature infant models.

are uniformly small, with 95% of the values being below 0.05 in all cases. The lnMAG produced by the Multipolar St. Venant approach exhibits a notable magnitude but is nearly symmetrically distributed. While the Local Subtraction approach, corrected the magnitude down in nearly all cases when using a finer mesh. Overall, adjustments for the two approaches were of similar magnitude. For both RDM and lnMAG, we see the Local Subtraction approach performing notably worse when using adult conductivities compared to all other results.

Hence, in the isotropic case, solution differences stemming from using different numeric approaches or using finer meshes are generally quite small, contrasting the anisotropic results.

RDM differences between approaches, obtained from the simulations with anisotropic gray matter conductivities, are shown in Figure 5.12. The results show generally bigger differences compared to the isotropic case and they show a significant increase in differences with the increase in anisotropy. Here, the child and premature infant models have shown an RDM of above 0.2 for over 5% of dipoles on the base grid as well as on its refinement. Across all models, the refined grid did produce significantly better results, but differences were still high. Similar results are shown for the lnMAG in Figure 5.13, seeing much bigger differences compared to the isotropic case, with an exception for the mildly anisotropic adult conductivities.

Comparing the results achieved on different mesh resolutions in Figure A.15, the difference again significantly increases with the increase of anisotropy. For the child and premature infant model, this means that the change in resolution causes a RDM of above

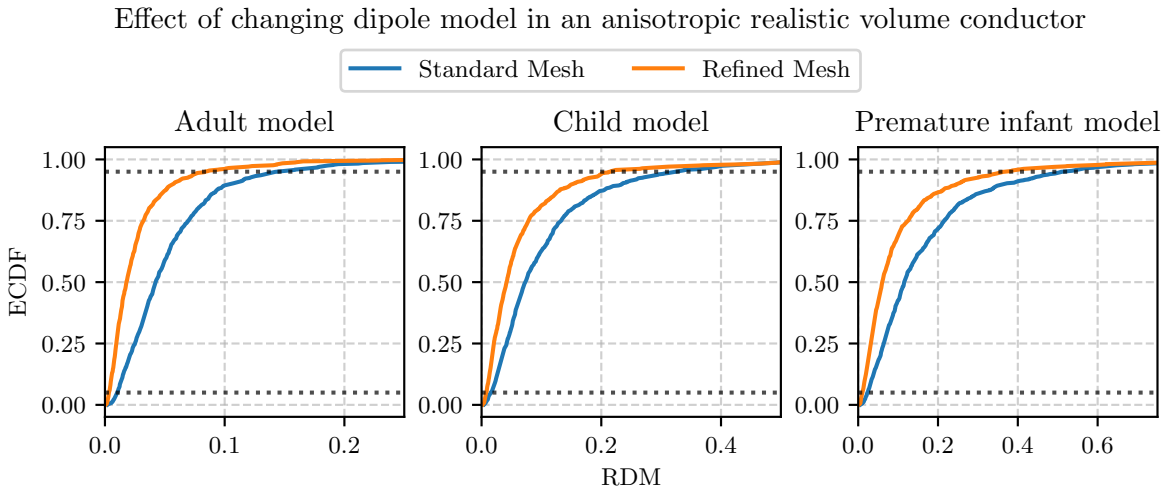

Figure 5.12.: ECDFs of RDM for anisotropic forward calculations across different numerical approaches in the realistic head model. Curves compare Local Subtraction and St. Venant approaches on standard and refined meshes for adult, child and premature infant models.

0.2 for over 5% of dipoles. The St. Venant approach showed in all our tests smaller changes than the Local Subtraction approach. Analogous observations can be made for the obtained lnMAG differences, displayed in Figure A.16.

Figure 5.14 shows the RE that was produced when comparing the corresponding isotropic and anisotropic results. As seen for previous anisotropic differences, the RE increases with the step up in conductivity and anisotropy. The median for adults lies around a RE of 0.05, for children around 0.18 and for premature infants around 0.35. Furthermore, all plots lie close together, with the St. Venant approach showing the smallest differences on the base mesh, while the biggest differences were produced by the Local Subtraction approach on the base mesh. This result was mirrored in the RDM results shown in Figure A.17. Showing medians for adults lying around a RDM of 0.03, for children around 0.1 and for premature infants around 0.15. While the lnMAG differences lie also close together, no clear ordering is apparent in Figure A.18, with medians for adults lying around a lnMAG of 0, for children around -0.1 and for premature infants around -0.3.

Overall, we see small differences for an isotropic gray matter compartment and significantly bigger differences in the anisotropic case. Noteworthy were that the isotropic adult conductivity on the standard mesh broke overarching patterns in the results and seemingly the found differences increase with the anisotropy ratio.

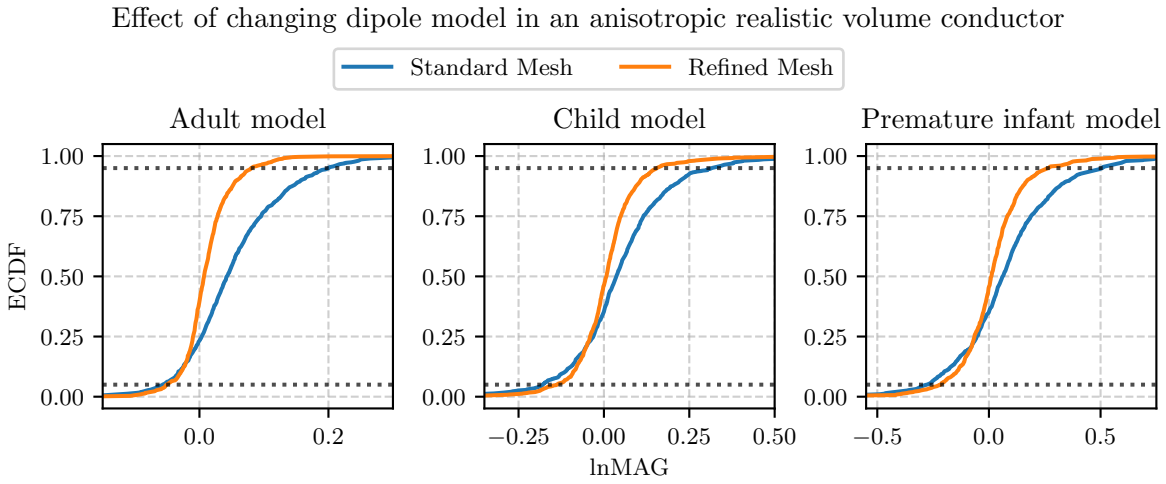

Figure 5.13.: ECDFs of lnMAG for anisotropic forward calculations across different numerical approaches in the realistic head model. Curves compare Local Subtraction and St. Venant approaches on standard and refined meshes for adult, child and premature infant models.

Discussion

The results obtained in the isotropic simulations fall within the expected range. Analyzing the differences introduced by using a finer grid reveals that the Local Subtraction approach shows greater changes than the Multipolar St. Venant approach only for the adult model on the rougher mesh. This phenomenon was already observed in Section 5.2 with isotropic sphere models. This is potentially caused by a greater conductivity jump in the patch region compared to the other conductivity scenarios.

In the anisotropic case, we observe significantly greater differences than in the isotropic simulations. Across all considered comparisons, the differences increase significantly with the increase in conductivity and anisotropy, a trend likely attributable to the increasing conductivity jumps between elements within the same compartment. Our findings indicate that the differences between the two numerical approaches were significant. Comparing the approaches across different grids further suggests insufficient convergence of both approaches at the current mesh resolutions.

For the adult model, with RDMs below 0.05 on the refined mesh, these results were in a reasonable range. However, for the child and premature infant models, a significant amount of dipoles produced an RDM of above 0.2. These findings challenge the confidence in the current results for children and premature infants further and suggest caution regarding sufficient convergence to the actual solution on the realistic meshes employed here. The aforementioned concerns regarding the trustworthiness of the simulation results, combined with the unclear optimal pairing of isotropic and anisotropic conductivity

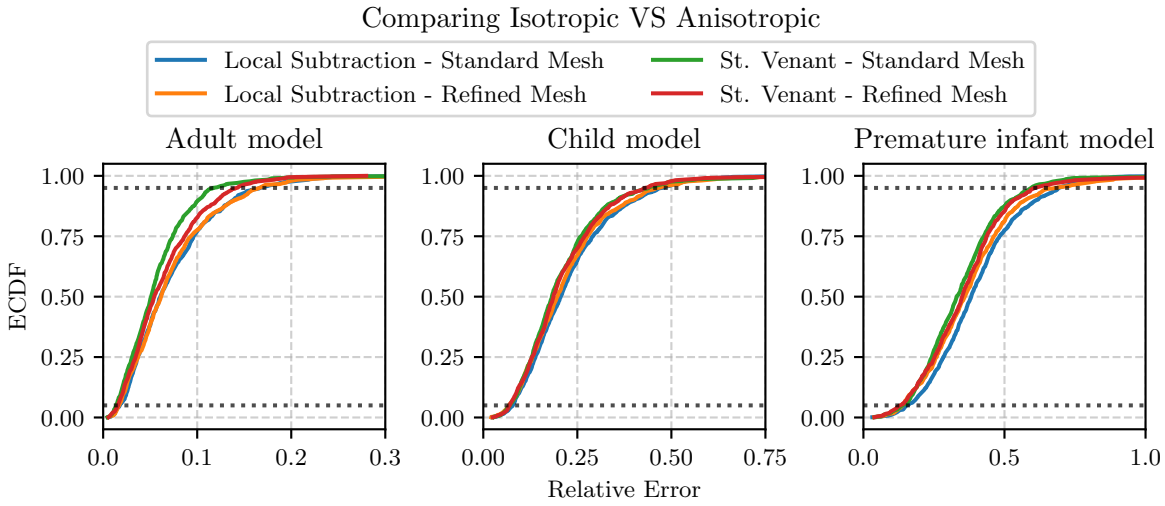

Figure 5.14.: ECDFs of relative errors comparing isotropic vs. anisotropic forward calculations in the realistic head model. Results shown for Local Subtraction and St. Venant approaches across standard and refined meshes for adult, child and premature infant models.

from Section 5.3, bring the comparison of isotropic and anisotropic results into question. Comparing against the results from Vorwerk et al. [66], which investigated individually modeling compartments against homogenization, would suggest that modeling gray matter anisotropy for children and premature infants may be of similar importance to modeling CSF.

Overall, this leads to the conclusion that a widespread usage of gray matter anisotropy in EEG forward modeling is not yet feasible, primarily because the current realistic meshes are not fine enough and the source of the large differences between results is not yet fully understood. Nevertheless, the sphere model tests have shown that gray matter anisotropy can be modeled and the anisotropy effect results warrant further investigation to support or reject those initial findings. Given that the Multipolar St. Venant approach performed very well in our sphere test and demonstrated more consistent results on the realistic head model, this approach might be more recommendable. Due to our findings, we would not advise trusting either approach without further validation against significantly finer meshes.

5.5. Visual Analysis of Fields and Currents in a Realistic Head Model

In previous sections, we investigated a large set of dipolar sources in a realistic head model with different anisotropic conductivities, producing results that were too unpredictable for EEG source reconstruction. To investigate and understand the predictions from the Local Subtraction and Multipolar St. Venant approaches, the produced potentials and secondary currents for three characteristic sources are visualized. The determined characteristic sources lie in a sulcal valley, on a gyral wall and on a gyral crown.

Methods

For the computations, the realistic head model described in Section 3.2 was used. Isotropic and anisotropic conductivities of adult, child and premature infant models, as described in Section 3.4, were assigned to this model. Forward simulations were then carried out on these models using the Multipolar St. Venant and Local Subtraction approaches. To interpret the differences using RE, RDM and lnMAG, electrodes were additionally assigned to the model, as described in Section 3.3.

Three source locations were picked from the region restricted to in Section 5.4 (visualized in Figure 5.9). In this region, a source was picked in a sulcal valley, one on a gyral wall and one on a gyral crown. It was visually ensured that the sources lie in the barycenter of a well-shaped gray matter tetrahedral element in the middle of the CSF compartment and that they were suitable for combined visualization. The positions and moments used are listed in Table 5.3 and are shown in Figure 5.15.

Table 5.3.: Point dipole sources used in Section 5.5.

Source	Position	Moment
1 Sulcal Valley	(−27.93, −16.45, 49.83)	(0.8345, −0.2482, −0.9651)
2 Gyral Wall	(−29.47, −15.58, 58.39)	(0.6896, −0.7233, −0.0364)
3 Gyral Crown	(−26.04, −22.33, 63.31)	(0.2161, 0.408, 0.887)

The presentation of the simulation results was organized in two ways.

First, the potentials that were produced on the plane that passes through all three sources were visualized. Note that the dipoles were chosen such that their moments were approximately parallel to this surface. The figures consist of a simulation using isotropic conductivities with the Local Subtraction method, which was used as a reference due to its established performance in this setting. Subsequently, the results from a simulation using anisotropic conductivities with the Local Subtraction approach are depicted, followed by the same calculation with the Multipolar St. Venant approach.

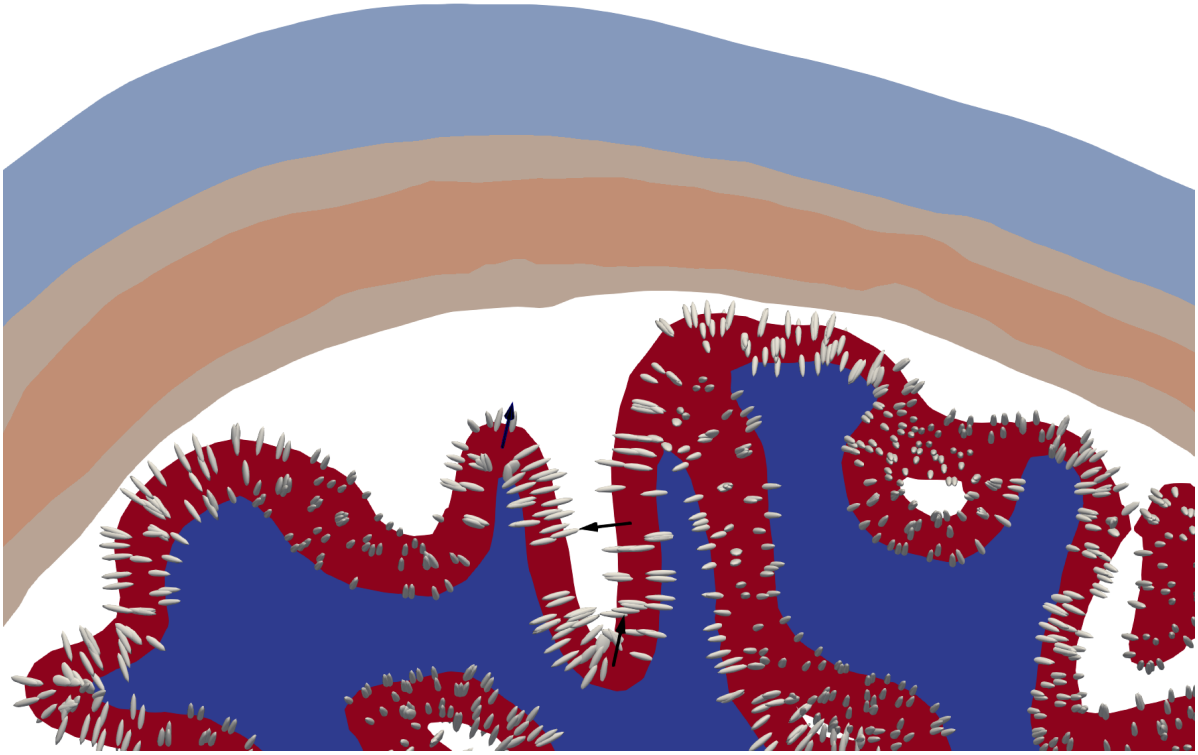

Figure 5.15.: 2D slice of the realistic head model used in Section 5.5, shown without the CSF compartment to avoid overlap. The anisotropic tensors are visualized by ellipsoids in the gray matter compartment with an anisotropy ratio of 5:1. Black arrows show the dipole location and orientation that are used throughout Section 5.5.

For the premature case, the currents produced by these sources in the isotropic and anisotropic cases, as predicted by the Multipolar St. Venant approach, were also visualized. The choice of approach for this was informed by the results of the potential simulations.

The choice of current visualization was inspired by Line Integral Convolution, which in full is beyond the scope of this work. Instead, the tools of ParaView were used. The plane spanned by the three source points, intersected with the realistic head model and color-coded by meshed compartment, is shown in the background for reference. On this plane, a "Point Plane Interpolator" filter was applied, yielding a regularly spaced grid of points lying in the plane, followed by a "Stream Tracer With Custom Sources" filter. This filter was parameterized to use the generated points as sources and the simulated current as the data for the flow lines calculation, which was executed for a few millimeters from the respective starting points. The flow lines were then color-coded using the logarithm

of the current magnitude[10].

Results

The RE, RDM and lnMAG that the anisotropic head models produced compared against the isotropic head model can be found in Table 5.4.

Inspecting the difference measures, we find in general low values for the RDM, in line with our optimization target in Section 5.3. Notably, there are two exceptionally large RDM values at the gyral crown source, produced by the Local Subtraction approach with premature infant conductivities and the Multipolar St. Venant approach with adult conductivities. Inspecting the simulated potentials in Figure 5.18, we find for the Local Subtraction simulation with infant conductivities a triangular divot in a predominantly positive region. The Multipolar St. Venant approach shows in all three conductivity settings a zero potential line that suggests a dipolar source pointing more towards the sulcal valley than the source we seek to simulate.

These low RDM values suggest that the higher relative errors might be driven by magnitude differences. This is in line with the lnMAG values, which rise sharply with increased gray matter conductivity. This mostly positive rise suggests that in this small sample, the anisotropic conductivity leads to bigger magnitudes at the electrodes. Notable for the magnitude differences is the source on the gyral wall, producing lnMAG values near zero for adult and child conductivities with a jump for the premature infant. The potential visualizations in Figure 5.17 show, for the anisotropic simulations and especially in high conductivity settings, a distorted zero potential line that varies in direction between approaches. Interestingly, this is already evident in the adult and child models, where we see small lnMAG values.

The source in the sulcal valley shows difference measures strictly increasing with gray matter conductivity, while in the potential visualization in Figure 5.16, we note that the St. Venant type approach, as for the two other sources, places the zero potential line not directly at the dipolar source.

The current visualizations with premature infant conductivities for the sulcal valley source are displayed in Figure 5.19, for the gyral wall source in Figure 5.20 and for the gyral crown source in Figure 5.21. In these figures, the effect of the anisotropic conductivity is most evident. No source shows major differences between the isotropic and anisotropic settings. Rather, the flow lines get slightly straightened, seeming to lead to slightly changed exit points for currents crossing the gray matter, smearing and broadening the overall image. In the isotropic compartments, which notably includes the white matter here, this does not seem to lead to big changes. With sufficient distance to

[10] A step by step guide may be found along the implementations under `https://gitlab.dune-project.org/timon.gronotte/thesis-experiments/-/tree/main/11_single_source_simulation?ref_type=heads`

the gray matter compartment, for example, in the skull compartments, changes are no longer visually apparent.

Table 5.4.: Table showing the relative error, relative difference measure and logarithmic magnitude error when comparing the results from anisotropic head models with the isotropic head models at the electrode positions.

Source	Model	Local Subtraction			Multipolar St. Venant		
		RE	RDM	lnMAG	RE	RDM	lnMAG
1	Adult	0.06071	0.02587	0.05314	0.0586	0.0571	0.01156
sulcal	Child	0.31486	0.08835	0.26108	0.30599	0.07767	0.25694
valley	Premature	0.69163	0.13743	0.5119	0.83239	0.10826	0.59855
2	Adult	0.02777	0.01056	-0.02607	0.06989	0.05955	-0.03916
gyral	Child	0.03515	0.01553	0.03093	0.07111	0.07115	-0.00142
wall	Premature	0.30536	0.03953	0.26391	0.27832	0.11555	0.22043
3	Adult	0.03736	0.03063	-0.02211	0.27189	0.11703	-0.29083
gyral	Child	0.11584	0.10693	0.03845	0.21198	0.08334	-0.22117
crown	Premature	0.46124	0.24616	0.30817	0.17653	0.11896	-0.14814

Discussion

The low RDM values align with our optimization goal and indicate that a properly calibrated isotropic conductivity model may prove sufficient to accurately reconstruct source positions, provided these results are confirmed through statistical testing. However the current results on the tested meshes do not seem to support this fully, see the previous Section 5.4. However, the lnMAG measure shows a significant and mostly positive reaction to the change in both conductivity and anisotropy. Given its direct link to source magnitude reconstruction, using an isotropic approximation with the current parameters would likely lead to significant errors in estimating the source strength. This finding is consistent with results from the sphere model, see Section 5.1, where the minimum errors for lnMAG and RDM occurred at different conductivities, thus making a simultaneous, accurate reconstruction of both position and magnitude using isotropic models unlikely.

In general, the high relative error values observed for premature infant conductivities suggest that assuming the wrong anisotropy in clinical practice could introduce significant reconstruction errors.

Crucially, the RDM and lnMAG also displayed significant variance between the two anisotropic approaches. For the source on the gyral crown, the Multipolar St. Venant approach initially appeared to struggle to properly approximate the target source but interestingly showed smaller RDM values with increasing anisotropy. At the gyral crown

and the sulcal valley, the regions with high curvature, the Multipolar St. Venant approach often yielded a smaller RDM. These are notably regions where the Local Subtraction method may have run into issues with the rapid changes in conductivity.

Conversely, for the source on the gyral wall with low curvature, the Local Subtraction approach produced a much smaller RDM than the Multipolar St. Venant approach.

These differences show that, at this grid resolution, the "correct" approach might change based on the specific head geometry and source location. While we expect both methods to converge to a single solution with refined grids, we deliberately used a realistically mesh resolution, as the high computational cost of further mesh refinements is a practical concern.

Regarding the visualizations, they are instrumental in gaining an intuition for how the anisotropic gray matter compartment affects currents and potentials. Yet, they may contain visualization artifacts and, most importantly, they offer only a two-dimensional view of a complex three-dimensional problem. This inherent geometric complexity may explain why we cannot perfectly correlate every effect seen in a distance measure with a visual source in the figures.

Overall, these three characteristic source locations demonstrate that gray matter anisotropy can cause significant effects that depend on the source location, highlighting the difficulty in accurately and precisely predicting its effect. This is evident in the divergence between the two simulation approaches and complicates statistical analysis.

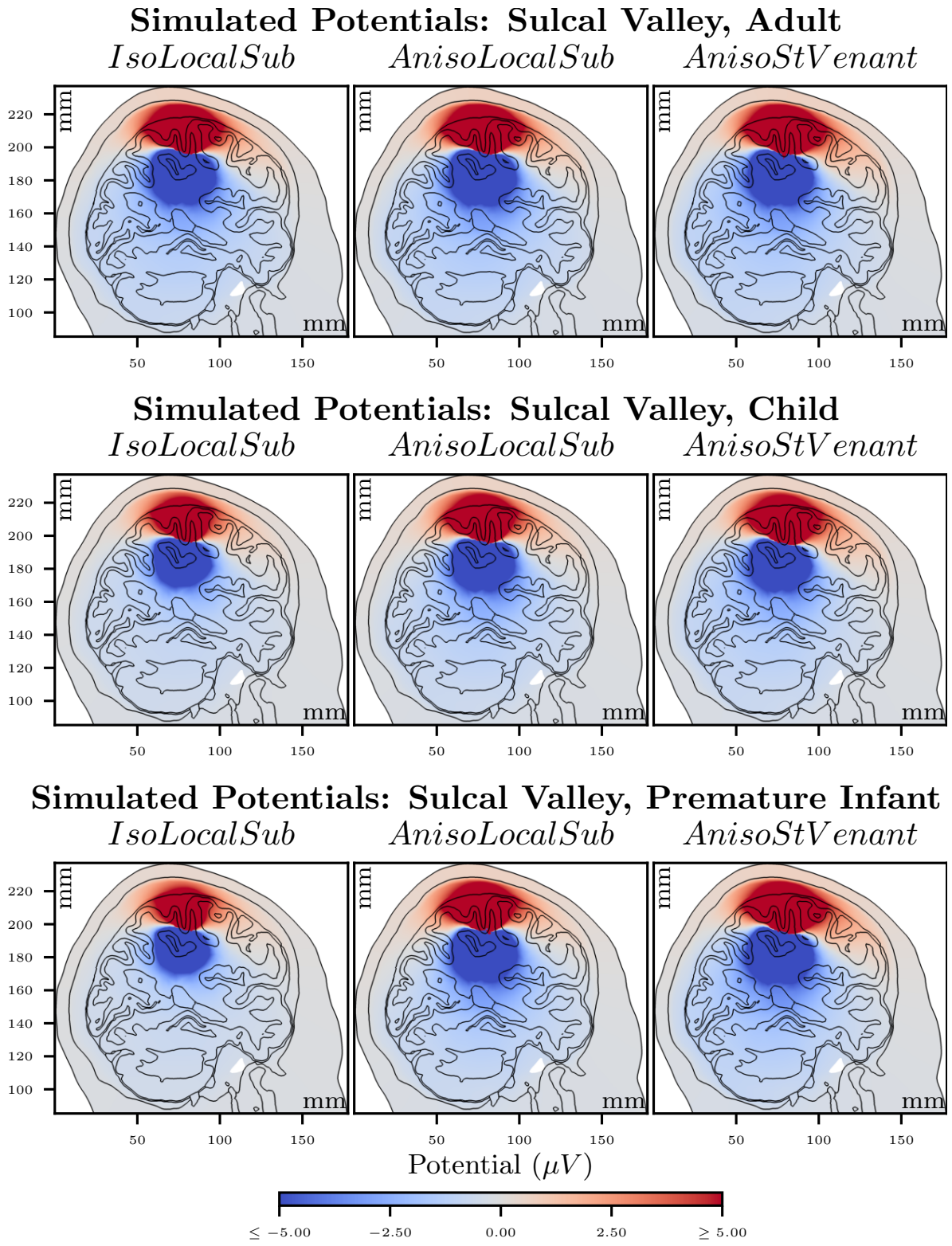

Figure 5.16.: Potentials produced in a sulcal valley, assuming adult, child or premature infant conductivities. Computed for isotropic conductivities with Local Subtraction (IsoLocasSub) and with anisotropic conductivity using Local Subtraction (AnisoLocalSub) and multipolar St. Venant (AnisoStVenant). See Section 5.5.

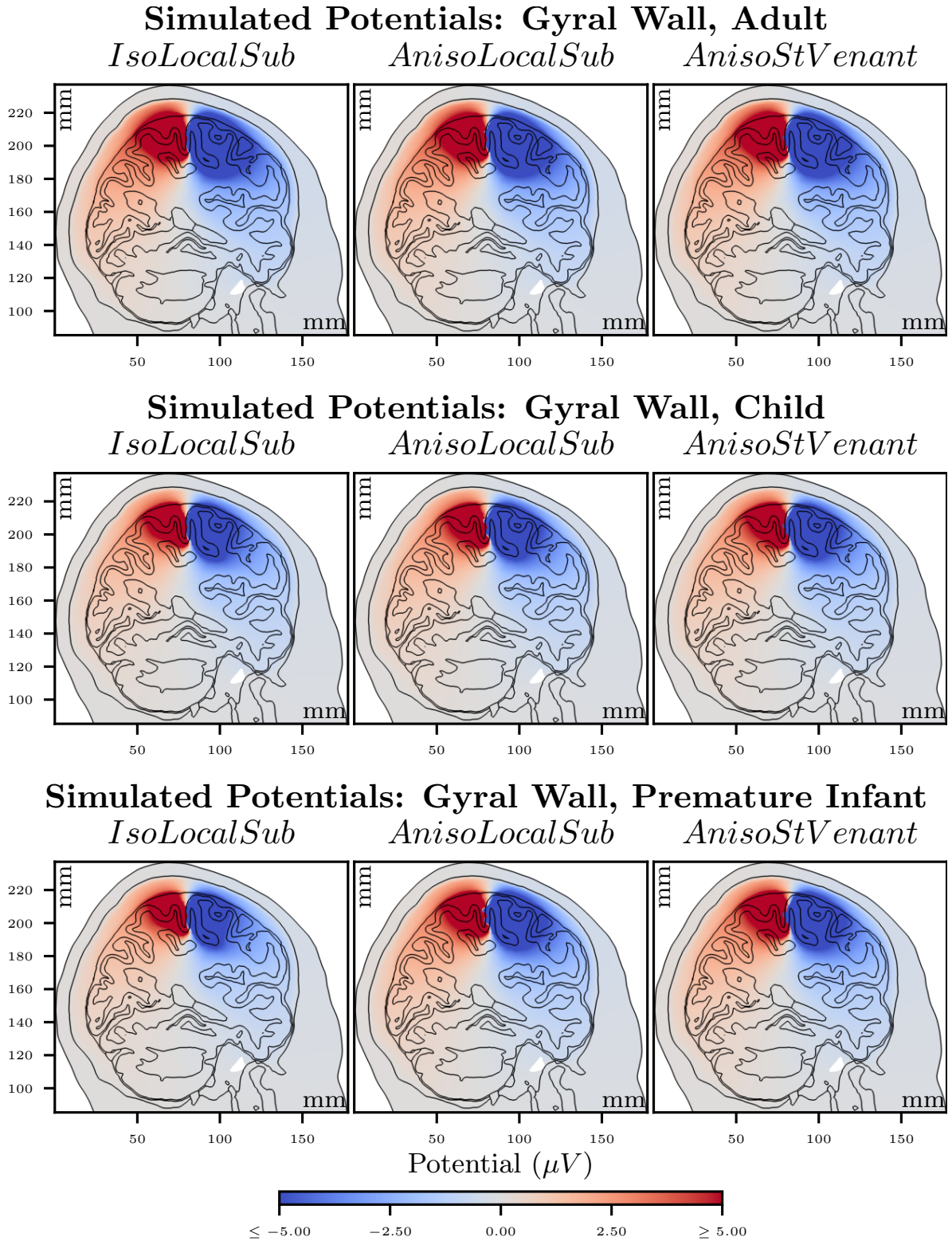

Figure 5.17.: Potentials produced in a gyral wall, assuming adult, child or premature infant conductivities. Computed for isotropic conductivities with Local Subtraction (IsoLocasSub) and with anisotropic conductivity using Local Subtraction (AnisoLocalSub) and multipolar St. Venant (AnisoStVenant). See Section 5.5.

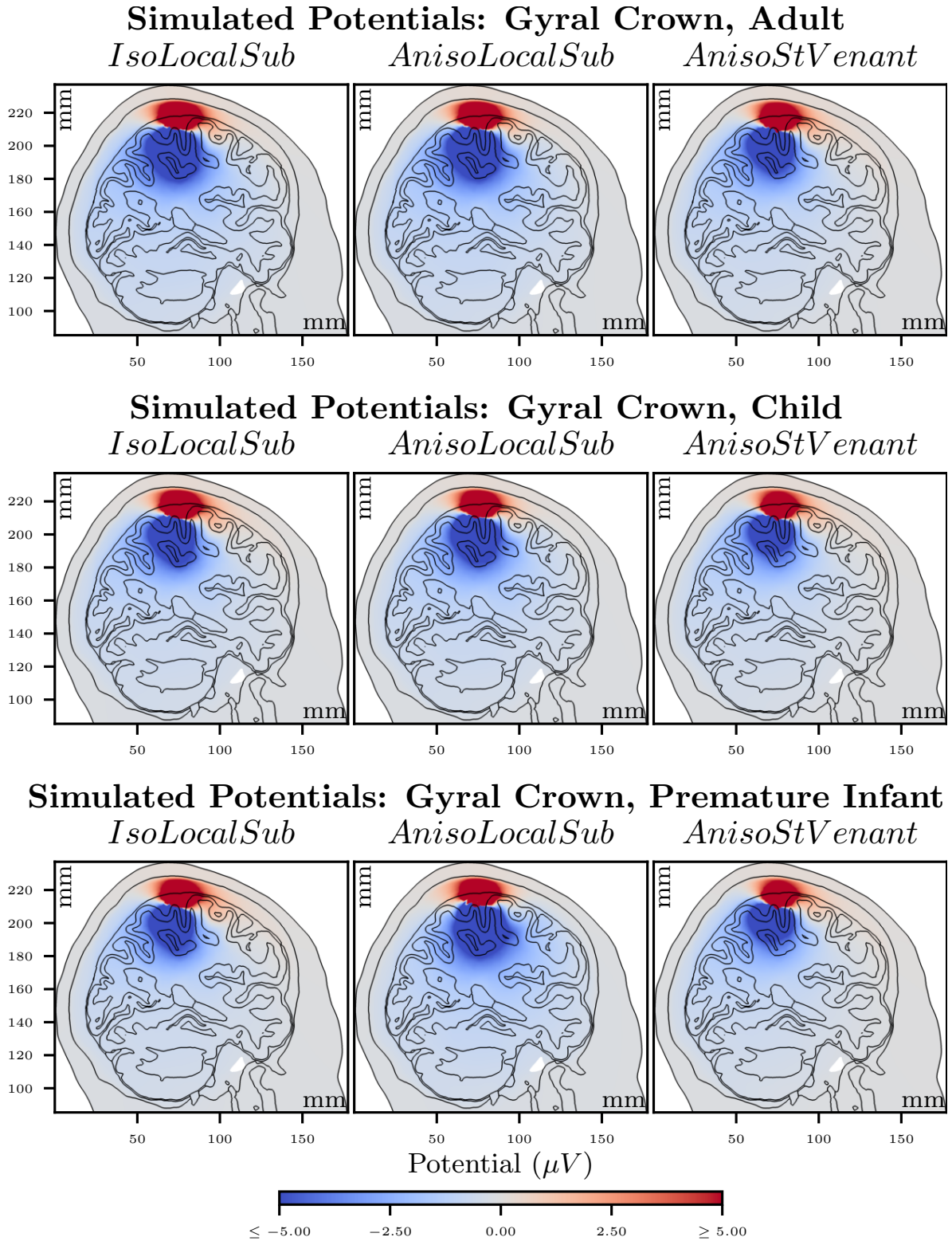

Figure 5.18.: Potentials produced on a gyral crown, assuming adult, child or premature infant conductivities. Computed for isotropic conductivities with Local Subtraction (IsoLocasSub) and with anisotropic conductivity using Local Subtraction (AnisoLocalSub) and multipolar St. Venant (AnisoStVenant). See Section 5.5.

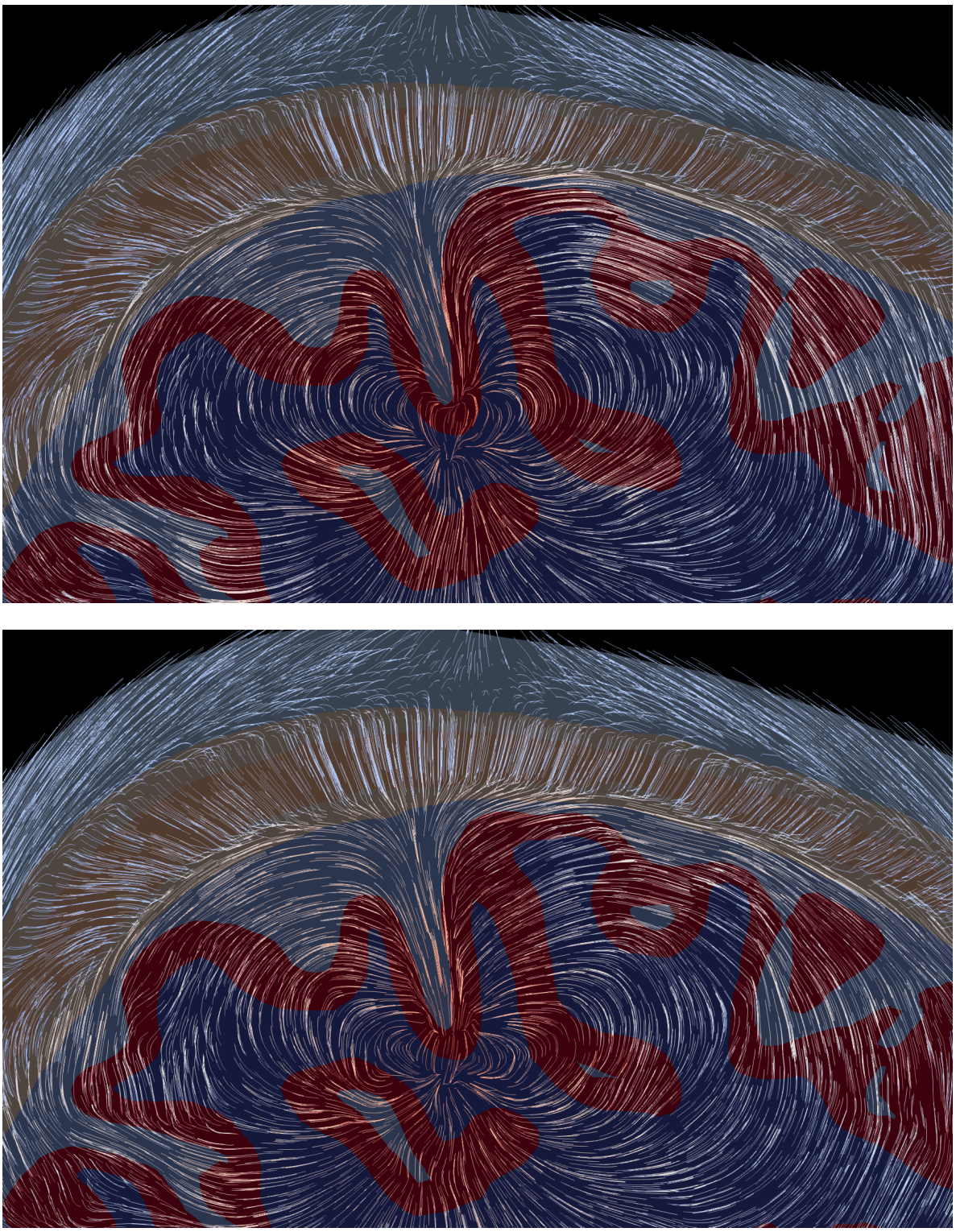

Figure 5.19.: Visualization of currents produced by a dipolar source in a sulcal valley. Background shows the color-coded brain compartment overlaid with 5mm long flow lines of the produced current vector field, logarithmically color-coded by current magnitude. See methods in Section 5.5.

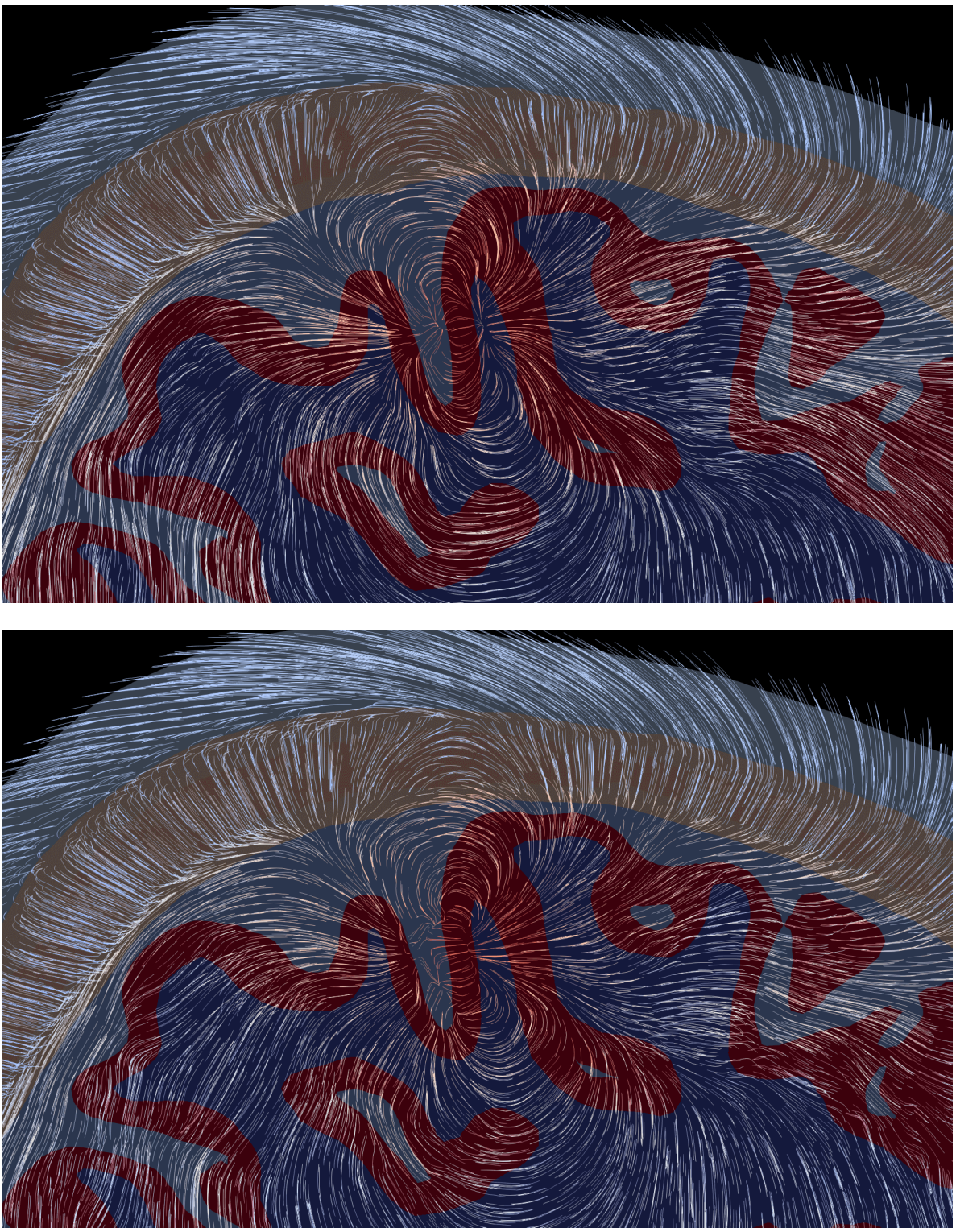

Figure 5.20.: Visualization of currents produced by a dipolar source in a gyral wall. Background shows color coded brain compartment overlayed with 5mm long flow lines of the produced current vector field, logarithmically color coded by current magnitude. See methods in Section 5.5.

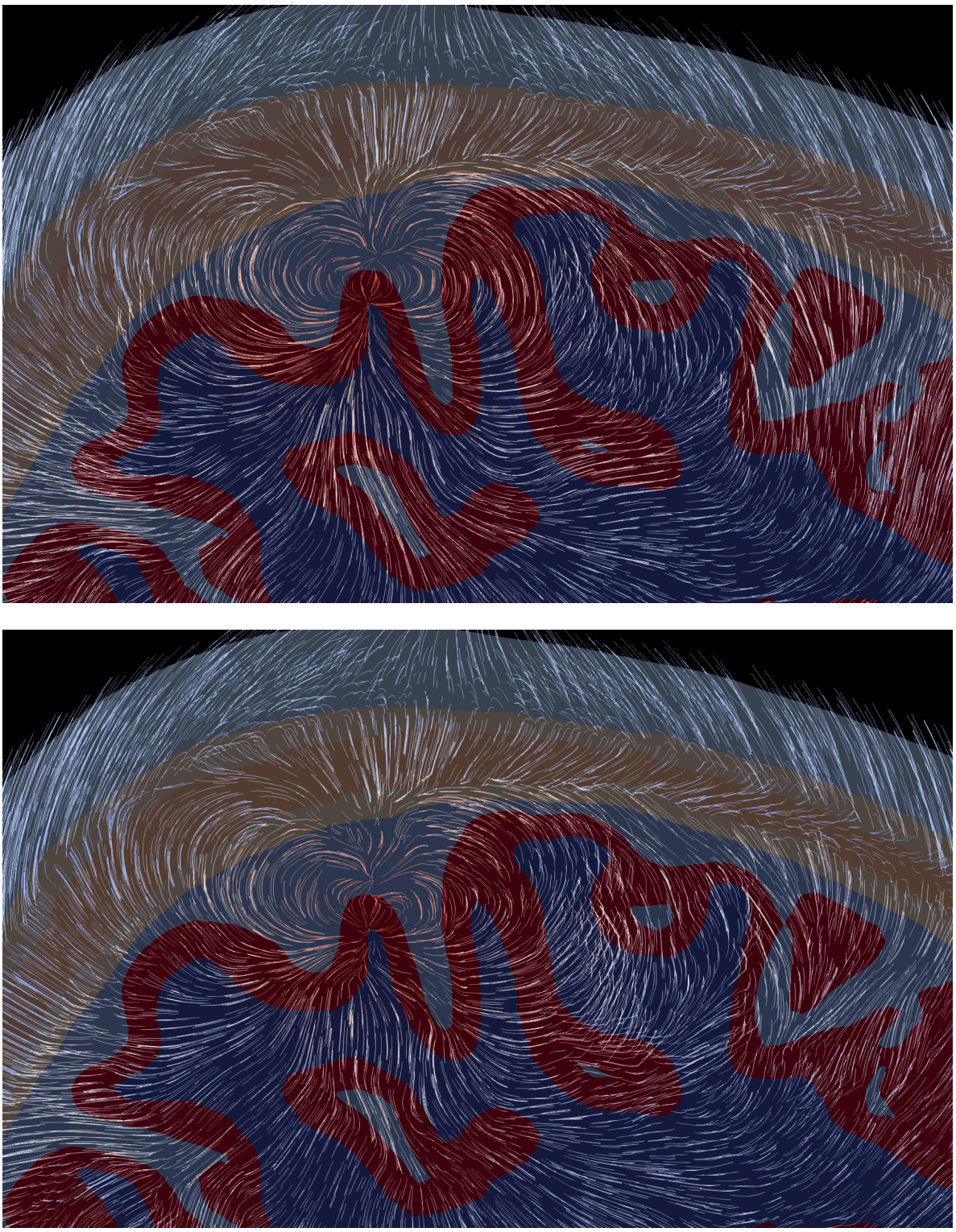

Figure 5.21.: Visualization of currents produced by a dipolar source on a gyral crown. Background shows the color-coded brain compartment overlaid with 5mm long flow lines of the produced current vector field, logarithmically color-coded by current magnitude. See methods in Section 5.5.

6. Anisotropic MEG

The previously discussed EEG forward problem and numerical approaches were compatible with anisotropy at the dipole location. While the Multipolar St. Venant approach can be used as a base for the MEG Forward problem, the Local Subtraction approach would need to be generalized.

The following rules out many approaches to generalize the approach before numerically evaluating approximate solutions.

6.1. Obstacles to Anisotropic Local Subtraction in MEG

The MEG forward problem was derived in Section 2.1.2. The final formulation of the problem in Definition 3 came down to evaluating an integral for the primary magnetic field and one for the secondary magnetic field as a result of the Biot-Savart law.

Remark 19. *While the following use of the formulas for the magnetic fields together with point dipoles is common practice, it is mathematically questionable as in the derivations of those equations, we utilized sufficient regularity of the current density. As we are unaware of a proof showing the results for Dirac distributions, the following has an open assumption. However, in his PhD thesis, Malte Höltershinken [34] rigorously proved that the resulting formulas for the isotropic case are indeed correct. While the proof even entailed a more efficient way to compute the MEG fluxes, the results cannot be utilized here, as they have isotropic conductivity as a core assumption.*

Assuming $\Omega \subset \mathbb{R}^3$ to be a head domain as in 2.2.2 and a point dipole as in Equation (2.19) at position $x_0 \in \Omega$ and moment $M \in \mathbb{R}^3$, the primary magnetic field can be easily evaluated:

$$\begin{aligned} B^P(x) &= \frac{\mu_0}{4\pi} \int_\Omega j^p(y) \times \frac{x-y}{||x-y||^3} dV(y) = \frac{\mu_0}{4\pi} \int_\Omega \delta_{x_0}(y) \cdot \left(M \times \frac{x-y}{||x-y||^3} \right) dV(y) \\ &= \frac{\mu_0}{4\pi} \cdot M \times \frac{x-x_0}{||x-x_0||^3} \end{aligned} \tag{6.1}$$

Notice that this is still true in the anisotropic case since the conductivity σ does not appear in that equation.

Assume additionally a tensor field $\sigma : \Omega \to \mathbb{R}^{n \times n}$ which is symmetric positive definite $\forall x \in \Omega$, such that there is a Local Subtraction solution. Meaning there is a neighborhood

$x_0 \in U$ such that $\sigma(x_0) = \sigma(U)$, sets $\tilde{\Omega}, \Omega^\infty \subset \Omega$ and function $u^c : \Omega \to \mathbb{R}$ such that $u = u^c + \chi u^\infty$, where χ is defined as in Equation (2.29) and u^∞ the fundamental solution as in Equation (2.28), weakly solves the associated EEG forward problem.

Inserting such u into Equation (2.17) for the secondary magnetic field yields:

$$B^S(s) = \frac{\mu_0}{4\pi} \int_\Omega \sigma(y) \nabla \left(u^c + \chi u^\infty\right)(y) \times \frac{s-y}{||s-y||^3} dV(y) \tag{6.2}$$

This cannot be evaluated as easily due to the singular gradient of u^∞. Since we assumed σ to be constant on U with value $\sigma^\infty = \sigma(x_0)$, this integral can be split into:

$$\begin{aligned} B^S(s) = \frac{\mu_0}{4\pi} \int_{\Omega \setminus U} \sigma(y) \nabla \left(u^c + \chi u^\infty\right)(y) \times \frac{s-y}{||s-y||^3} dV(y) \\ + \frac{\mu_0}{4\pi} \int_U \sigma^\infty \nabla u^\infty(y) \times \frac{s-y}{||s-y||^3} dV(y) \end{aligned} \tag{6.3}$$

The first term on the right-hand side does not contain a singularity and could be evaluated numerically. The second term, however, does contain a singularity and needs to be solved separately. Hence, much of the following will be concerned with attempting to solve:

$$\int_U \sigma^\infty \nabla u^\infty(y) \times \frac{s-y}{||s-y||^3} dV(y) \text{ for } s \in \mathbb{R}^3 \tag{6.4}$$

In the case that σ^∞ is isotropic, the original Local Subtraction publication by Hölter-shinken et al. [33] derived a method to calculate this integral despite the singularities. This method relied on being able to pull the isotropic σ out of the integral since it is essentially a scalar, followed by rewriting the cross product as a curl by the following computation:

$$\begin{aligned} \nabla_y u^\infty(y) \times \frac{s-y}{||s-y||^3} &= \nabla_y u^\infty(y) \times \nabla_y \left[\frac{1}{||s-y||}\right] \\ &= u(y) \left(\nabla \times \nabla_y \left[\frac{1}{||s-y||}\right]\right) + \nabla_y u^\infty(y) \times \nabla_y \left[\frac{1}{||s-y||}\right] \\ &= \nabla_y \times \left[u^\infty(y) \nabla_y \frac{1}{||s-y||}\right] \end{aligned} \tag{6.5}$$

Where we used ∇_y to denote the gradient with respect to y and that the curl of the gradient of a scalar function is 0, allowing the use of identity (2.9). After careful consideration of the singularity, this allows for an application of Stokes' theorem, yielding a singularity-free boundary integral which can finally be numerically evaluated [15].

Before going into the difficulties with generalizing this approach, some preparations are needed.

6.2. Cross Product Identities

To help in the following computations, two cross product identities will be proved, using the

Definition 20 (Levi-Civita-Symbol)**.** *The Levi-Civita-Symbol is given for* $i, j, k \in \{1, 2, 3\}$ *by [53]:*

$$\epsilon_{ijk} = \begin{cases} +1 & \text{if } (i,j,k) \text{ is an even permutation of } 1,2,3 \\ -1 & \text{if } (i,j,k) \text{ is an odd permutation of } 1,2,3 \\ 0 & \text{otherwise} \end{cases} \tag{6.6}$$

Lemma 21. *Let* $M \in \mathbb{R}^{n\times n}$ *be invertible and* $a, b \in \mathbb{R}^n$*. Then we have:*

$$(Ma) \times (Mb) = \det(M) \left(M^{-1}\right)^T (a \times b) \tag{6.7}$$

Proof. Let $M \in \mathbb{R}^{n\times n}$ be invertible and $a, b, x \in \mathbb{R}^n$. We denote by (a, b, x) the $\mathbb{R}^{3\times 3}$ matrix whose columns are respectively given by a, b and x. For the determinant, we use the Leibniz formula with the Levi-Civita-Symbol, i.e., $\det(M) = \sum_{i,j,k=1}^{3} \epsilon_{ijk} M_{1i} M_{2j} M_{3k}$ and we have $a \times b = \sum_{i,j,k=1}^{3} \epsilon_{ijk} a_i b_j \vec{e_k}$ where $\vec{e_i}$ are the canonical basis vectors. This immediately reveals for $v, w, z \in \mathbb{R}^3$ the identity:

$$\det(v, w, z) = \sum_{i,j,k=1}^{3} \epsilon_{ijk} v_i w_j z_k = z^T \cdot \left(\sum_{i,j,k=1}^{3} \epsilon_{ijk} v_i w_j \vec{e_k} \right) = \langle v \times w, z \rangle \tag{6.8}$$

This in turn allows us to compute:

$$\begin{aligned} \left\langle M^T \left([Ma] \times [Mb] \right), x \right\rangle &= \langle [Ma] \times [Mb], Mx \rangle \\ &= \det(Ma, Mb, Mx) \\ &= \det(M \cdot (a, b, x)) \\ &= \det(M) \det(a, b, x) \\ &= \det(M) \langle a \times b, x \rangle \end{aligned} \tag{6.9}$$

Since x was arbitrary, we have $M^T ([Ma] \times [Mb]) = \det(M) a \times b$, which is equivalent to the claim, completing the proof. □

Lemma 22. *Let* $M \in \mathbb{R}^{n\times n}$ *be a symmetric matrix and* $a, b \in \mathbb{R}^n$*.*

$$M(a \times b) = tr(M)(a \times b) - [(Ma) \times b] - [a \times (Mb)] \tag{6.10}$$

Proof. As before, we have $a \times b = \sum_{i,j,k=1}^{3} \epsilon_{ijk} a_i b_i \vec{e_i}$ where $\vec{e_i}$ are the canonical basis vectors. First, assume that M is a diagonal matrix. Then we have:

$$\begin{aligned}
M(a \times b) &= \sum_{i,j,k,l=1}^{3} M_{lk} \epsilon_{ijk} a_i b_j \vec{e_l} \\
&= \sum_{\substack{i,j,k,l=1 \\ m=k}}^{3} M_{lk} \epsilon_{ijk} a_i b_j \vec{e_l} + \underbrace{\sum_{\substack{i,j,k,l=1 \\ m=i}}^{3} M_{lk} \epsilon_{ijk} a_i b_j \vec{e_l} + \sum_{\substack{i,j,k,l=1 \\ m=j}}^{3} M_{lk} \epsilon_{ijk} a_i b_j \vec{e_l}}_{\text{equal 0 since } M \text{diagonal matrix}} \\
&= \sum_{i,j,k=1}^{3} \left[\operatorname{tr}(M) \epsilon_{ijk} a_i b_j - \sum_{k \neq n=1}^{3} M_{nn} \epsilon_{ijk} a_i b_j \right] \vec{e_l} \\
&= \sum_{i,j,k=1}^{3} \left[\operatorname{tr}(M) \epsilon_{ijk} a_i b_j - \epsilon_{ijk} \underbrace{M_{ii} a_i}_{=(Ma)_i} b_j - \epsilon_{ijk} a_i \underbrace{M_{jj} b_j}_{=(Mb)_j} \right] \vec{e_l} \\
&= \operatorname{tr}(M)(a \times b) - (Ma) \times b - a \times (Mb)
\end{aligned} \tag{6.11}$$

Leaving only the case where the diagonal of M is empty since the cross product is bilinear.
Hence, in the following, we assume all entries on the diagonal of M are 0 and thereby $\operatorname{tr}(M) = 0$ and:

$$\begin{aligned}
M(a \times b) &= \underbrace{\sum_{\substack{i,j,k,l=1 \\ l=k}}^{3} M_{lk} \epsilon_{ijk} a_i b_j \vec{e_l}}_{\text{equals 0}} + \sum_{\substack{i,j,k,l=1 \\ l=i}}^{3} M_{lk} \epsilon_{ijk} a_i b_j \vec{e_l} + \sum_{\substack{i,j,k,l=1 \\ l=j}}^{3} M_{lk} \epsilon_{ijk} a_i b_j \vec{e_l} \\
&= \sum_{i,j,k=1}^{3} M_{ik} \epsilon_{ijk} a_i b_j \vec{e_i} + \sum_{i,j,k=1}^{3} M_{jk} \epsilon_{ijk} a_i b_j \vec{e_j} \\
&= \sum_{i,j,k=1}^{3} \left[M_{ki} \epsilon_{kji} a_k b_j + (1-1) \epsilon_{kji} M_{ji} a_j b_j \right] \vec{e_k} + \\
&\quad \sum_{i,j,k=1}^{3} \left[M_{jk} \epsilon_{ikj} a_i b_k + (1-1) \epsilon_{ikj} M_{ij} a_i b_i \right] \vec{e_k} \\
&= -(Ma) \times b - a \times (Mb) + \\
&\quad \sum_{i,j,k=1}^{3} \left[-\epsilon_{kji} M_{ji} a_j b_j - \underbrace{\epsilon_{ikj} M_{ij} a_i b_i}_{\text{Change name of } i \text{ and } j \text{ to cancel the first term.}} \right] \vec{e_k}
\end{aligned} \tag{6.12}$$

Thus completing the proof. □

6.3. Reduction and Exclusion: Analytical Efforts in Anisotropic Local Subtraction

The following first shows that solving the integral in Equation (6.4) can be reduced to solving it for positive definite diagonal conductivity tensors, as a general $\sigma^\infty \in \mathbb{R}^{n\times n}$ may not be easily removed from a cross product. This simplification is then used to show the trick shown in Equation (6.5) cannot be recovered by substitution or linear transformation.

In the following, we will use $d_s(y) := d(s,y) := ||s-y||$ for the substitution:

$$\nabla d_s^{-1} = \frac{s-y}{||s-y||^3} \tag{6.13}$$

Starting with the reduction to the diagonal case:

Lemma 23. *For $\sigma \in \mathbb{R}^{3\times3}$ symmetric positive definite and $x_0, M, s \in \mathbb{R}^3$ and a compact set $U \subset \mathbb{R}^3$, there is a unitary matrix $O \in \mathbb{R}^{3\times3}$ and a diagonal matrix $D \in \mathbb{R}^{3\times3}$ such that:*

$$\int_U \sigma^\infty \nabla u^\infty_{x_0,M,\sigma} \times \nabla d_s^{-1} dV = O \int_{O^T U} \left(D \nabla u^\infty_{O^T x_0, O^T M, D} \right) \times \nabla d^{-1}_{O^T s} dV \tag{6.14}$$

Proof. Let $\sigma \in \mathbb{R}^{3\times3}$ be symmetric positive definite and $x_0, M, s \in \mathbb{R}^3$. Then we can use the spectral theorem for normal matrices (Theorem 2.5.3 in [35]) to find a unitary Matrix $O \in \mathbb{R}^{3\times3}$ and a diagonal matrix $D \in \mathbb{R}^{3\times3}$ such that $\sigma = ODO^T$. Recall that in the real case, we then have $O^T = O^{-1}$, $\sigma^{-1} = OD^{-1}O^T$ and $\det(\sigma) = \det(D)$. Then we can define a diffeomorphism on $\mathbb{R}^3$ by $\Phi_O(x) = O \cdot x$ and calculate the concatenation with d_s^{-1}:

$$\begin{aligned} d_s^{-1} \circ \Phi_O(x) &= \frac{1}{\langle s - Ox, s - Ox \rangle^{\frac{1}{2}}} \\ &= \frac{1}{\langle O\left(O^T s - x\right), O\left(O^T s - x\right) \rangle^{\frac{1}{2}}} \\ &= \frac{1}{\langle O^T s - x, O^T s - x \rangle^{\frac{1}{2}}} \\ &= d^{-1}_{O^T s}(x) \end{aligned} \tag{6.15}$$

And the concatenation with the infinity potential (2.28):

$$\begin{aligned} u^{\infty}_{x_0,M,\sigma} \circ \Phi_O(x) &= \frac{1}{4\pi\sqrt{\det \sigma}} \frac{\langle M, \sigma^{-1}(Ox - x_0)\rangle}{\langle \sigma^{-1}(Ox - x_0), Ox - x_0\rangle^{\frac{3}{2}}} \\ &= \frac{1}{4\pi\sqrt{\det \sigma}} \frac{\left\langle M, OD^{-1}\left(x - O^T x_0\right)\right\rangle}{\langle \sigma^{-1} O(x - O^T x_0), O(x - O^T x_0)\rangle^{\frac{3}{2}}} \\ &= \frac{1}{4\pi\sqrt{\det D}} \frac{\left\langle O^T M, D^{-1}\left(x - O^T x_0\right)\right\rangle}{\langle D^{-1}(x - O^T x_0), x - O^T x_0\rangle^{\frac{3}{2}}} \\ &= u^{\infty}_{O^T x_0, O^T M, D}(x) \end{aligned} \tag{6.16}$$

With these results and the change of variable formula [36], we can finally compute:

$$\begin{aligned} \int_U \sigma \nabla u^{\infty}_{x_0,M,\sigma} \times \nabla d_s^{-1} dV &= \int_U \left(ODO^T \nabla u^{\infty}_{x_0,M,\sigma}\right) \times \nabla d_s^{-1} dV \\ \text{Change of variable} \rightarrow &= \int_{O^T U} \left(ODO^T \nabla u^{\infty}_{x_0,M,\sigma} \circ \Phi_O\right) \times \nabla d_s^{-1} \circ \Phi_O dV \\ \text{Chain rule} \rightarrow &= \int_{O^T U} \left(OD\nabla\left[u^{\infty}_{x_0,M,\sigma} \circ \Phi_O\right]\right) \times \left(O\nabla\left[d_s^{-1} \circ \Phi_O\right]\right) dV \\ \text{Lemma 21} \rightarrow &= O \int_{O^T U} \left(D\nabla\left[u^{\infty}_{x_0,M,\sigma} \circ \Phi_O\right]\right) \times \nabla\left[d_s^{-1} \circ \Phi_O\right] dV \\ &= O \int_{O^T U} \left(D\nabla u^{\infty}_{O^T x_0, O^T M, D}\right) \times \nabla d^{-1}_{O^T s} dV \end{aligned} \tag{6.17}$$

□

This lemma essentially means that instead of calculating the integral for a general symmetric positive definite σ, we may calculate the integral of an equivalent problem with a positive definite diagonal σ. Utilizing this result, it is shown that the trick cannot be applied through a substitution:

Lemma 24. *For $\sigma \in \mathbb{R}^{3\times 3}$ symmetric positive definite, $x_0, M \in \mathbb{R}^3$ and $u_{x_0,M,\sigma}$ defined by Equation (2.28), there is in general no twice partially differentiable $v : \mathbb{R}^3 \setminus \{x_0\} \to \mathbb{R}$ such that $\nabla v = \sigma \nabla u_{x_0,M,\sigma}$ on $\mathbb{R}^3 \setminus \{x_0\}$.*

Proof. We start by restricting the dipole location to the origin $x_0 = 0$ and to a diagonal conductivity

$$\sigma = \begin{pmatrix} \sigma_1 & 0 & 0 \\ 0 & \sigma_2 & 0 \\ 0 & 0 & \sigma_3 \end{pmatrix} \text{ for } \sigma_1, \sigma_2, \sigma_3 \in \mathbb{R}^3 \text{ with } \sigma_1 \neq \sigma_2 \tag{6.18}$$

and assume we have a $v : \mathbb{R}^3 \setminus \{x_0\} \to \mathbb{R}$ such that $\nabla v = \sigma \nabla u_{x_0,M,\sigma}$ on $\mathbb{R}^3 \setminus \{x_0\}$. We can then quickly calculate:

$$\nabla \times \nabla v = \nabla \times (\sigma \nabla u_{x_0,M,\sigma}) = \begin{pmatrix} (\sigma_3 - \sigma_2)\partial_2\partial_3 u_{x_0,M,\sigma} \\ (\sigma_1 - \sigma_3)\partial_1\partial_3 u_{x_0,M,\sigma} \\ (\sigma_2 - \sigma_1)\partial_1\partial_2 u_{x_0,M,\sigma} \end{pmatrix} \tag{6.19}$$

By Schwarz's theorem, we also have for all gradients and especially v, that $\nabla \times \nabla v = 0$. Since we required $\sigma_1 \neq \sigma_2$, we need $\partial_1 \partial_2 u_{x_0,M,\sigma}$ on $\mathbb{R}^3 \backslash \{x_0\}$ to be 0 to avoid a contradiction. Calculating the second partial derivatives from Equation (2.28) gives:

$$\partial_i \partial_j u^\infty(y) = \frac{3}{4\pi\sqrt{\det(\sigma)}} \frac{5x_i x_j \langle M, \sigma^{-1}x\rangle - (m_i x_j + m_j x_i)\langle \sigma^{-1}x, x\rangle}{\sigma_i \sigma_j \langle \sigma^{-1}x, x\rangle^{\frac{7}{2}}} \tag{6.20}$$

Hence, evaluating $\partial_1 \partial_2 u^\infty$ at $x := (1,0,0)^T$ yields:

$$\partial_1 \partial_2 u^\infty(x) = \frac{-3m_2 \sigma_1^{\frac{3}{2}}}{4\pi\sqrt{\det(\sigma)}\sigma_2} \tag{6.21}$$

This means that $\nabla \times \nabla v$ can only be always 0 for a general σ if $m_2 = 0$, but the dipole moment M was arbitrary, contradicting the existence of such a v. □

This lemma means that we cannot substitute in a ∇v for $\sigma^\infty \nabla u$ in (6.4), which would make the trick from the isotropic case applicable. Notably, $\sigma^\infty = c\mathrm{Id}_n$ for $c \in \mathbb{R}$ is a class for which this trick could still be applied, but for the important general diagonal matrices, the above proof shows that it does not work.

Malte Höltershinken has shown in [34] that the analytic integration formulas to assemble the linear system could be lifted up to anisotropic conductivity by the means of a simple linear transformation. To do so, he substituted in a linear transformation. In the following, it will be shown that this is not an option for this problem:

Lemma 25. *For $\sigma \in \mathbb{R}^{3\times 3}$ symmetric positive definite with $\sigma \neq Id_3$, $x_0, M \in \mathbb{R}^3$ and $u := u_{x_0,M,\sigma}$ defined by Equation (2.28), there is no diffeomorphism Φ and set $x_0 \in U$ such that the general change of variable theorem [36] may be used to achieve*

$$\int_U (\sigma \nabla u) \times \nabla d_s^{-1} dV = \int_{\Phi^{-1}(U)} [\nabla (u \circ \Phi)] \times \left[\nabla \left(d_s^{-1} \circ \Phi\right)\right] dV \tag{6.22}$$

Proof. Assuming the stated equality would hold, the change of variable theorem and the chain rule allow us to calculate:

$$\begin{aligned}\int_{\Phi^{-1}(U)} [\nabla (u \circ \Phi)] \times \nabla \left[\left(d_s^{-1} \circ \Phi\right)\right] dV &= \int_{\Phi^{-1}(U)} [\nabla\Phi\, (\nabla u) \circ \Phi] \times \left[\nabla\Phi \left(\nabla d_s^{-1}\right) \circ \Phi\right] dV \\ &= \int_U [\nabla\Phi \nabla u] \times \left[\nabla\Phi \nabla d_s^{-1}\right] dV\end{aligned} \tag{6.23}$$

To achieve $\sigma\nabla u = \nabla\Phi\nabla u$ would require $\nabla\Phi(x) = \sigma$ for all $x \in U$, meaning on U the diffeomorphism $\Phi(x)$ must be given by $\sigma^T \cdot x + b$ for some $b \in \mathbb{R}^3$ since σ is constant. But by the same argument for the right side of the cross product, we would require $\nabla\Phi = \mathrm{Id}_3$. Hence, $\sigma = \nabla\Phi = \mathrm{Id}_3$, which contradicts the requirement of $\sigma \neq \mathrm{Id}_3$. □

Lastly, it is shown that it is in general not possible to remove the matrix multiplication with σ from the cross product by matrix multiplication.

Lemma 26. *Given a symmetric positive definite matrix $M \in \mathbb{R}^{3\times3}$ and a matrix $L \in \mathbb{R}^{3\times3}$ such that for all $a, b \in \mathbb{R}^3$*

$$L \cdot (a \times b) = (Ma) \times b \tag{6.24}$$

then, $M = c \cdot Id_3$ for a $c \in \mathbb{R}$

Proof. As in the proof of Lemma 23, we can find a unitary matrix $O \in \mathbb{R}^{3\times3}$ and a diagonal matrix $D = \operatorname{diag}(d_1, d_2, d_3) \in \mathbb{R}^{3\times3}$ such that $\sigma = ODO^T$. Furthermore, we fix an $a \neq 0$ and since the cross product is anticommutative, $0 = L\,(a \times a)$. On the other hand, $(Ma) \times a = \left(ODO^T a\right) \times a$ multiplied with O^T, defining $b = O^T \cdot a$ and applying Lemma 21, we get:

$$0 = OL\,(a \times a) = O\left[(Ma) \times a\right] = O^T\left[\left(DO^T a\right) \times \left(O^T a\right)\right] = O^T\left[(Db) \times b\right] \tag{6.25}$$

Since O is invertible, this means:

$$0 = \begin{pmatrix} (d_2 - d_3)b_2b_3 \\ (d_3 - d_1)b_3b_1 \\ (d_1 - d_2)b_1b_2 \end{pmatrix} \tag{6.26}$$

Because we chose $b = O^T a$ arbitrarily, this means we have $d_1 = d_2 = d_3$, i.e., $D = c \cdot \mathrm{Id}_3$ for some $c \in \mathbb{R}$. But then we have already $M = O \cdot c \cdot \mathrm{Id}_3 \cdot O^T = c \cdot \mathrm{Id}_3$. □

The previous two lemmas exclude two broad categories of approaches to transform the anisotropic case back to the isotropic case. We cannot find a diffeomorphism that works in conjunction with the change of variable theorem to transform into the isotropic form, nor can there be an identity that allows extracting the conductivity matrix without additional terms from the cross product unless we are in the isotropic case. They, however, inspired a recursive procedure to remove the anisotropic tensor.

6.4. Idea: Recursive Decomposition of the Singular Anisotropic Integral

Lemma 22 provides a way to shift a symmetric matrix from one side of a cross product to the other, at the cost of additional cross products. Using that for a symmetric positive matrix M, we can compute a root, that is, a positive definite matrix $\sqrt{M}$ fulfilling $M = \sqrt{M}^2$. Then, given the term under the integral in Equation (6.4), we can rewrite it as:

$$\begin{aligned}\left[\sqrt{\sigma^\infty}\left(\sqrt{\sigma^\infty}\nabla u^\infty\right)\right] \times \nabla d_s^{-1} = \operatorname{tr}\left(\sqrt{\sigma^\infty}\right)\left(\left(\sqrt{\sigma^\infty}\nabla u^\infty\right) \times \nabla d_s^{-1}\right) \\ - \sqrt{\sigma^\infty}\left(\left(\sqrt{\sigma^\infty}\nabla u^\infty\right) \times \nabla d_s^{-1}\right) \\ - \left(\sqrt{\sigma^\infty}\nabla u^\infty\right) \times \left(\sqrt{\sigma^\infty}\nabla d_s^{-1}\right)\end{aligned} \tag{6.27}$$

First, note that with Lemma 21, we can transform the last term of (6.27) to:

$$\left(\sqrt{\sigma^\infty}\nabla u^\infty\right) \times \left(\sqrt{\sigma^\infty}\nabla d_s^{-1}\right) = \det(\sqrt{\sigma^\infty})\sqrt{\sigma^\infty}^{-1}\left(\nabla u^\infty \times \nabla d_s^{-1}\right) \tag{6.28}$$

Allowing integration of the last term using the trick from the isotropic case. Furthermore, noting that $\sqrt{\sigma^\infty}$ is again a symmetric positive definite matrix, we could apply the above again to $\left(\sqrt{\sigma^\infty}\nabla u^\infty\right) \times \nabla d_s^{-1}$ in the first and second term of (6.27), factoring out $(\sigma^\infty)^{\frac{1}{4}}$ and producing a recursive formula. Since $(\sigma^\infty)^{\frac{1}{2^N}} \to \mathrm{Id}_3$ for $N \to \infty$, the integrals get progressively closer to $\nabla u^\infty \times \nabla d_s^{-1}$, which could be integrated using the trick from the isotropic case. This could potentially be exploited numerically by recursively evaluating until $(\sigma^\infty)^{\frac{1}{N}}$ is sufficiently close to Id_3, at which point we would replace the integral with $\nabla u^\infty \times \nabla d_s^{-1}$. Since we are trying to integrate over a singularity, it is very much not clear if sufficiently close even exists in this case.

In any case, we may define:

$$\begin{aligned} R_n :&= \left(\sigma^{\frac{1}{2^n}}\nabla u^\infty\right) \times \nabla d_s^{-1} \\ &= \mathrm{tr}(\sigma^{\frac{1}{2^{n+1}}})R_{n+1} - \sigma^{\frac{1}{2^{n+1}}}R_{n+1} - \det(\sigma^{\frac{1}{2^{n+1}}})\left(\sigma^{\frac{1}{2^{n+1}}}\right)^{-1}\left(\nabla u^\infty \times \nabla d_s^{-1}\right) \end{aligned} \tag{6.29}$$

Which allows expanding the cross product out as in the following:

$$\begin{aligned} R_0 &= (\sigma^\infty \nabla u^\infty) \times \nabla d_s^{-1} \\ &= \mathrm{tr}(\sigma^{\frac{1}{2}})R_1 - \sigma^{\frac{1}{2}}R_1 - \det(\sigma^{\frac{1}{2}})\left(\sigma^{\frac{1}{2}}\right)^{-1}\left(\nabla u^\infty \times \nabla d_s^{-1}\right) \\ &= \mathrm{tr}(\sigma^{\frac{1}{2}})\left(\mathrm{tr}(\sigma^{\frac{1}{4}})R_2 - \sigma^{\frac{1}{4}}R_2 - \det(\sigma^{\frac{1}{4}})\left(\sigma^{\frac{1}{4}}\right)^{-1}\left(\nabla u^\infty \times \nabla d_s^{-1}\right)\right) \\ &\quad - \sigma^{\frac{1}{2}}\left(\mathrm{tr}(\sigma^{\frac{1}{4}})R_2 - \sigma^{\frac{1}{4}}R_2 - \det(\sigma^{\frac{1}{4}})\left(\sigma^{\frac{1}{4}}\right)^{-1}\left(\nabla u^\infty \times \nabla d_s^{-1}\right)\right) \\ &\quad - \det(\sigma^{\frac{1}{2}})\left(\sigma^{\frac{1}{2}}\right)^{-1}\left(\nabla u^\infty \times \nabla d_s^{-1}\right) \end{aligned} \tag{6.30}$$

In the numeric implementation, a fixed amount of expansions m is currently executed with $R_{m+1} := \frac{1}{3}\mathrm{tr}\left(\sigma^{\frac{1}{2^{m+1}}}\right)\nabla u^\infty \times \nabla d_s^{-1}$, which leads to a conforming formulation for isotropic σ.

6.5. Comparative Numerical Analysis of Singular Integration Methods

As proper results for Equation 6.4 have evaded us thus far, we want to conclude with a numerical investigation into the issues this integral causes.

Methods

Two four-layer sphere models sized as in Table 3.1 approximated by `mesh_mid` were set up. The first model used the isotropic premature infant conductivities from Table 3.1,

while the second one used a radial conductivity of $0.7763\frac{S}{m}$ with the premature infant anisotropy ratio of $5:1$ to avoid errors due to big conductivity jumps. We use the standard tangential dipole configuration from Section 3.5 along with a set of 256 coil positions[1] from [33]. Only tangential sources were considered since [55] has shown that radial sources do not produce any magnetic field outside of a spherically symmetric conductor.

Then, multiple forward simulations were performed using the Multipolar St. Venant source model and the Local Subtraction approach with different approximations of the Biot-Savart law around the singularity[2]:

- **Multipolar St. Venant:** The existing DUNEuro implementation for forward MEG simulations using St. Venant type approaches. Since these approaches only approximate the dipole and do not cause singularities in the approximate potential, one can directly apply the Biot-Savart law to compute the secondary field numerically.

- **Local Subtraction:** The Local Subtraction approach as implemented and described in [33]. Meaning the secondary magnetic field B^S is evaluated by the following that can be obtained by carefully splitting (6.2):

$$\begin{aligned} -\frac{4\pi}{\mu_0}B^S(s) = &\int_\Omega \sigma(y)\nabla u^c(y) \times \frac{s-y}{||s-y||^3}dV(y) \\ &+ \int_{\Omega^\infty} \sigma^c(y)\nabla u^\infty(y) \times \frac{s-y}{||s-y||^3}dV(y) \\ &+ \int_{\Omega^\infty} \sigma^\infty(y)\nabla u^\infty(y) \times \frac{s-y}{||s-y||^3}dS(y) \\ &+ \int_{\tilde{\Omega}} \sigma(y)\nabla\left(\chi \cdot u^\infty\right)(y) \times \frac{s-y}{||s-y||^3}dV(y) \end{aligned} \tag{6.31}$$

  To the third term on the RHS of this, the trick presented in Equation (6.5) is applied, assuming isotropic σ^∞, to transition to a boundary integral:

$$\begin{aligned} -\frac{4\pi}{\mu_0}B^S(s) = &\int_\Omega \sigma(y)\nabla u^c(y) \times \frac{s-y}{||s-y||^3}dV(y) \\ &+ \int_{\Omega^\infty} \sigma^c(y)\nabla u^\infty(y) \times \frac{s-y}{||s-y||^3}dV(y) \\ &+ \int_{\partial\Omega^\infty} \sigma^\infty(y)u^\infty(y)\cdot n(y) \times \frac{s-y}{||s-y||^3}dV(y) \\ &+ \int_{\tilde{\Omega}} \sigma(y)\nabla\left(\chi \cdot u^\infty\right)(y) \times \frac{s-y}{||s-y||^3}dV(y) \end{aligned} \tag{6.32}$$

[1] See: https://zenodo.org/records/12575552

[2] The implementation can be found at: https://gitlab.dune-project.org/timon.gronotte/thesis-experiments/-/tree/main/05_meg_zero_source_spheres_test

Hence, this approach can only be applied to isotropic conductivities and was added here for reference.

- **Local Subtraction Zero Epsilon Ball:** Here, we use the Local Subtraction approach to solve the EEG forward problem, but we define with radius $\epsilon > 0$ around the dipole location x_0 a ball $B_\epsilon(x_0) := \{x \in \mathbb{R}^3 | \ ||x - x_0|| < \epsilon\}$ and remove this set from the integration. This simply removes a small region around the singularity from the integration in the hope that its contribution would cancel due to the symmetry of u^∞. Hence, we used the following to compute the secondary magnetic field:

$$\begin{aligned} -\frac{4\pi}{\mu_0} B^S(s) \approx & \int_{\Omega \setminus B_\epsilon(x_0)} \sigma(y) \nabla u^c(y) \times \frac{s-y}{||s-y||^3} dV(y) \\ & + \int_{\Omega^\infty \setminus B_\epsilon(x_0)} \sigma(y) \nabla u^\infty(y) \times \frac{s-y}{||s-y||^3} dV(y) \\ & + \int_{\tilde{\Omega} \setminus B_\epsilon(x_0)} \sigma(y) \nabla \left(\chi \cdot u^\infty\right)(y) \times \frac{s-y}{||s-y||^3} dV(y) \end{aligned} \tag{6.33}$$

  Since it produces no RDM smaller than 0.25, it will not be shown in the plots.

- **Local Subtraction Recursive:** Here, we use the approach that has been described in Section 6.4. To build on existing implementations in DUNEuro, Equation (6.31) is used, where the term containing the singularity is replaced with 20 recursive expansions to approximate the integral over the singularity.

- **Local Subtraction Neglect Anisotropy:** Inspired by the Multipolar St. Venant approach, that does not change when the anisotropy is introduced, we use Equation (6.32). The equation is only true for isotropic conductivity, yet out of curiosity, the error that is produced if one simply inserts anisotropic σ and u^∞ was evaluated.

Analytic solutions to compare against were obtained from the work of Sarvas [55]. While that work assumes isotropic conductivity, the work of Ilmoniemi [38] shows that the anisotropy does not change the result in a sphere model.

Results

In Figure 6.1, we see the results from the isotropic test case. Here, we see nearly identical results for the recursive development and the pure Local Subtraction approach, which both yield better results than the St. Venant approach. Since the Local Subtraction Zero Epsilon Ball produced no RDM smaller than 0.25, it is not shown in this figure.

In Figure 6.2, we see the results from the anisotropic test case. They paint three quite different pictures. The St. Venant approach produces errors very close to the isotropic case. The Local Subtraction Neglect Anisotropy approach produces notably higher errors

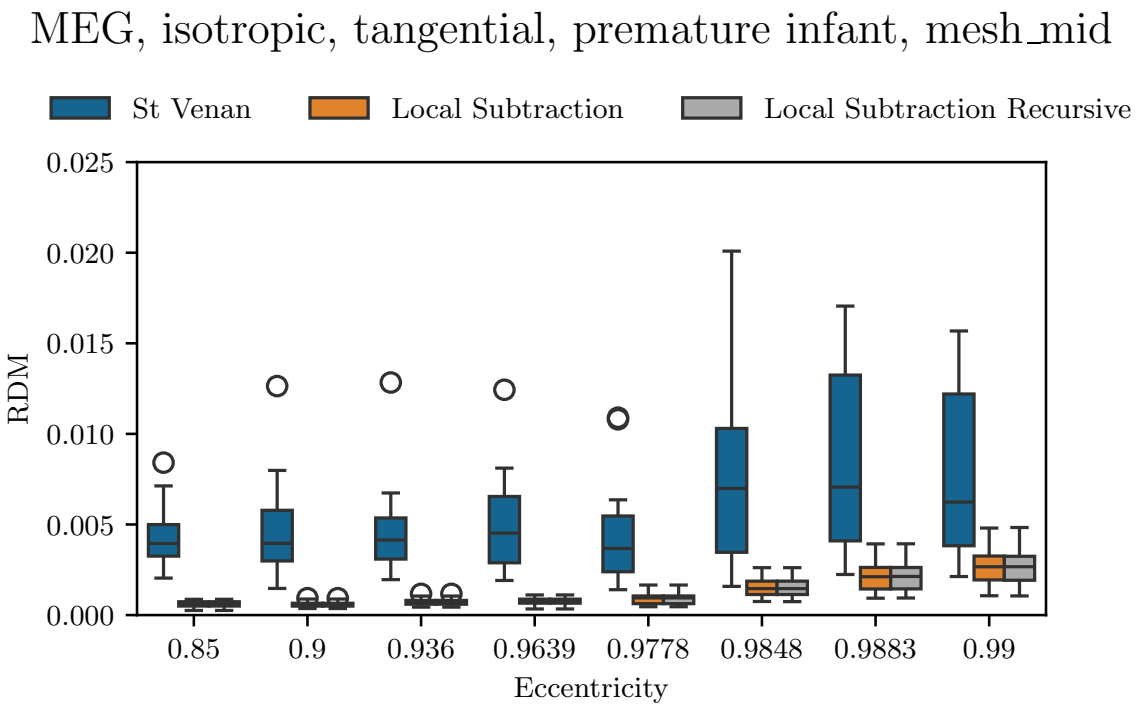

Figure 6.1.: Results from simulating 1000 tangential dipoles per eccentricity with isotropic conductivity. Some outliers of the St. Venant approach are not shown.

than the St. Venant approach, with a sharp increase in error and error range for eccentric sources. The Local Subtraction Recursive approach shows the highest RDM across all tested eccentricities, with a muted reaction to increases in eccentricity.

Discussion

The results for the isotropic case confirm the findings from the original Local Subtraction paper [33]. The Local Subtraction approach produced much better results than the St. Venant approach, especially for deep sources. Additionally, we see that the recursive expansion of the Local Subtraction approach produced indistinguishable data from the pure Local Subtraction approach. This is exactly the expected result, as the approach was designed to be equivalent to the Local Subtraction approach on isotropic compartments.

In the anisotropic case, we saw very good results for the St. Venant approach. Rather interestingly, the produced errors of this approach remained nearly unchanged when moving to the anisotropic model, while the underlying potential computation showed more than a doubling of RDM at the electrodes in Section 5.2.

This could potentially be explained by the nature of the Biot-Savart law. A contribution from a point y in the integration domain is penalized with the distance to the sensor position s by $||s-y||^{-3}$. This means that potential changes very close to the sensor have

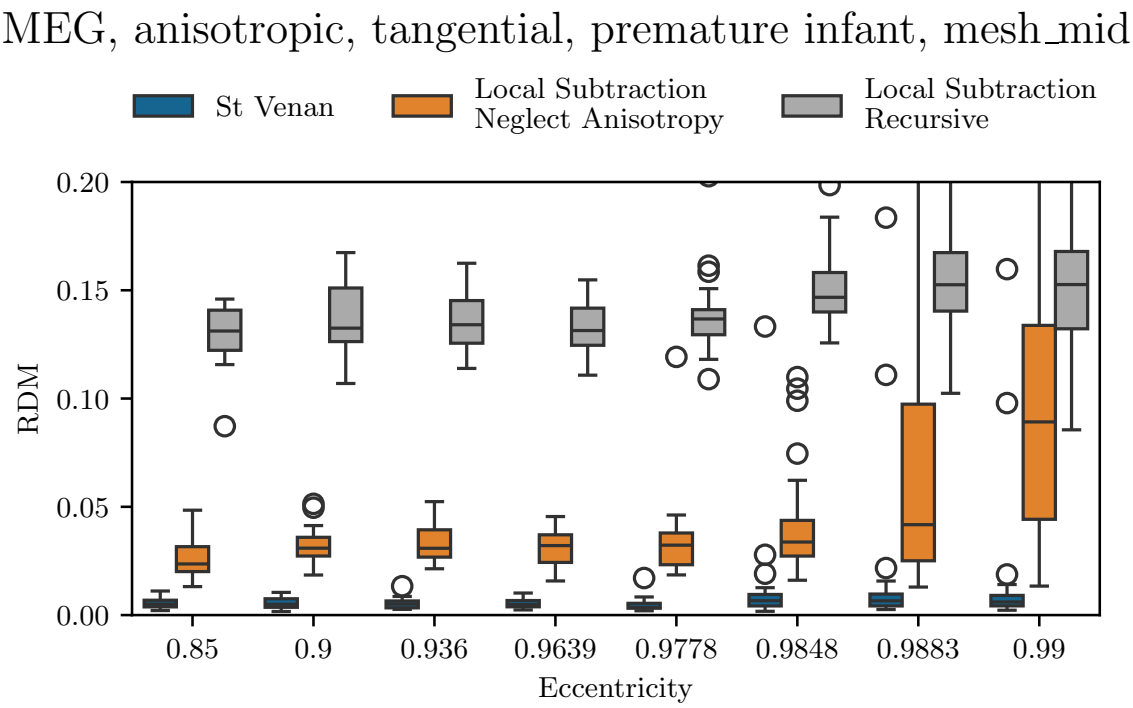

Figure 6.2.: Results from simulating 1000 tangential dipoles per eccentricity with anisotropic conductivity. Some outliers from all approaches are not shown.

a very big effect, while the effect of more distant points falls off very quickly. In our case, where there is no potential change in the vicinity of the sensor, all points with potential changes make heavily penalized contributions. On the other hand, the potential gradient approaches a very focused singularity at the dipole source, leading to very strong signals counteracting the penalization from the distance. This means there is a very small region around the dipole that will nearly completely determine the resulting field at the sensor.

The St. Venant approach, however, approximates the divergence of the primary current j^p around the dipole location with no regard for the present conductivity by fixing values on the RHS. When there is no change on the RHS, $\sigma \nabla u_h$ will be close to unchanged around the dipole although σ changed and the B-field simulation will be nearly unchanged as well, which would explain the observed errors.

The Local Subtraction Neglect Anisotropy approach has shown surprisingly good results. This is a futile result, however, since there is no theoretical backing for this approach, nor a large-scale simulation study. While its performance is interesting and might be in part a consequence of Ilmoniemi's results [38], the most interesting part is the contrast to the results from the Local Subtraction Recursive approach, which performed much worse in our test. It has shown a very consistent mean error over all eccentricities, suggesting that there might be a systemic error with this approach. While this could be

a bug in the implementation, this could also be the sign of the hubris of assuming that a conductivity close to the identity can be ignored close to the singularity.

Overall, it is currently recommended to use the Multipolar St. Venant approach for anisotropic MEG, based on this result. It by far outperformed both Local Subtraction variants in our test, which further lack any amount of theoretical backing.

7. Conclusion

7.1. Discussion

This thesis presented an investigation into the impact of gray matter conductivity anisotropy on EEG and MEG source estimation and an evaluation of the Local Subtraction approach.

Regarding the mesh dependence of the Local Subtraction approach, the findings from its original publication [33] were confirmed and extended by including the mesh resolution in the considerations. In [33], Höltershinken et al. noted the initial error decrease when increasing the patch size, coming from the vanishing need to approximate the potential near the singular source, as well as the error increase when the patch grows into the skin compartment. Besides confirming those findings for more eccentricities, it was shown through mesh refinement that those findings are linked to the distance from the source rather than the number of elements from the source. The originally recommended two vertex extensions are still a very good compromise of accuracy and computation time and the best choice for practically used meshes. If one does go to higher mesh resolutions, however, it is recommended to give the patch a radius of 10 mm for the best results.

The starting point of our anisotropic investigation was [21] from Drechsler et al., where they investigated EEG forward modeling approaches with conductivity anisotropy in the source space in four-layer sphere models. In that study, older types of the approaches, namely the St. Venant approach following Buchner et al. [12] and the original subtraction method by Wolters et al. [71], have been used. Both approaches have been improved upon since and hence we have used the Multipolar St. Venant approach by Vorwerk et al. [67] and the aforementioned Local Subtraction approach.

The original investigation restricted dipole sources to the barycenter of their finite element mesh due to the solution dependence on source placement relative to the mesh, citing the diploma thesis from Johannes Vorwerk [65]. In our own testing in the isotropic setting, we still found that the Local Subtraction approach performed best in the barycenter of elements and worst close to nodes and the opposite for the Multipolar St. Venant. However, we found that the average relative error of favorable and unfavorable positions was no bigger than 0.005, which we declared negligible for any practical concerns. In the anisotropic setting, we did find the same pattern but a more significant variation in mean and distribution width. When focusing on a single approach, restricting to

certain source positions will be helpful. For a fair comparison, we have chosen to use arbitrary source positions throughout this work.

To measure the effect of introducing anisotropy into the EEG forward problem, a meaningful relation between the isotropic conductivity value and the symmetric positive-definite 3×3 conductivity tensor was required to give meaning to a comparison between isotropic and anisotropic forward simulations. As in our template work [21], we chose to create this relation by optimizing the conductivity pairing to produce the least possible differences. To do so, a restriction to specific tensors was enacted. The included tensors have one predominant direction, i.e., an eigenvector with a comparatively large eigenvalue and two orthogonal eigenvectors with the same smaller eigenvalue (Definition 16), which allows us to compute analytic solutions in spherical head models. The restrictions determine the tensors up to a principal direction, a ratio between the eigenvalues and a single eigenvalue. Due to experimental results [31, 13, 39, 58], showing gray matter anisotropy in adult brains in the normal direction to the interface between gray matter and CSF, the principal direction of the tensors was fixed in this direction. Our reference work [21] also provided some maximum ratios between the eigenvalues for different ages. Hence, optimization was only required for a single eigenvalue per age to get a base for comparison.

The underlying work [21] already put this approach forward and optimized for dipoles of all orientations and in a range of eccentricities. As a source tangential to the predominant conductivity direction is expected to produce very different fields than an aligned one, it was found here that this limits the potential of the optimization. The effects of dipole depth and orientation, as well as the measure used to compare the computed potentials in spherical models, have been investigated further in this work. All three were found to have a significant impact. The smallest impact was found for a change in eccentricity and the error deemed acceptable for an isotropic approximation of an anisotropic compartment. Since this parameter is very much unknown in source estimation, the final optimization result was not controlled for this parameter.

As expected, the source orientation is of great impact, allowing a three to five times better approximation in relative error if the dipole orientation is known. Because of this, all following considerations were made under the assumption of a normal constraint, meaning the source orientation is always aligned with the principal direction of the conductivity tensor. While this constraint might not be realistic in a sphere model, this constraint is based on physiological reasoning [32].

The difference measure used for the optimization turned out to be of great importance itself. The relative error seems to be mainly controlled by the magnitude errors and the lnMAG reaches its optimum at significantly different conductivities than the RDM. This conductivity difference seemed, in turn, to be correlated with eccentricity. For this work, we focused on optimizing the RDM as it is considered the most important for source localization. Further, it was found to be the most practical, as the optima of

relative error and lnMAG were so small that our numeric approaches were pushed to their boundaries.

In general, the optima that were found are physiologically unfeasible. As the later discussed realistic head model investigations did yield more feasible results, we believe this is due to the chosen spherical model. As a four-layer sphere model was used, the entire innermost sphere was made anisotropic, which is physiologically quite different from a few millimeter thick gray matter layer. This unfortunate limitation is due to the available tools for the analytic solution, which currently support no more than four shells. As such, the produced approximations are only of philosophical interest and show that we can do the approximation in a probably harder case.

In our numerical testing on the sphere model, we were able to confirm and improve the results from our template paper [21]. We found that both anisotropic numeric approaches on realistically fine grids produce better approximations than even our improved isotropic approximations. Further, the relative error to analytic solutions is for anisotropic models about a magnitude worse compared to isotropic models and calculations.

It was confirmed in [33] that in isotropic settings, the Local Subtraction approach on reasonable meshes produces the best results. For the anisotropic case, it was shown that the ideal choice of approach is mesh-dependent. In a specific case, a classification of what approach to use when was possible but found to be erroneous after slight parameter changes. As such, it is recommended to do the quick forward calculations for both approaches for now, allowing cross-validation by two mathematically quite different approaches, yielding more substance to eventual findings.

To consider realistic head models, a six-compartment isotropic FEM head model was used. For anisotropic simulations, the tensors were added by reconstructing the boundary surfaces. The boundary tensors were then aligned with the surface normals and elements without a boundary intersection were assigned the tensor from the closest element on the border.

In this head model, the optimization procedure from the spherical models was repeated in restricted form using the Local Subtraction approach. Due to stability and importance for reconstruction, the RDM was chosen as a difference measure and because of the physiological reasoning, only sources aligned with the tensors were considered. When only considering the mean RDM, this procedure did yield a clear optimal conductivity pairing, within physiological reason. However, the RDM distribution over all considered sources resulted in a standard deviation of 50% of the achieved minimum and for the child model, this minimum was already no better than an RDM of 0.2. This illustrates either a significant effect when anisotropic gray matter is combined with complex head geometry or numerical difficulties when the latter yields too quickly changing conductivities.

To further investigate, the source space was restricted to a small region in the upper left hemisphere of the considered head model where tensors were visually checked to be reasonably placed. In this region, significant differences in potentials at the electrodes

were found between the Local Subtraction and Multipolar St. Venant approaches, in RDM as well as lnMAG. Further significant differences of similar magnitude were found when considering either approach on the realistic head model against itself on a regularly refined version of the realistic head model, pointing at insufficient convergence of both numeric approaches.

The effect that the inclusion of gray matter anisotropy has compared to isotropic head models was briefly considered as well. As seen in the spherical models, the lnMAG error was very significant, but besides the adult model, the RDM differences were bigger than expected. In a previous paper [66], Vorwerk et al. have analyzed the effects of adding in certain compartments against homogenization. Comparing with their results between model refinement steps for the lnMAG, the current effect of the adult model would be comparable to grid refinement, the child to including white matter anisotropy into an isotropic model and the premature infant could be as influential for lnMAG as the inclusion of a CSF compartment. Regarding RDM, for the adult, the effect lies between differentiating spongiosa and compacta in the skull and the inclusion of white matter anisotropy. The current result would mean that even the effect of child anisotropy would be more significant than modeling CSF. While the result for the adults seems reasonable, the effect for child and premature seem unreasonable considering previous questions regarding the results.

A further visual investigation focused on three specific source locations. This analysis demonstrated the potential benefit of modeling anisotropy and offered an intuitive explanation for the observed differences, particularly motivating the significant lnMAG values and small RDM differences found when comparing anisotropic and isotropic forward calculations. The investigation also visually highlighted the effect of local geometric curvature at the source location on the resulting electric potentials.

As the MEG is strongly connected to the potential close to the dipole over the Biot-Savart law, it was investigated as well. For the Local Subtraction approach, the singularity enters into these calculations, which has been solved for the isotropic case in the original paper [33]. While multiple approaches have been considered, it was only shown that certain approaches did not allow for the calculations to go through. Numeric considerations were limited to spherical head models where the Multipolar St. Venant performed well. A version of the Local Subtraction approach where the anisotropy was disregarded on the patch also performed well but was not further investigated due to a lack of mathematical motivation. Considering the difficulties with the EEG forward results in realistic head models on which the MEG forward problem depends, no MEG investigations on realistic head models were made.

7.2. Conclusion

It was found that in the isotropic case, the Local Subtraction approach performed better in all tested EEG cases than the Multipolar St. Venant approach on realistic or finer meshes and with a properly configured extension distance. Regardless of the approach, source placement relative to the grid is of little concern in the isotropic case.

In the anisotropic gray matter case for EEG, on a four-layer spherical model, it was found that both Local Subtraction and Multipolar St. Venant approaches on realistically resolved meshes were significantly better than isotropic estimation. However, at the tested mesh resolutions, the errors for anisotropic simulations in the child and premature conductivity sets were approximately an order of magnitude higher than those for the corresponding isotropic simulations. This finding suggests that the accurate modeling of anisotropy in these age groups requires significantly higher mesh resolutions.

On a realistic head model, it was then confirmed that the currently considered head models lack the gray matter resolution to consider gray matter anisotropy properly.

Regarding MEG, the St. Venant type appeared to perform similarly to the isotropic case in sphere models. Attempts to generalize the Local Subtraction approach for anisotropic source spaces were unfortunately not successful.

7.3. Outlook

Given that the current results were often limited by mesh resolution, a straightforward and immediate next step, provided sufficient computational resources, would be to explore significantly finer meshes. This would also allow the evaluation of a refined Multipole St. Venant formulation, that restricts the monopole moments further to guarantee the FEM has a unique solution. Furthermore, to enhance the realism of the spherical models, one could extend the current implementations of the analytic formulas to support more than four shells, allowing for separate gray and white matter compartments. The significant result noted regarding geometric curvature could also be further investigated by implementing the analytic ellipsoid solutions from De Munck [16].

The initial investigations used anisotropy tensors placed naively with a normal constraint. A deeper investigation into the optimal placement of these tensors, would be a valuable contribution to this field. Additionally, since the realistic head model considerations focused exclusively on adult geometry, it remains an open and important question how an actual premature infant head model geometry might affect these findings.

The field remains open for a mathematically robust solution for the MEG forward problem with anisotropic gray matter. Obtaining a solution that successfully generalizes the Local Subtraction approach would be a critical step in completing this model. Furthermore, the scope of this work did not extend to inverse approaches, leaving this as a highly promising and interesting line of research.

8. Bibliography

[1] James Ahrens, Berk Geveci, and Charles Law. "ParaView: An End-User Tool for Large-Data Visualization". en. In: *Visualization Handbook*. Elsevier, 2005, pp. 717–731. ISBN: 978-0-12-387582-2. DOI: 10.1016/B978-012387582-2/50038-1.

[2] Ümit Aydin et al. "Combining EEG and MEG for the Reconstruction of Epileptic Activity Using a Calibrated Realistic Volume Conductor Model". en. In: *PLoS ONE* 9.3 (Mar. 2014). Ed. by Gareth Robert Barnes. ISSN: 1932-6203. DOI: 10.1371/journal.pone.0093154.

[3] P.J. Basser, J. Mattiello, and D. Lebihan. "Estimation of the Effective Self-Diffusion Tensor from the NMR Spin Echo". en. In: *Journal of Magnetic Resonance, Series B* 103.3 (Mar. 1994), pp. 247–254. ISSN: 10641866. DOI: 10.1006/jmrb.1994.1037.

[4] P. Bastian et al. "A generic grid interface for parallel and adaptive scientific computing. Part I: abstract framework". en. In: *Computing* 82.2-3 (July 2008), pp. 103–119. ISSN: 0010-485X, 1436-5057. DOI: 10.1007/s00607-008-0003-x.

[5] P. Bastian et al. "A generic grid interface for parallel and adaptive scientific computing. Part II: implementation and tests in DUNE". en. In: *Computing* 82.2-3 (July 2008), pp. 121–138. ISSN: 0010-485X, 1436-5057. DOI: 10.1007/s00607-008-0004-9.

[6] Peter Bastian et al. "The Dune framework: Basic concepts and recent developments". en. In: *Computers & Mathematics with Applications* 81 (Jan. 2021), pp. 75–112. ISSN: 08981221. DOI: 10.1016/j.camwa.2020.06.007.

[7] Martin Bauer et al. "Comparison Study for Whitney (Raviart–Thomas)-Type Source Models in Finite-Element-Method-Based EEG Forward Modeling". In: *IEEE Transactions on Biomedical Engineering* 62.11 (Nov. 2015), pp. 2648–2656. ISSN: 0018-9294, 1558-2531. DOI: 10.1109/TBME.2015.2439282.

[8] Leandro Beltrachini. "The analytical subtraction approach for solving the forward problem in EEG". In: *Journal of Neural Engineering* 16.5 (Sept. 2019). Number: 5, p. 056029. ISSN: 1741-2552. DOI: 10.1088/1741-2552/ab2694.

[9] Markus Blatt and Peter Bastian. "The Iterative Solver Template Library". en. In: *Applied Parallel Computing. State of the Art in Scientific Computing*. Ed. by Bo Kågström et al. Vol. 4699. Series Title: Lecture Notes in Computer Science. Berlin, Heidelberg: Springer Berlin Heidelberg, 2007, pp. 666–675. ISBN: 978-3-540-75754-2. DOI: 10.1007/978-3-540-75755-9_82.

[10] Markus Blatt and Peter Bastian. "On the generic parallelisation of iterative solvers for the finite element method". en. In: *International Journal of Computational Science and Engineering* 4.1 (2008), p. 56. ISSN: 1742-7185, 1742-7193. DOI: 10.1504/IJCSE.2008.021112.

[11] R. P. Brent. *Algorithms for minimization without derivatives*. Prentice-Hall series in automatic computation. Englewood Cliffs, N.J: Prentice-Hall, 1972. ISBN: 978-0-13-022335-7. URL: https://katalogplus.uni-muenster.de/permalink/49HBZ_ULM/1orud0a/alma991004344119706449.

[12] Helmut Buchner et al. "Inverse localization of electric dipole current sources in finite element models of the human head". en. In: *Electroencephalography and Clinical Neurophysiology* 102.4 (Apr. 1997), pp. 267–278. ISSN: 00134694. DOI: 10.1016/S0013-4694(96)95698-9.

[13] J. Cohen-Adad et al. "T2* mapping and B0 orientation-dependence at 7T reveal cyto- and myeloarchitecture organization of the human cortex". en. In: *NeuroImage* 60.2 (Apr. 2012), pp. 1006–1014. ISSN: 10538119. DOI: 10.1016/j.neuroimage.2012.01.053.

[14] Moritz Dannhauer et al. "Modeling of the human skull in EEG source analysis". en. In: *Human Brain Mapping* 32.9 (Sept. 2011), pp. 1383–1399. ISSN: 1065-9471, 1097-0193. DOI: 10.1002/hbm.21114.

[15] GEORGE DASSIOS and FOTINI KARIOTOU. "ON THE GESELOWITZ FORMULA IN BIOMAGNETICS". In: *Quarterly of Applied Mathematics* 61.2 (2003). Publisher: Brown University, pp. 387–400. ISSN: 0033569X, 15524485. URL: http://www.jstor.org/stable/43638539.

[16] J. C. De Munck. "The potential distribution in a layered anisotropic spheroidal volume conductor". en. In: *Journal of Applied Physics* 64.2 (July 1988), pp. 464–470. ISSN: 0021-8979, 1089-7550. DOI: 10.1063/1.341983.

[17] J.C. De Munck and M.J. Peters. "A fast method to compute the potential in the multisphere model (EEG application)". In: *IEEE Transactions on Biomedical Engineering* 40.11 (Nov. 1993), pp. 1166–1174. ISSN: 00189294. DOI: 10.1109/10.245635.

[18] J.C. De Munck, B.W. Van Dijk, and H. Spekreijse. "Mathematical dipoles are adequate to describe realistic generators of human brain activity". In: *IEEE Transactions on Biomedical Engineering* 35.11 (Nov. 1988), pp. 960–966. ISSN: 00189294. DOI: 10.1109/10.8677.

[19] Jan C. De Munck, Carsten H. Wolters, and Maureen Clerc. "EEG and MEG: forward modeling". In: *Handbook of Neural Activity Measurement*. Ed. by Romain Brette and Alain Destexhe. 1st ed. Cambridge University Press, Sept. 2012, pp. 192–256. ISBN: 978-0-521-51622-8 978-0-511-97995-8. DOI: 10.1017/CBO9780511979958.006.

[20] Katharina Domschke et al. "Magnetoencephalographic Correlates of Emotional Processing in Major Depression Before and After Pharmacological Treatment". en. In: *International Journal of Neuropsychopharmacology* 19.2 (Feb. 2016), pyv093. ISSN: 1461-1457, 1469-5111. DOI: 10.1093/ijnp/pyv093.

[21] Florian Drechsler et al. "Validation of EEG forward modeling approaches in the presence of anisotropy in the source space". In: (Aug. 2022). Issue: arXiv:2208.03081 arXiv:2208.03081 [physics]. DOI: 10.48550/arXiv.2208.03081.

[22] Otto Forster. *Analysis 3: Maß- und Integrationstheorie, Integralsätze im IRn und Anwendungen*. ger. 8. Aufl. 2017. Aufbaukurs Mathematik. Wiesbaden: Springer Spektrum, 2017. ISBN: 978-3-658-16746-2. DOI: 10.1007/978-3-658-16746-2.

[23] Christophe Geuzaine and Jean-François Remacle. "Gmsh: A 3-D finite element mesh generator with built-in pre- and post-processing facilities". en. In: *International Journal for Numerical Methods in Engineering* 79.11 (Sept. 2009), pp. 1309–1331. ISSN: 0029-5981, 1097-0207. DOI: 10.1002/nme.2579.

[24] Christophe Geuzaine and Jean-François Remacle. "Gmsh: A 3-D finite element mesh generator with built-in pre- and post-processing facilities". en. In: *International Journal for Numerical Methods in Engineering* 79.11 (Sept. 2009), pp. 1309–1331. ISSN: 0029-5981, 1097-0207. DOI: 10.1002/nme.2579.

[25] Álvaro González. "Measurement of Areas on a Sphere Using Fibonacci and Latitude–Longitude Lattices". en. In: *Mathematical Geosciences* 42.1 (Jan. 2010), pp. 49–64. ISSN: 1874-8961, 1874-8953. DOI: 10.1007/s11004-009-9257-x.

[26] Daniel Güllmar, Jens Haueisen, and Jürgen R. Reichenbach. "Influence of anisotropic electrical conductivity in white matter tissue on the EEG/MEG forward and inverse solution. A high-resolution whole head simulation study". en. In: *NeuroImage* 51.1 (May 2010), pp. 145–163. ISSN: 10538119. DOI: 10.1016/j.neuroimage.2010.02.014.

[27] Hans Hallez et al. “Dipole estimation errors due to differences in modeling anisotropic conductivities in realistic head models for EEG source analysis”. In: *Physics in Medicine and Biology* 53.7 (Apr. 2008), pp. 1877–1894. ISSN: 0031-9155, 1361-6560. DOI: 10.1088/0031-9155/53/7/005.

[28] Matti Hämäläinen et al. “Magnetoencephalography—theory, instrumentation, and applications to noninvasive studies of the working human brain”. en. In: *Reviews of Modern Physics* 65.2 (Apr. 1993), pp. 413–497. ISSN: 0034-6861, 1539-0756. DOI: 10.1103/RevModPhys.65.413.

[29] Charles R. Harris et al. “Array programming with NumPy”. en. In: *Nature* 585.7825 (Sept. 2020), pp. 357–362. ISSN: 0028-0836, 1476-4687. DOI: 10.1038/s41586-020-2649-2.

[30] J. Haueisen et al. “The Influence of Brain Tissue Anisotropy on Human EEG and MEG”. en. In: *NeuroImage* 15.1 (Jan. 2002), pp. 159–166. ISSN: 10538119. DOI: 10.1006/nimg.2001.0962.

[31] Robin M. Heidemann et al. “Diffusion imaging in humans at 7T using readout-segmented EPI and GRAPPA”. en. In: *Magnetic Resonance in Medicine* 64.1 (July 2010), pp. 9–14. ISSN: 0740-3194, 1522-2594. DOI: 10.1002/mrm.22480.

[32] A Hillebrand. “The use of anatomical constraints with MEG beamformers”. en. In: *NeuroImage* 20.4 (Dec. 2003), pp. 2302–2313. ISSN: 10538119. DOI: 10.1016/j.neuroimage.2003.07.031.

[33] Malte B. Höltershinken et al. “The Local Subtraction Approach for EEG and MEG Forward Modeling”. en. In: *SIAM Journal on Scientific Computing* 47.1 (Feb. 2025). Number: 1, B160–B189. ISSN: 1064-8275, 1095-7197. DOI: 10.1137/23M1582874.

[34] Malte Bernhard Höltershinken. “New mathematics for the EEG and MEG forward and inverse problems, and application to the tDCS stimulation of an epilepsy patient”. PhD thesis, officially submitted for defense. PHD Thesis. IBB: Münster. URL: https://www.sci.utah.edu/~wolters/PaperWolters/2025/Hoeltershinken_Dissertation.pdf.

[35] Roger A. Horn and Charles R. Johnson. *Matrix Analysis:* 2nd ed. Cambridge University Press, Oct. 2012. ISBN: 978-0-521-83940-2 978-1-139-02041-1 978-0-521-54823-6. DOI: 10.1017/CBO9781139020411.

[36] John H. Hubbard and Barbara Burke Hubbard. *Vector calculus, linear algebra, and differential forms: a unified approach.* eng. Upper Saddle River, NJ: Prentice Hall, 1999. ISBN: 978-0-13-657446-0. URL: https://hal.science/hal-01297648.

[37] John D. Hunter. “Matplotlib: A 2D Graphics Environment”. In: *Computing in Science & Engineering* 9.3 (2007), pp. 90–95. ISSN: 1521-9615. DOI: 10.1109/MCSE.2007.55.

[38] R. J Ilmoniemi. "Radial Anisotropy Added to a Spherically Symmetric Conductor Does Not Affect the External Magnetic Field Due to Internal Sources". In: *Europhysics Letters (EPL)* 30.5 (May 1995), pp. 313–316. ISSN: 0295-5075, 1286-4854. DOI: 10.1209/0295-5075/30/5/011.

[39] Derek K. Jones, ed. *Diffusion MRI: theory, methods, and application*. Oxford ; New York: Oxford University Press, 2010. ISBN: 978-0-19-536977-9. URL: https://katalogplus.uni-muenster.de/permalink/49HBZ_ULM/1qrskqt/cdi_nii_cinii_1130282268960671360.

[40] Fatih Karpuz. "The Complete Electrode Model in Bioelectromagnetism: Analysis, Implementation and Evaluation". MA thesis. Universität Münster, 2025. URL: https://www.sci.utah.edu/~wolters/PaperWolters/2025/Karpuz_Master.pdf.

[41] S. Lew et al. "Accuracy and run-time comparison for different potential approaches and iterative solvers in finite element method based EEG source analysis". en. In: *Applied Numerical Mathematics* 59.8 (Aug. 2009), pp. 1970–1988. ISSN: 01689274. DOI: 10.1016/j.apnum.2009.02.006.

[42] Fa-Hsuan Lin et al. "Distributed current estimates using cortical orientation constraints". In: *Human Brain Mapping* 27.1 (2006), pp. 1–13. DOI: https://doi.org/10.1002/hbm.20155. eprint: https://onlinelibrary.wiley.com/doi/pdf/10.1002/hbm.20155.

[43] Felix Lucka et al. "Hierarchical Bayesian inference for the EEG inverse problem using realistic FE head models: Depth localization and source separation for focal primary currents". en. In: *NeuroImage* 61.4 (July 2012), pp. 1364–1382. ISSN: 10538119. DOI: 10.1016/j.neuroimage.2012.04.017.

[44] Jaakko Malmivuo and Robert Plonsey. *BioelectromagnetismPrinciples and Applications of Bioelectric and Biomagnetic Fields*. Oxford University Press, Oct. 1995. ISBN: 978-0-19-505823-9. DOI: 10.1093/acprof:oso/9780195058239.001.0001.

[45] Wes McKinney. "Data Structures for Statistical Computing in Python". In: *Proceedings of the 9th Python in Science Conference*. Ed. by Stéfan van der Walt and Jarrod Millman. 2010, pp. 56–61. DOI: 10.25080/Majora-92bf1922-00a.

[46] J.W.H. Meijs et al. "On the numerical accuracy of the boundary element method (EEG application)". In: *IEEE Transactions on Biomedical Engineering* 36.10 (Oct. 1989), pp. 1038–1049. ISSN: 00189294. DOI: 10.1109/10.40805.

[47] Tuuli Miinalainen et al. "A realistic, accurate and fast source modeling approach for the EEG forward problem". en. In: *NeuroImage* 184 (Jan. 2019), pp. 56–67. ISSN: 10538119. DOI: 10.1016/j.neuroimage.2018.08.054.

[48] J.C. Mosher, R.M. Leahy, and P.S. Lewis. "EEG and MEG: forward solutions for inverse methods". In: *IEEE Transactions on Biomedical Engineering* 46.3 (Mar. 1999), pp. 245–259. ISSN: 00189294. DOI: 10.1109/10.748978.

[49] J J Neil et al. "Normal brain in human newborns: apparent diffusion coefficient and diffusion anisotropy measured by using diffusion tensor MR imaging." en. In: *Radiology* 209.1 (Oct. 1998), pp. 57–66. ISSN: 0033-8419, 1527-1315. DOI: 10.1148/radiology.209.1.9769812.

[50] J. Neil et al. "Diffusion tensor imaging of normal and injured developing human brain - a technical review". en. In: *NMR in Biomedicine* 15.7-8 (Nov. 2002), pp. 543–552. ISSN: 0952-3480, 1099-1492. DOI: 10.1002/nbm.784.

[51] Frank Neugebauer et al. "Validating EEG, MEG and Combined MEG and EEG Beamforming for an Estimation of the Epileptogenic Zone in Focal Cortical Dysplasia". en. In: *Brain Sciences* 12.1 (Jan. 2022), p. 114. ISSN: 2076-3425. DOI: 10.3390/brainsci12010114.

[52] S Pursiainen, F Lucka, and C H Wolters. "Complete electrode model in EEG: relationship and differences to the point electrode model". In: *Physics in Medicine and Biology* 57.4 (Feb. 2012), pp. 999–1017. ISSN: 0031-9155, 1361-6560. DOI: 10.1088/0031-9155/57/4/999.

[53] K. F. Riley, M. P. Hobson, and S. J. Bence. *Mathematical Methods for Physics and Engineering*. 3rd ed. Cambridge: Cambridge University Press, 2006. ISBN: 978-0-511-81076-3. DOI: 10.1017/CBO9780511810763.

[54] Oliver Sander. *DUNE — The Distributed and Unified Numerics Environment*. en. Vol. 140. Lecture Notes in Computational Science and Engineering. Cham: Springer International Publishing, 2020. ISBN: 978-3-030-59701-6 978-3-030-59702-3. DOI: 10.1007/978-3-030-59702-3.

[55] J Sarvas. "Basic mathematical and electromagnetic concepts of the biomagnetic inverse problem". In: *Physics in Medicine and Biology* 32.1 (Jan. 1987). Number: 1, pp. 11–22. ISSN: 0031-9155, 1361-6560. DOI: 10.1088/0031-9155/32/1/004.

[56] Jan-Mathijs Schoffelen and Joachim Gross. "Source connectivity analysis with MEG and EEG". en. In: *Human Brain Mapping* 30.6 (June 2009), pp. 1857–1865. ISSN: 1065-9471, 1097-0193. DOI: 10.1002/hbm.20745.

[57] Sophie Schrader et al. "DUNEuro—A software toolbox for forward modeling in bioelectromagnetism". en. In: *PLOS ONE* 16.6 (June 2021). Ed. by Christos Papadelis. Number: 6, e0252431. ISSN: 1932-6203. DOI: 10.1371/journal.pone.0252431.

[58] Joshua S. Shimony et al. "Quantitative Diffusion-Tensor Anisotropy Brain MR Imaging: Normative Human Data and Anatomic Analysis". en. In: *Radiology* 212.3 (Sept. 1999), pp. 770–784. ISSN: 0033-8419, 1527-1315. DOI: 10.1148/radiology.212.3.r99au51770.

[59] SimBio Development Group. *SimBio: A generic environment for bio-numerical simulations*. 2025. URL: https://www.mrt.uni-jena.de/simbio.

[60] The pandas development team. *pandas-dev/pandas: Pandas*. Feb. 2020. DOI: 10.5281/zenodo.3509134.

[61] Brandon J. Thio et al. "Ideal current dipoles are appropriate source representations for simulating neurons for intracranial recordings". en. In: *Clinical Neurophysiology* 145 (Jan. 2023), pp. 26–35. ISSN: 13882457. DOI: 10.1016/j.clinph.2022.11.002.

[62] David S. Tuch et al. "Conductivity tensor mapping of the human brain using diffusion tensor MRI". en. In: *Proceedings of the National Academy of Sciences* 98.20 (Sept. 2001), pp. 11697–11701. ISSN: 0027-8424, 1091-6490. DOI: 10.1073/pnas.171473898.

[63] Sylvain Vallaghé and Théodore Papadopoulo. "A Trilinear Immersed Finite Element Method for Solving the Electroencephalography Forward Problem". en. In: *SIAM Journal on Scientific Computing* 32.4 (Jan. 2010), pp. 2379–2394. ISSN: 1064-8275, 1095-7197. DOI: 10.1137/09075038X.

[64] Pauli Virtanen et al. "SciPy 1.0: fundamental algorithms for scientific computing in Python". en. In: *Nature Methods* 17.3 (Mar. 2020), pp. 261–272. ISSN: 1548-7091, 1548-7105. DOI: 10.1038/s41592-019-0686-2.

[65] Johannes Vorwerk. "Comparison of Numerical Approaches to the EEG Forward Problem". Diploma. Münster, Dec. 2011. URL: https://www.sci.utah.edu/~wolters/PaperWolters/2011/VorwerkDiplom.pdf.

[66] Johannes Vorwerk et al. "A guideline for head volume conductor modeling in EEG and MEG". en. In: *NeuroImage* 100 (Oct. 2014), pp. 590–607. ISSN: 10538119. DOI: 10.1016/j.neuroimage.2014.06.040.

[67] Johannes Vorwerk et al. "The multipole approach for EEG forward modeling using the finite element method". en. In: *NeuroImage* 201 (Nov. 2019), p. 116039. ISSN: 10538119. DOI: 10.1016/j.neuroimage.2019.116039.

[68] Kun Wang et al. "A New Method to Derive White Matter Conductivity From Diffusion Tensor MRI". In: *IEEE Transactions on Biomedical Engineering* 55.10 (Oct. 2008), pp. 2481–2486. ISSN: 0018-9294, 1558-2531. DOI: 10.1109/TBME.2008.923159.

[69] Jörg Wellmer et al. “Lesion guided stereotactic radiofrequency thermocoagulation for palliative, in selected cases curative epilepsy surgery”. en. In: *Epilepsy Research* 121 (Mar. 2016), pp. 39–46. ISSN: 09201211. DOI: 10.1016/j.eplepsyres.2016.01.005.

[70] C H Wolters, L Grasedyck, and W Hackbusch. “Efficient computation of lead field bases and influence matrix for the FEM-based EEG and MEG inverse problem”. In: *Inverse Problems* 20.4 (Aug. 2004), pp. 1099–1116. ISSN: 0266-5611, 1361-6420. DOI: 10.1088/0266-5611/20/4/007.

[71] C. H. Wolters et al. “Numerical Mathematics of the Subtraction Method for the Modeling of a Current Dipole in EEG Source Reconstruction Using Finite Element Head Models”. en. In: *SIAM Journal on Scientific Computing* 30.1 (Jan. 2008). Publisher: Society for Industrial & Applied Mathematics (SIAM), pp. 24–45. ISSN: 1064-8275, 1095-7197. DOI: 10.1137/060659053.

[72] C.H. Wolters et al. “Influence of tissue conductivity anisotropy on EEG/MEG field and return current computation in a realistic head model: A simulation and visualization study using high-resolution finite element modeling”. en. In: *NeuroImage* 30.3 (Apr. 2006), pp. 813–826. ISSN: 10538119. DOI: 10.1016/j.neuroimage.2005.10.014.

[73] C.H. Wolters et al. “Influence of tissue conductivity anisotropy on EEG/MEG field and return current computation in a realistic head model: A simulation and visualization study using high-resolution finite element modeling”. en. In: *NeuroImage* 30.3 (Apr. 2006). Publisher: Elsevier BV, pp. 813–826. ISSN: 1053-8119. DOI: 10.1016/j.neuroimage.2005.10.014.

[74] Carsten Wolters et al. “Influence of local and remote white matter conductivity anisotropy for a thalamic source on EEG/MEG field and return current computation”. In: *International Journal of Bioelectromagnetism* 7 (June 2005), pp. 203–206. URL: https://hdl.handle.net/11858/00-001M-0000-0010-BD0B-E.

A. Additional Figures

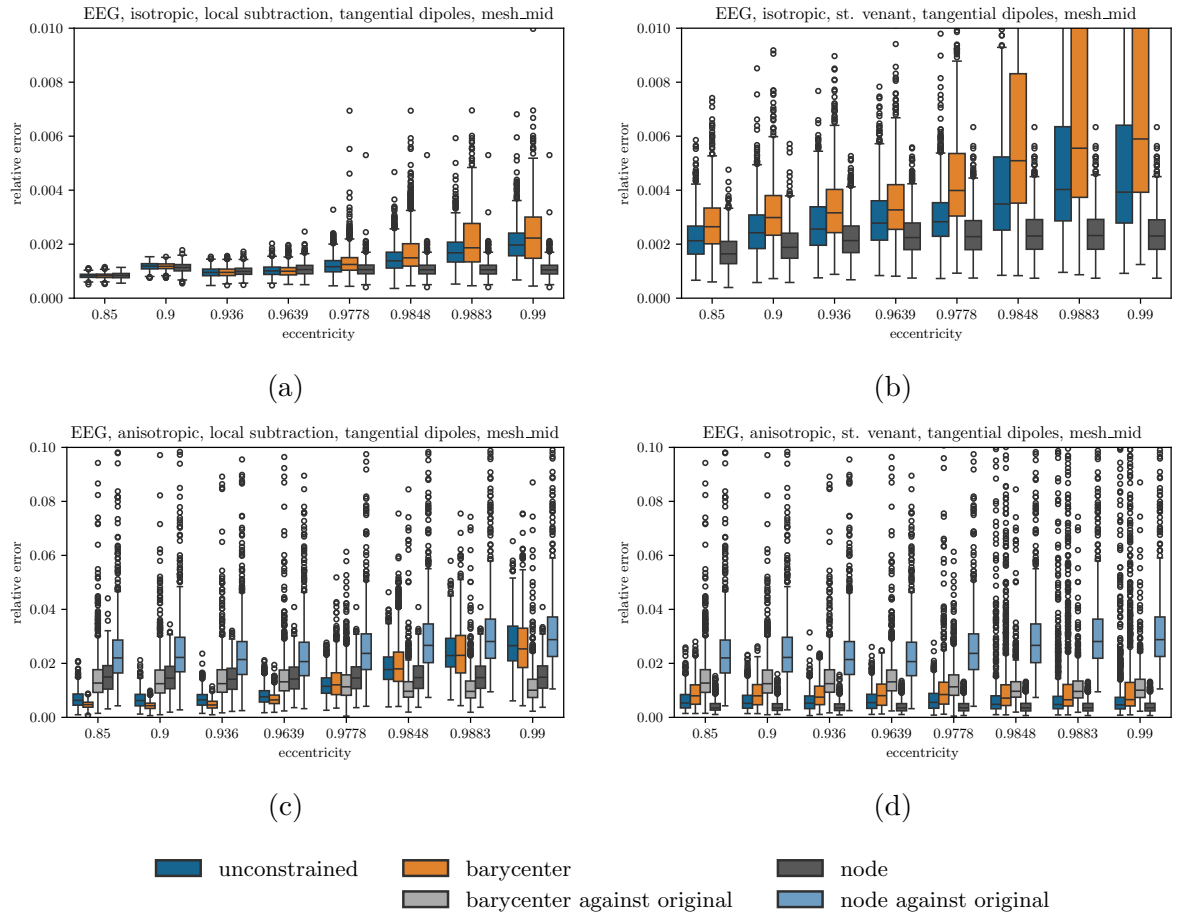

Figure A.1.: Relative error for different dipole positioning schemes in the EEG case, for 1000 tangential dipoles at different eccentricities. (a) shows the results in an isotropic volume conductor using a Local Subtraction approach, (b) shows the same for a St. Venant approach. (c) shows the results in an anisotropic volume conductor with a 5:1 ratio using a Local Subtraction approach, (d) shows the same for a St. Venant approach. The anisotropic plots also show the relative error against the analytic solution at the original dipole location.

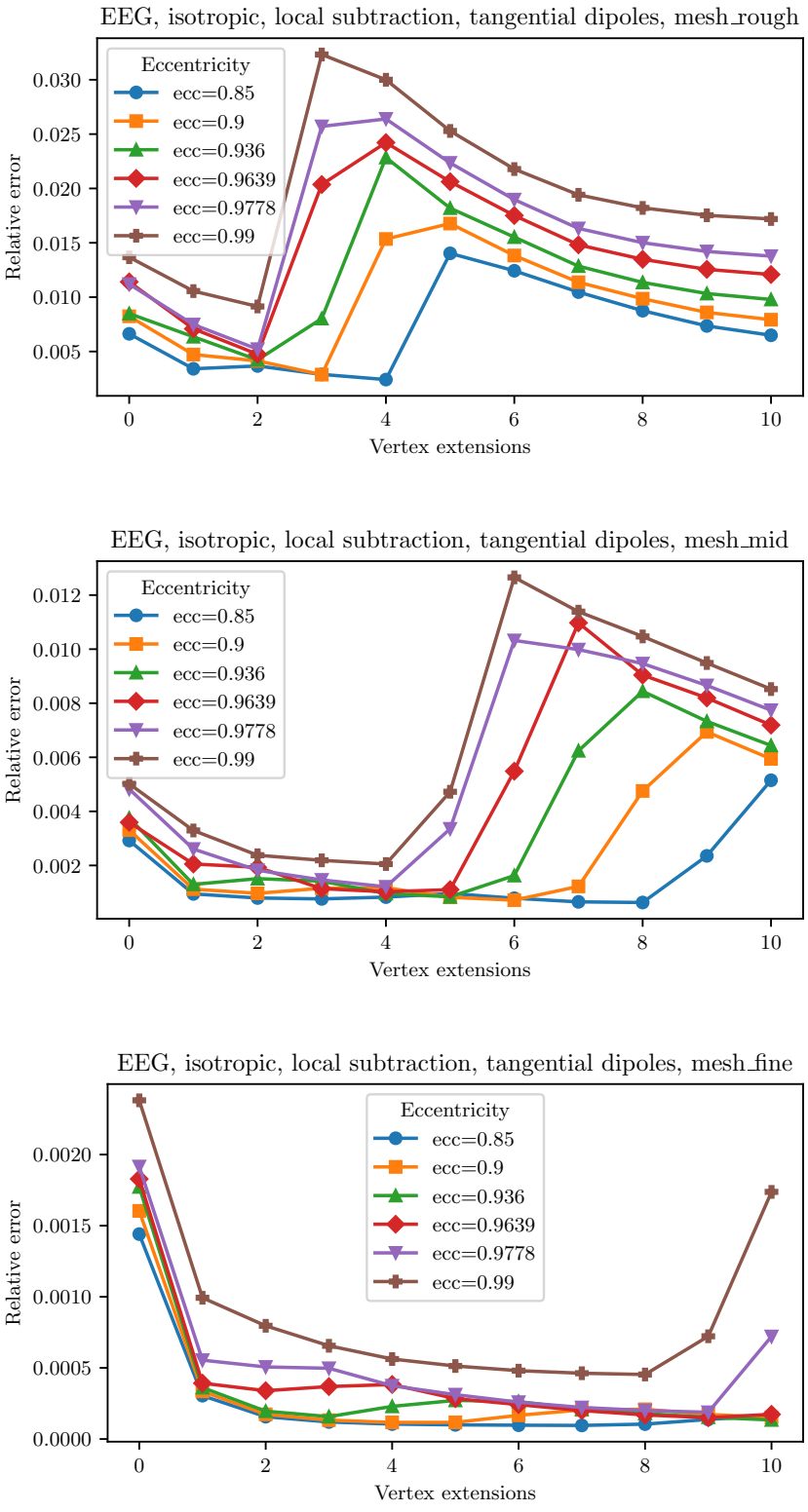

Figure A.2.: Plots showing EEG mean relative error for 1000 radial dipoles at different eccentricities and vertex extensions, without error ranges. Sown are the results on `rough_mesh`, `mid_mesh` and `fine_mesh`.

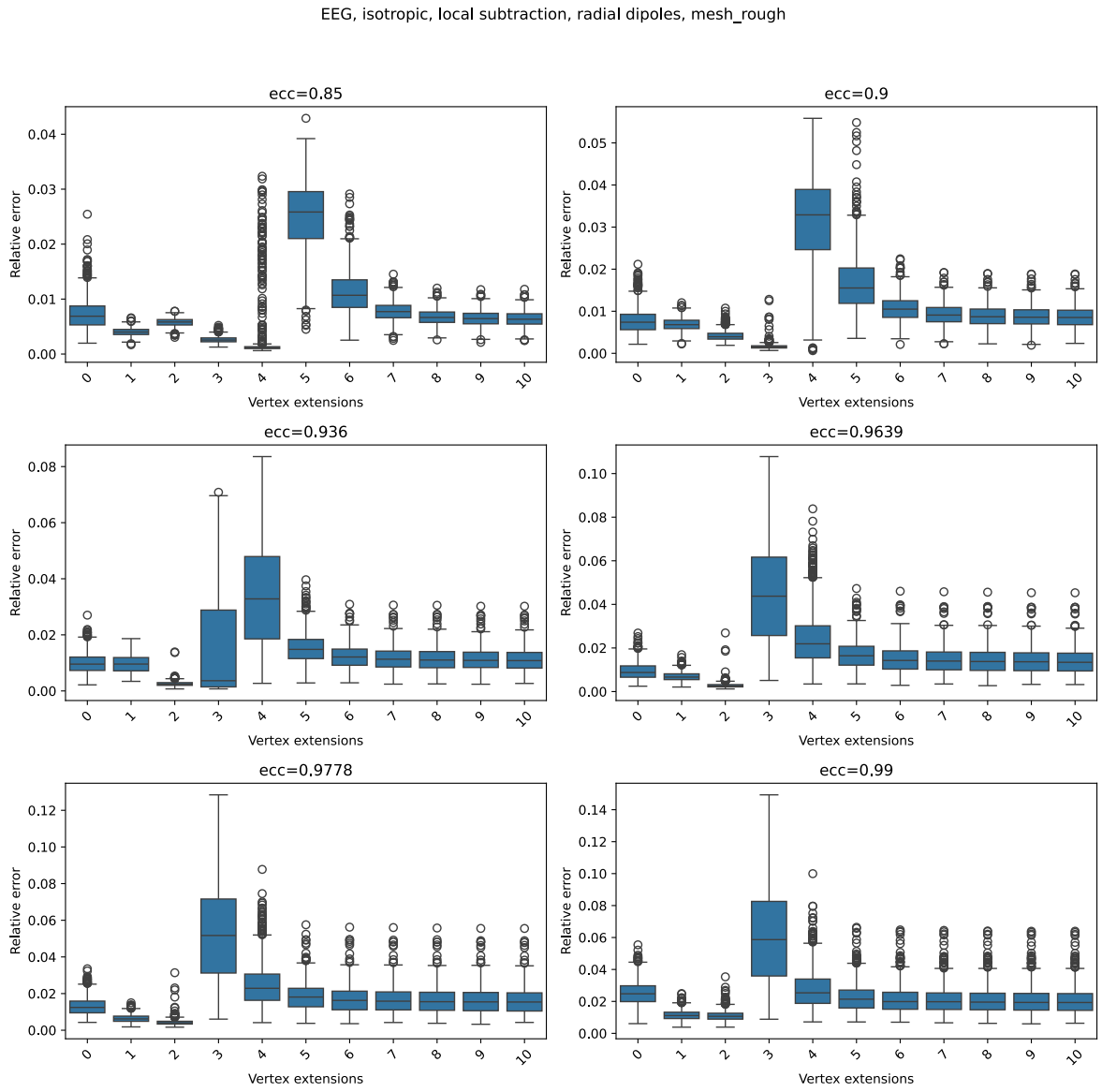

Figure A.3.: Plots showing the relative error of simulating 1000 radial dipoles on `mesh_rough` for different levels of vertex extensions. Thereby ecc is the source depth of the dipoles, given as a fraction of the total brain radius.

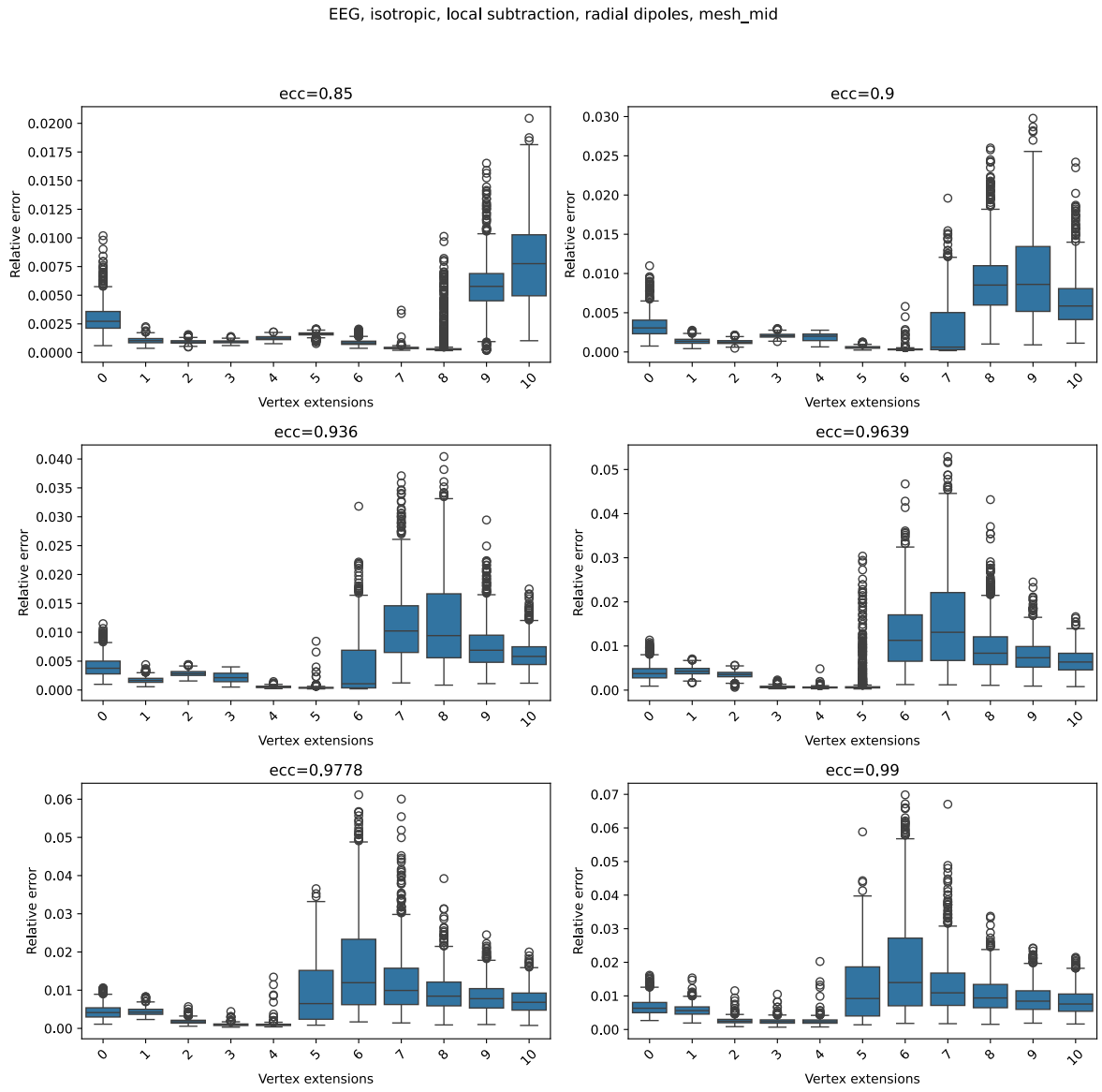

Figure A.4.: Plots showing the relative error of simulating 1000 radial dipoles on `mesh_mid` for different levels of vertex extensions. Thereby ecc is the source depth of the dipoles, given as a fraction of the total brain radius.

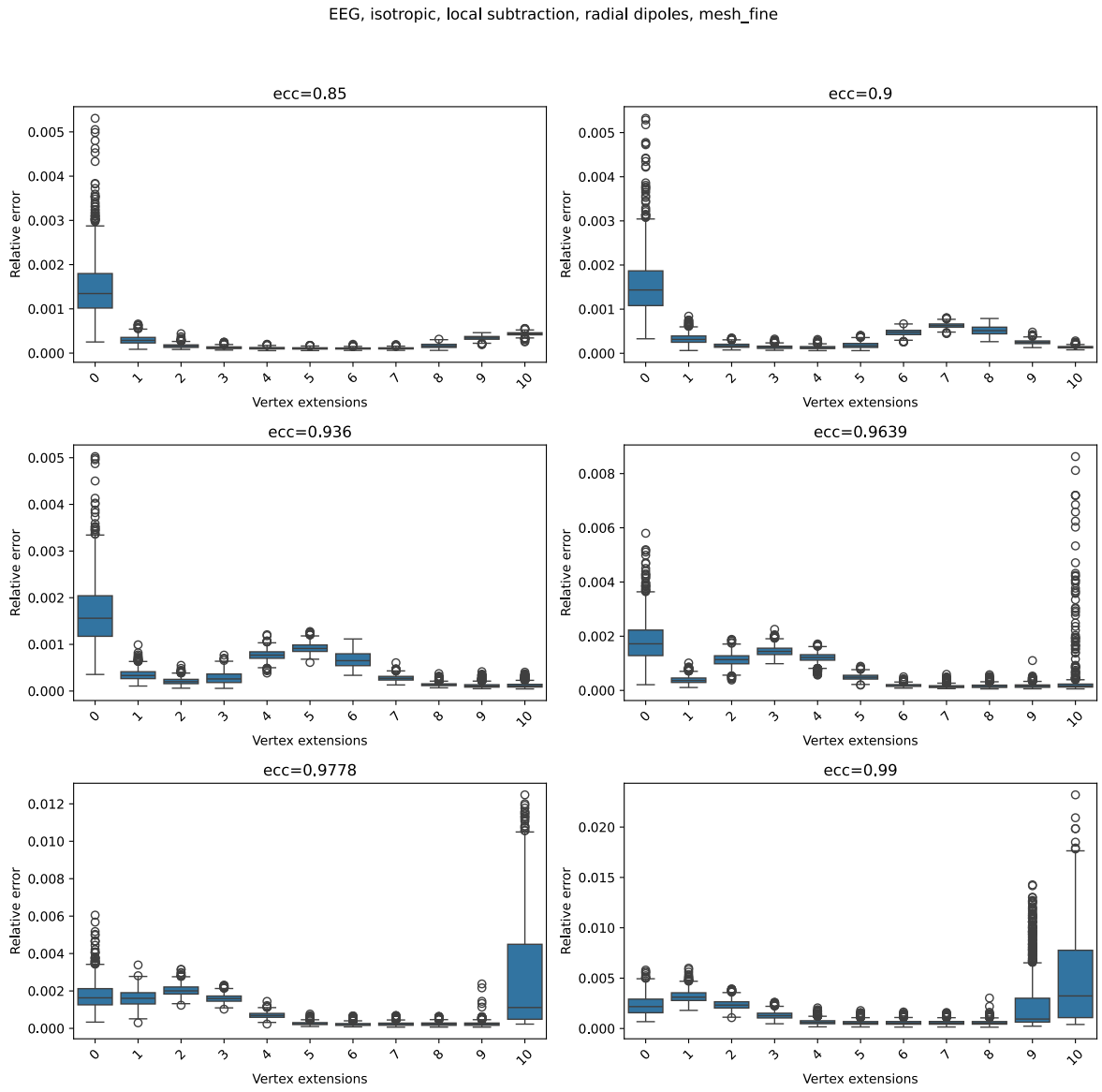

Figure A.5.: Plots showing the relative error of simulating 1000 radial dipoles on `mesh_fine` for different levels of vertex extensions. Thereby ecc is the source depth of the dipoles, given as a fraction of the total brain radius.

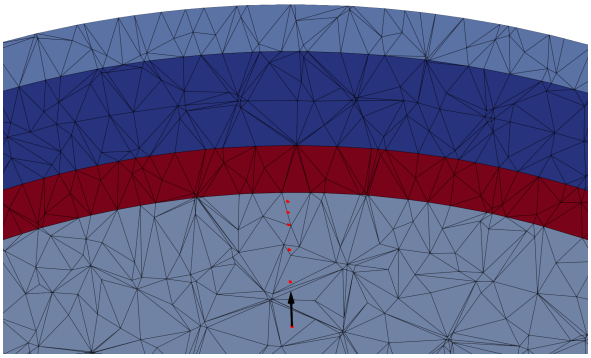

(a)

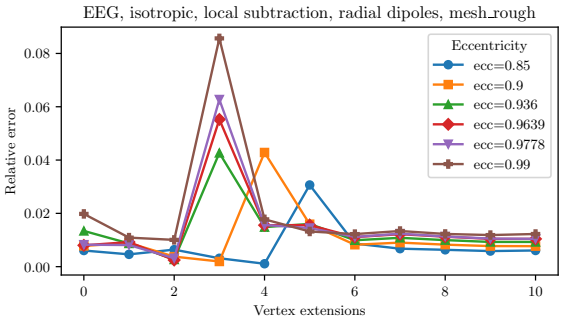

(b)

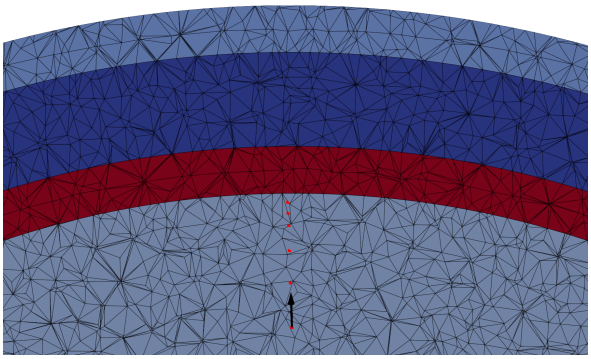

(c)

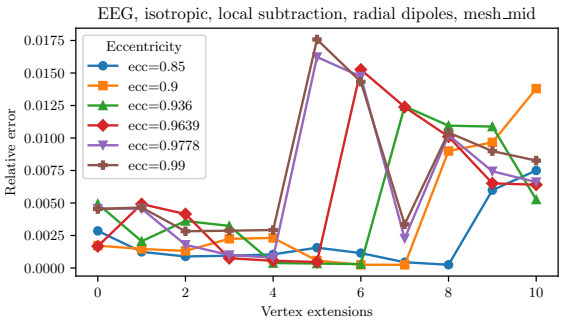

(d)

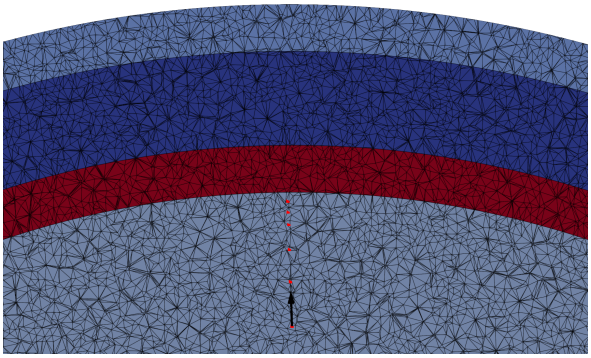

(e)

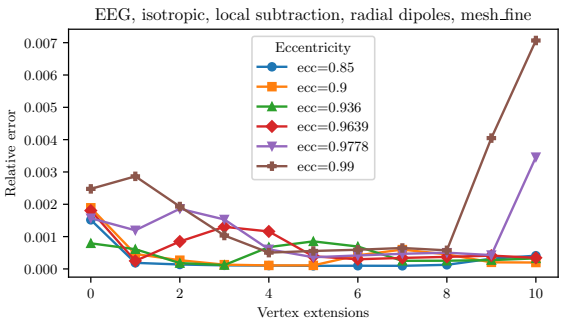

(f)

Figure A.6.: Position ad relative error for dipoles on axis *sphere center* + $c\,(-0.872,\ 0.419,\ -0.25)^T\ \forall c > 0$ on `rough_mesh` (a),(b), on `mid_mesh` (c),(d) and `fine_mesh` (e),(f). Dipole positions are marked by red dots, dipole orientation is represented by black arrow.

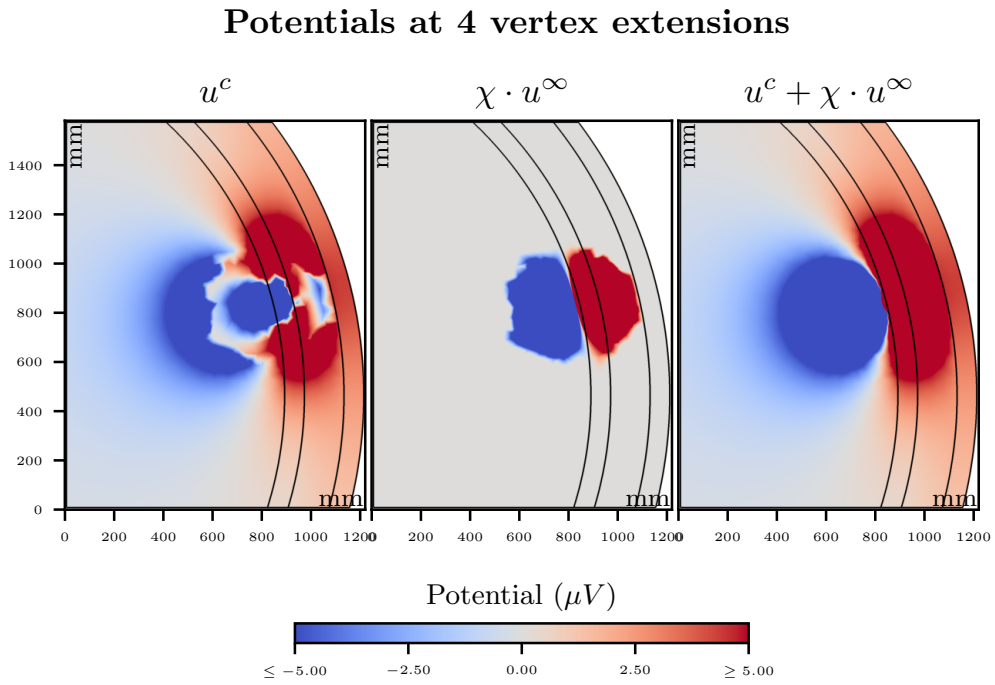

(a)

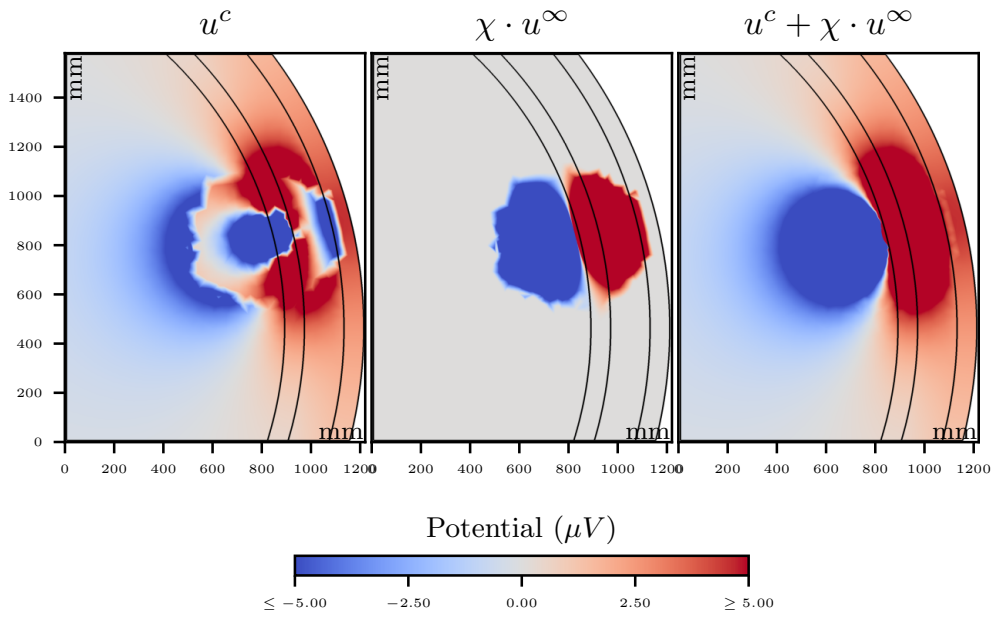

(b)

Figure A.7.: Visualization of the potentials produced by the Local Subtraction approach, simulating a radial dipole at an eccentricity of 0.99 on `mesh_mid`. (a) shows the potentials using 4 vertex extensions and (b) using 5 vertex extensions.

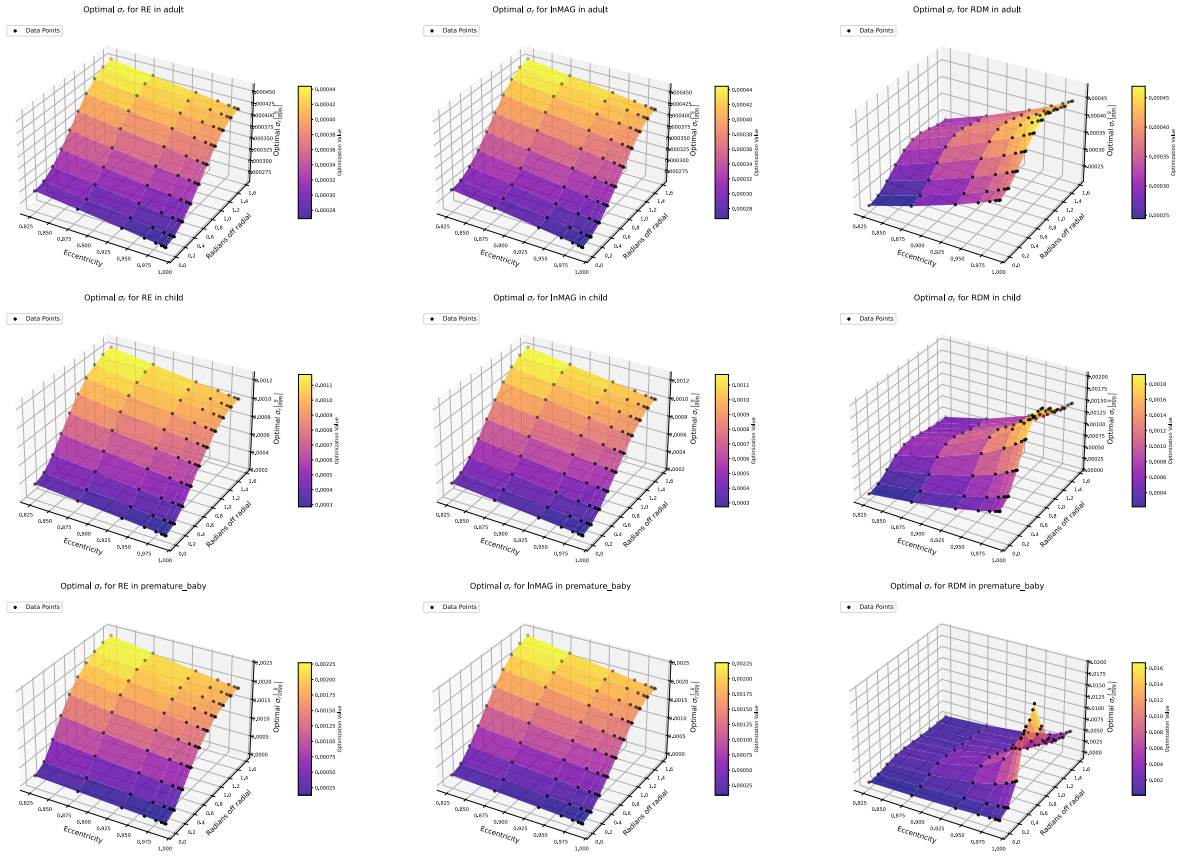

Figure A.8.: Optimal radial conductivities for eccentricity and source orientation. Shown for RE, lnMAG and RDM and adult, child and premature infant conductivity models. 0 radians of radial means a radial source and $\frac{\pi}{2}$ means a tangential source.

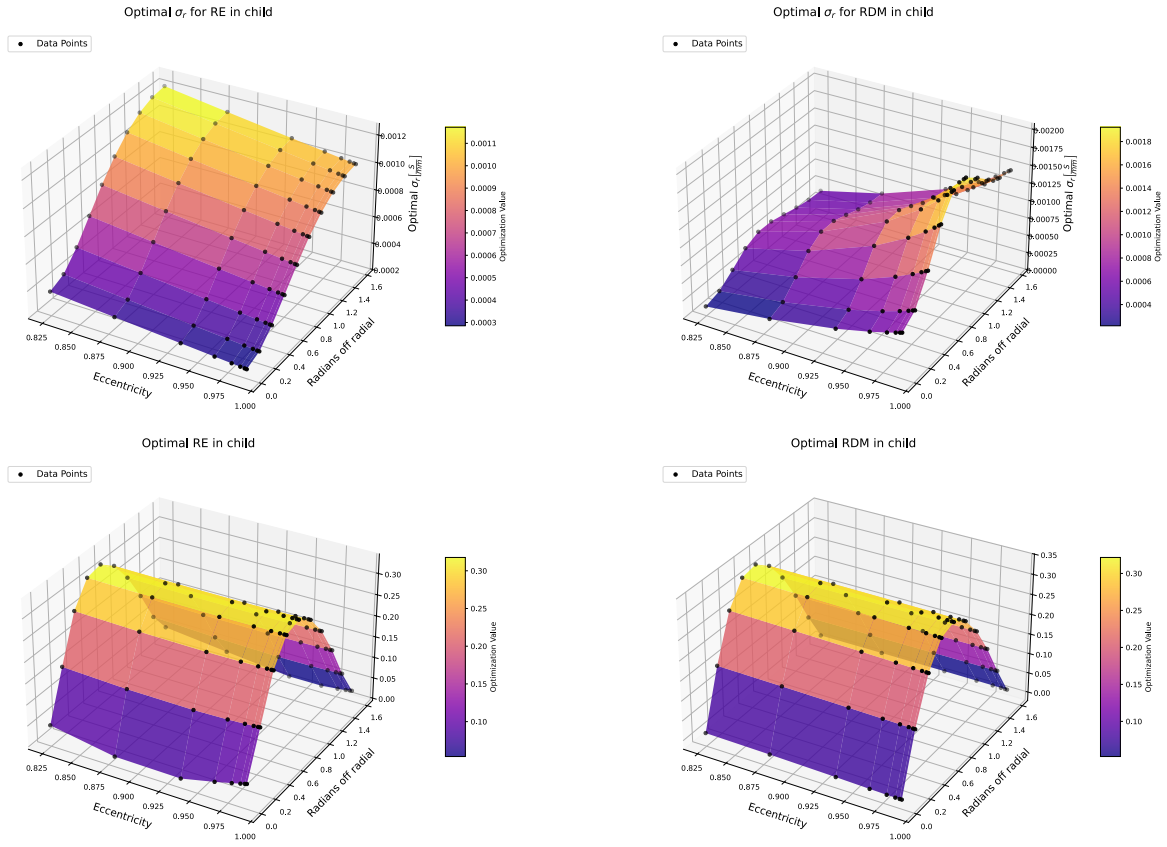

Figure A.9.: Optimal radial conductivities with respect to RE and RDM for child conductivity and anisotropy. Values shown depending on eccentricity as well as orientation, where 0 radians of radial means a radial source and $\frac{\pi}{2}$ means a tangential source. Additionally the difference measure that was achieved between isotropic and anisotropic calculations is shown.

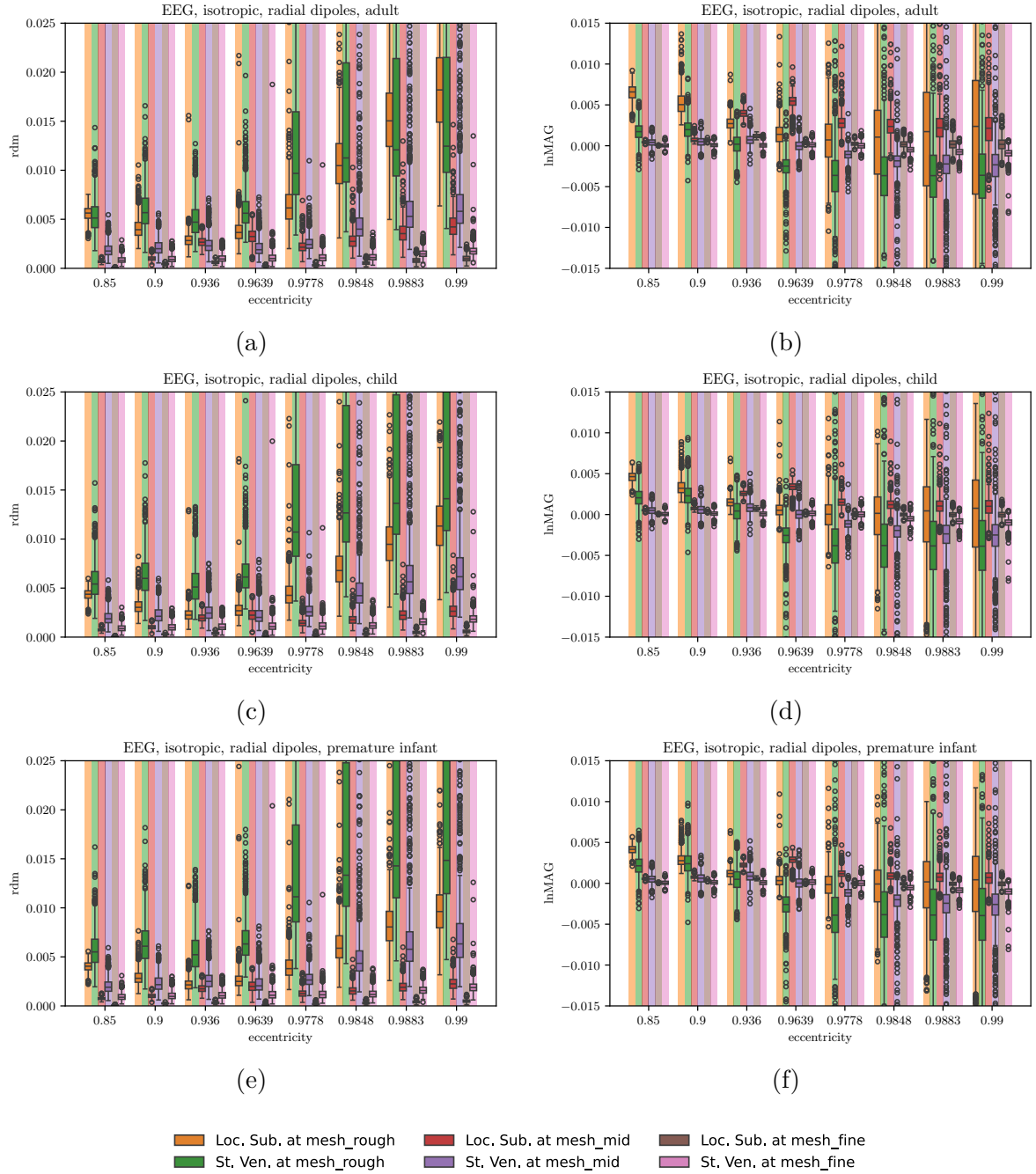

Figure A.10.: RDM and lnMAG comparison of Local Subtraction and Multipolar St. Venant approaches on multiple grids and isotropic conductivities for radial dipoles plotted against eccentricity.

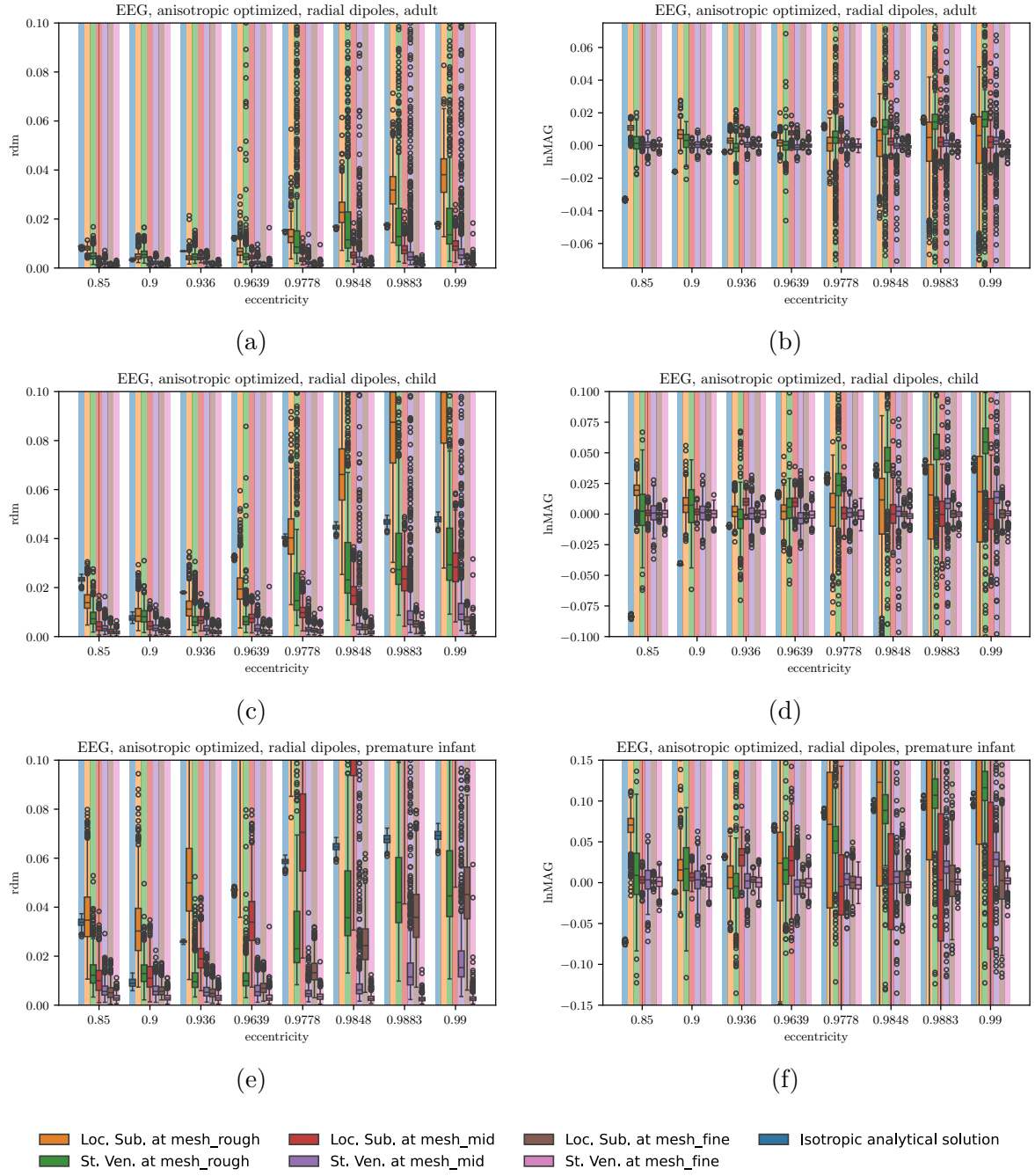

Figure A.11.: RDM and lnMAG comparison of Local Subtraction and Multipolar St. Venant approaches on multiple grids and anisotropic optimized conductivities for radial dipoles plotted against eccentricity. Also included is a comparison against isotropic analytic approximation.

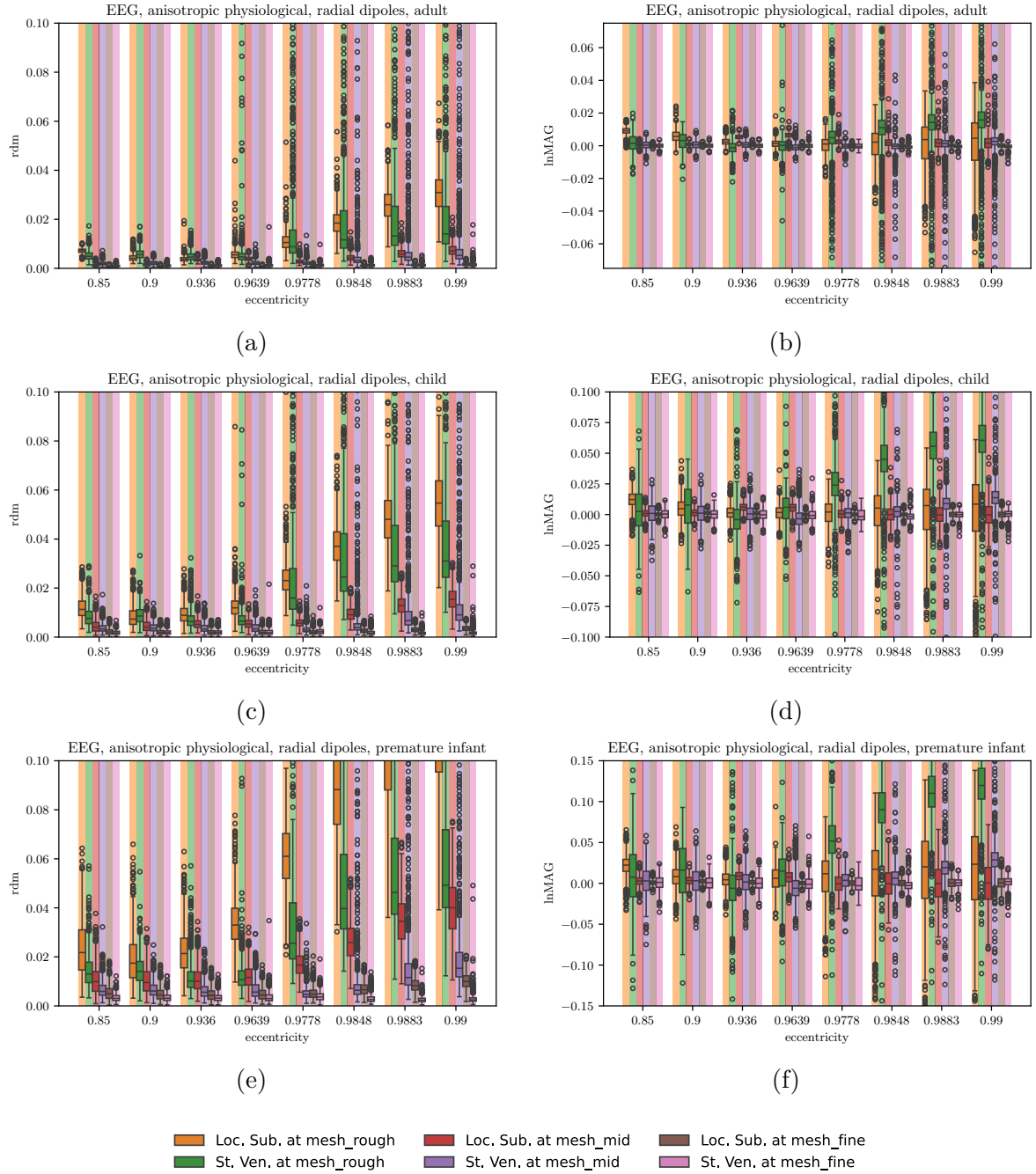

Figure A.12.: RDM and lnMAG comparison of Local Subtraction and Multipolar St. Venant approaches on multiple grids and anisotropic physiological realistic conductivities for radial dipoles plotted against eccentricity.

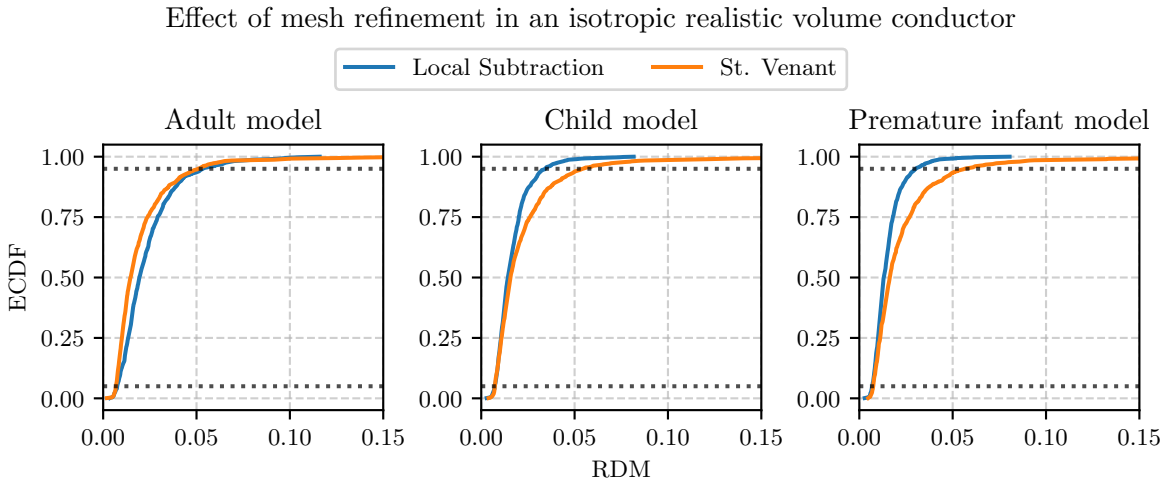

Figure A.13.: ECDFs of RDM for isotropic forward calculations across different mesh resolutions in the realistic head model. Curves compare standard and refined mesh using Local Subtraction and St. Venant approaches for adult, child, and premature infant models.

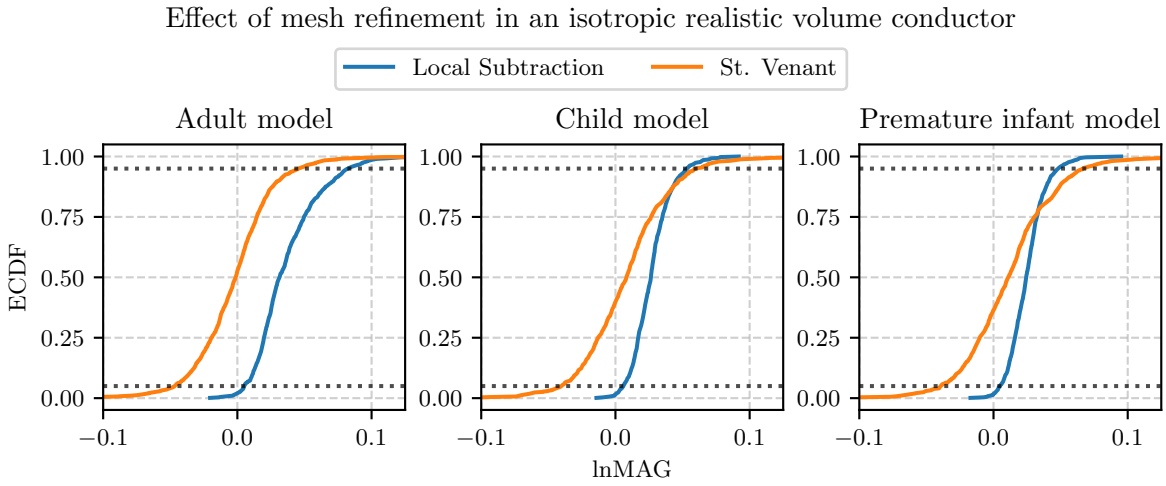

Figure A.14.: ECDFs of lnMAG for isotropic forward calculations across different mesh resolutions in the realistic head model. Curves compare standard and refined mesh using Local Subtraction and St. Venant approaches for adult, child, and premature infant models.

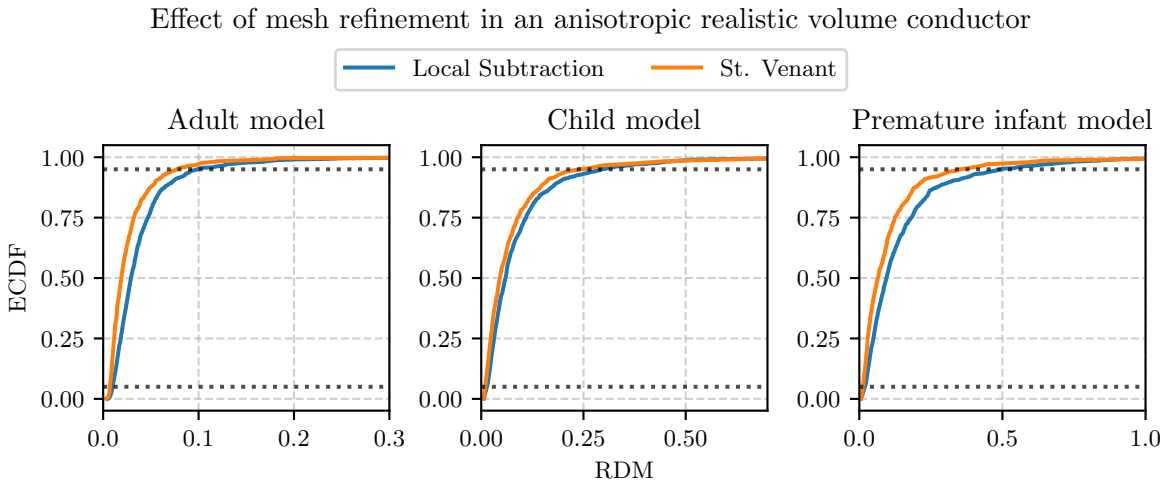

Figure A.15.: ECDFs of RDM for anisotropic forward calculations across different mesh resolutions in the realistic head model. Curves compare standard and refined mesh using Local Subtraction and St. Venant approaches for adult, child, and premature infant models.

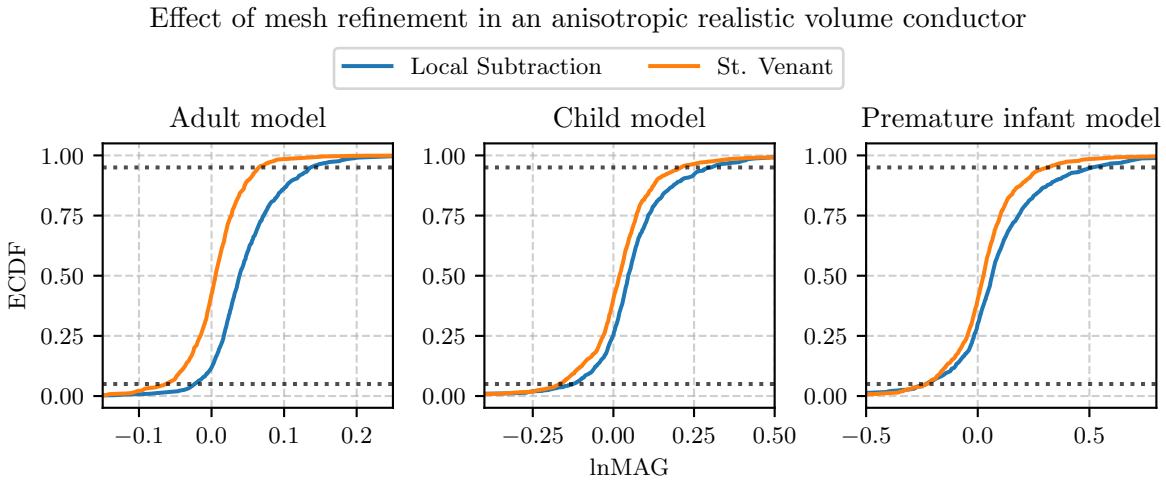

Figure A.16.: ECDFs of lnMAG for anisotropic forward calculations across different mesh resolutions in the realistic head model. Curves compare standard and refined mesh using Local Subtraction and St. Venant approaches for adult, child, and premature infant models.

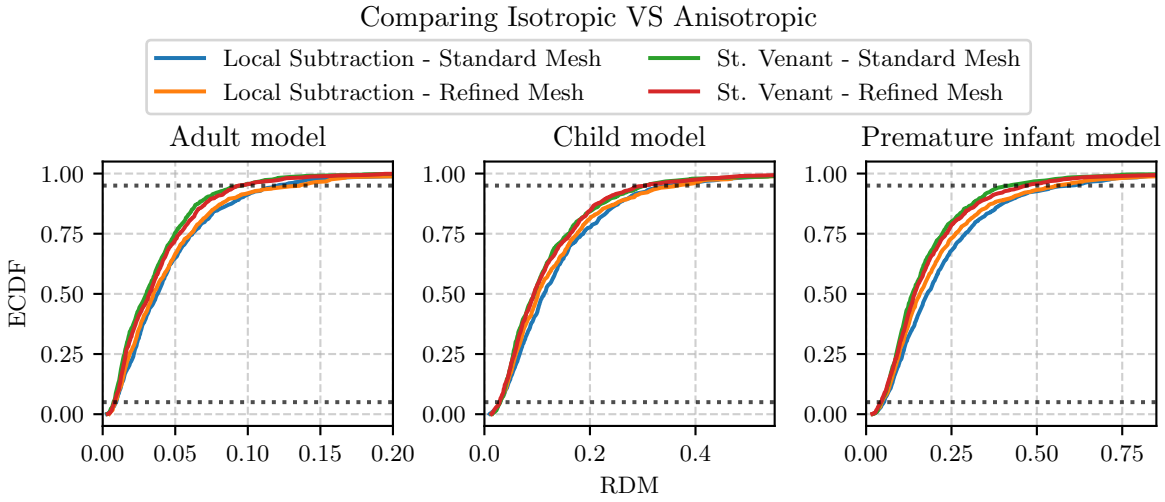

Figure A.17.: ECDFs of relative errors comparing isotropic vs. anisotropic forward calculations in the realistic head model. Results shown for Local Subtraction and St. Venant approaches across standard and refined meshes for adult, child, and premature infant models.

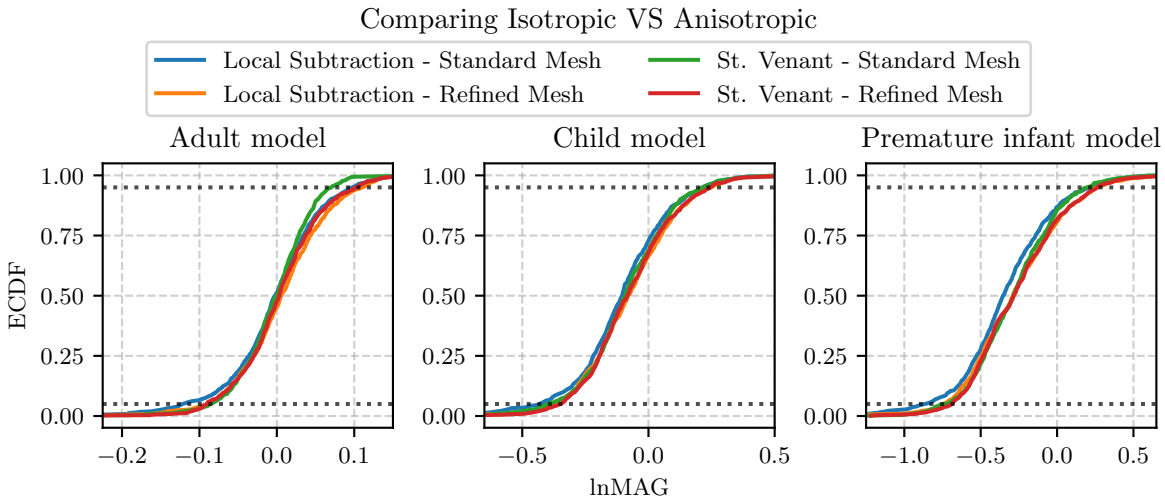

Figure A.18.: ECDFs of relative errors comparing isotropic vs. anisotropic forward calculations in the realistic head model. Results shown for Local Subtraction and St. Venant approaches across standard and refined meshes for adult, child, and premature infant models.